EXPERIMENTAL INVESTIGATION ON THE EFFECTS OF CHEMICAL HEAT RELEASE IN THE REACTING TURBULENT PLANE SHEAR LAYER

Allan Kenneth Wallace, B. Tech., B.E. (Hons)

University of Adelaide

Department of Mechanical Engineering

Thesis Submitted for the Degree of

Doctor of Philosophy

January, 1981

ABSTRACT

A chemically reacting shear layer between various gases was investigated in a new type of blow-down wind tunnel. The gas streams were inert (helium, nitrogen or argon), but carried up to 10% concentration of reactants, one being ozone and the other nitric oxide. The resulting reaction, $O_3 + NO \rightarrow NO_2 + O_2$, was essentially diffusion limited and spontaneous, enabling the temperature rise to be varied at will from zero up to 200°C mean. Flows of Reynolds number up to 5×10^4 were investigated.

Simultaneous shadowgraphs at two different wavelengths (blue and middle ultraviolet) were taken, the blue light showing the product NO_2 and the UV showing the reactant O_3. Mean velocity and temperature profiles of the layer were obtained for various reactant concentration ratios and temperature rises.

The effect of heat release by the chemical reaction was to strongly reduce the entrainment rate of free stream fluid into the shear layer, and to apparently inhibit the smallest, high frequency turbulence scales. The effect of changing the reactant concentration ratio was to skew the mean temperature profile towards the minority reactant side of the layer, but the dependence was not strong.

The measured temperature profiles were also compared with those calculated from probability density functions (PDFs) for the mixture composition at various points across the layer, which were measured in a non-reacting turbulent shear

layer by Konrad (1977). Good agreement was found within the temperature rise range of the experiment, especially for temperature rises less than 100°C. A procedure for inverting the above calculation (i.e., finding the PDFs from measurements of mean temperature rise profiles) was used to produce a set of PDFs comparable to Konrad's which would predict temperature rise more accurately.

The strong effect on the temperature rise of changing the density ratio of the two free streams was demonstrated and shown to be in good agreement with the effect predicted from Konrad's non-reacting PDF measurements. It was also contrasted with the very different result obtained from an eddy diffusivity model of the turbulent shear layer.

Experiments with an argon shear layer which consistently produced unexpectedly low temperature rises are reported.

TABLE OF CONTENTS

Page No.

STATEMENT OF ORIGINALITY

This thesis contains no material which has been accepted for the award of any other degree or diploma in any University. To the best of the author's knowledge and belief, this thesis contains no material previously published or written by another person, except where the reference is made in the text.

A.K. Wallace,
January, 1981

ACKNOWLEDGEMENTS

I am most indebted to Professor Garry Brown as my infinite source of guidance and enthusiasm in every stage of this project. Also I wish to acknowledge the help and advice of various staff at the California Institute of Technology and the University of Adelaide, in particular Professors Hans W. Liepmann, Anatol Roshko and R.E. Luxton. Many people contributed directly to the project by way of discussion or suggestion, including Drs. Chris J. Abell, Andrew S.W. Thomas and Mr. R.J. Kenyon.

The superb craftsmanship of Craig Price, George Osborne and others on the technical staff is gratefully acknowledged for helping construct the rig and instrumentation. It is a pleasure to thank Betty Wood for doing the diagrams and Kathy Franson, Wendy Koch and Helen Koennecke for typing the manuscript.

The work was supported by an Australian Post-graduate Research Award, the Australian Research Grants Commission and the U.S. Air Force Office of Scientific Research Contract F40760-709-C-0152.

Finally I express my gratitude to my parents and friends for their continuing interest, encouragement and support.

LIST OF SYMBOLS

c	mixture fraction (Equation A3)
c_s	stoichiometric mixture fraction (Equation A8)
C_0	molar fraction concentration of subscripted reactant in free stream fluid
C_p	specific heat at constant pressure
d	optical path length (Section 2.5.4)
D	coefficient of mass diffusion (Equation 3.10)
E_a	activation energy (Appendix D)
ΔH_f	change in heat of formation (Appendix D)
I_0	intensity of incident light
I	intensity of transmitted light (Section 2.5.4)
k_f	chemical reaction rate constant (Appendix D)
k	optical absorptivity (Section 2.5.4)
n	number density of subscripted species
n	number of molecules of subscripted species (Section A2)
p	pressure
$p_c(c)$	probability density function of c (Appendix A)
R	gas constant
Re	Reynolds number, usually = $\frac{\delta_\omega \Delta U}{\nu_{N_2}}$
r	free stream velocity ratio, $\frac{U_2}{U_1}$
s	free stream density ratio
t	time
T	temperature
U_1, U_2	free stream velocities $U_1 > U_2$
u,v,w	components of velocity in x, y, z directions

LIST OF SYMBOLS continued

V	voltage (Section 2.5.2)
x	streamwise coordinate. Origin is the end of the splitter plate.
x_0	distance from effective shear layer origin to end of splitter plate
y	orthogonal coordinate (origin is normally y^*)
y^*	position of dividing streamline (Appendix B)
z	spanwise coordinate
α	Damkohler number (Appendix D)
α	temperature coefficient of resistivity (Section 2.5.2)
δ_T	half maximum amplitude thickness of temperature profile
δ_ω	maximum slope (vorticity) thickness of shear layer
ϵ	kinetic energy dissipation per unit volume (Appendix D)
κ	chemical equilibrium constant (Appendix D)
λ	Kolmogorov microscale (Appendix D)
η	$y/(x - x_o)$
ν	kinematic viscosity
ρ	density
θ	boundary layer momentum thickness
θ	temperature rise number $\frac{\Delta T}{T_\infty}$
ω	vorticity
τ	time scale (Appendix D)
ξ	free stream reactant concentration ratio (Equation A4)

LIST OF SYMBOLS continued

Modifiers

$\Delta( )$	difference
$\overline{( )}$	time mean
$( )_\infty$	free stream conditions
$( )_1$	high speed stream
$( )_2$	low speed stream
$( )_T$	within the turbulent zone

LIST OF FIGURES

1. INTRODUCTION

1.1 Background

Modern theory of the fluid mechanics of combustion really began in 1928 with Burke and Schumann. Prior to that time, there appears to be no serious attempt to bridge the gap between the chemists, with their Lagrangian (time based) idealizations of molecular reaction rates, and the kineticists with their practical reacting flow problem, often in the Eulerian (spacial) framework. Working with non-premixed combustion in laminar flow, Burke and Schumann realised that the chemical reaction between two fluids was confined to a zone at the interface which they called a "flame sheet". Reactants were fed to each side of the flame sheet by Fick's Law diffusion. Thus they introduced the idea of a "diffusion - limited" reaction rate. Damkohler (1936) then drew attention to the influence of the ratio α, between a characteristic diffusion time and a characteristic molecular chemical reaction time. Where this is zero, the flow is non-reacting (frozen chemistry) and where it approaches infinity, the reaction zone becomes vanishingly thin as the reactant molecules cannot co-exist in the same region. This second case represented the diffusion limited flame sheet of Burke and Schumann, and has received the greatest attention in the literature ever since because the chemical reaction rate term can be eliminated from the flow equations, which results in a considerable simplification over any intermediate value of α. Friedlander

and Keller (1936) analytically solved the static isothermal plane diffusion layer with a one step second order reaction. The theory of combustion in laminar flows was reviewed by Williams (1971).

Application of laminar flow concepts to turbulent flow increased markedly in the 1940's. Hawthorne, Hottel and Weddel (1949), working in a jet, measured the mixture fraction, c, the molar fraction of fluid originating from the jet in any sample. They showed that the product concentration could not be related to the time average mixture fraction at a point. What was required was a complete probability density function for the mixture fraction at that point. (This idea is analytically described in Appendix A). Their work underlined the importance of the concept of molecular scale mixing and unmixedness in diffusion limited turbulent flows. The time average turbulent system differed from the non-turbulent in the fact that the interface could not be a thin surface, even with infinite reaction speed. The necessity for a detailed knowledge and understanding of the turbulent fluid mechanics was thus confirmed, but much significant work at that time occurred in the field of homogeneous turbulence. Since Kolmogorov (1941), it was well known that the small scales of turbulence were isotropic and independent of the large scales and turbulent energy was cascaded from the large eddies to the small, dissipating eddies. Hence the study of the homogeneous turbulence situation had a role to play in the field of shear flow after breakdown. Some of the

workers in this area were Batchelor (1952) on the stretching of fluid lines and surfaces in isotropic turbulence, O'Brien (1971), and Corrsin (1958) on the statistical behaviour of a reacting mixture under such flow conditions.

Prediction of reaction rates in turbulent flow was approached by Toor (1962), who used an analogy between a scalar species in a non-reacting flow and a reaction invariate species in the reacting flow. With the assumption of dilute reactants, equal diffusivities, and a rapid, irreversible reaction, the time average behaviour of the reacting system could be deduced if the RMS concentration fluctuations and time average behaviour were known in the non-reacting system. Lin and O'Brien (1974) extended Toor's analysis to shear flows, solving for the reacting species concentrations in a jet using data from Tutu and Chevray (1973) of temperature measurements in a heated non-reacting jet.

In the meantime, the behaviour of non-reacting turbulent shear flow structure had received enormous attention. The first detailed study of the shear layer, using hot wire anemometry, is attributed to Liepmann and Laufer (1947). Wygnanski and Fiedler (1970) repeated the study, including higher order velocity fluctuation products and intermittancy. Some pressure data was added by Spencer and Jones (1971) using a special pressure transducer. The recent recognition of large structure in the shear layer (Brown and Roshko, 1974; Winant and Browand, 1974; Dimotakis and Brown, 1976) has led to a much deeper understanding of the entrainment and mixing processes. The important experiments of Konrad (1977) who used an aspirating probe (Brown and Rebollo, 1972) to measure

species and density elucidated the highly non gaussian PDFs of the mixture fraction in the shear layer (in the absence of better information, model builders were, and are, often uneasily forced to assume Gaussian distributions).

At this stage a number of computational models exist and appear to predict mixing and reacting processes in turbulent flows (Spalding, 1974). However, the models badly need quantitative experimental verification, and in particular the greatest unknown is the interaction between turbulence and chemistry. Reacting experiments to date have fallen into two distinct categories.

1. Those where conditions approaching Toor's analogy apply viz. insignificant heat release, usually conducted specifically to isolate the secondary effects of reaction (Batt, 1977; Shea, 1976).
2. Those with high or extreme heat release (causing incandescence) where most of the highly developed and sensitive instrumentation of the isothermal research is unusable (Bilger 1976; Wahl et al 1949 etc.).

The present research is the first experiment to bridge these categories, having infinitely controllable heat release from zero to a maximum of approximately 200^{o}C time averaged.

1.2 Present Research

The requirement in designing this experiment was to abstract a flow which had a wide applicability to real engineering situations (in particular the chemical laser) and at the same time be as simple as possible for experimental and

analytic tractability. There was little difficulty in choosing the plane shear layer (Figure 1.1) for the study. Although it required a dual flow facility, it had the following characteristics.

1. Two dimensionality.
2. Relatively fast achievement of a linear similarity in the x direction.
3. Considerable previous investigation (non-reacting) e.g. Liepmann and Laufer 1947, Wygnanski and Fiedler 1970, Brown and Roshko 1974, Konrad 1976.

A near ideal chemical reaction to use in this study was the nitric oxide - ozone reaction.

$$NO + O_3 \rightarrow O_2 + NO_2$$

which has been well documented (Johnston and Crosby, 1951, 1954; Herron and Hine, 1973), partly from research motivated by atmospheric pollution problems.

It is a simple, second order, bimolecular reaction accomplished in a single collision. Although other reactions can occur in the flow, this reaction dominates within the temperature range of the experiment. (See Appendix D for details of the chemical kinetics). In particular, these other reactions can occur in the rig

1. dissociation of NO_2

$$N_2O_4 \rightleftarrows 2NO_2$$

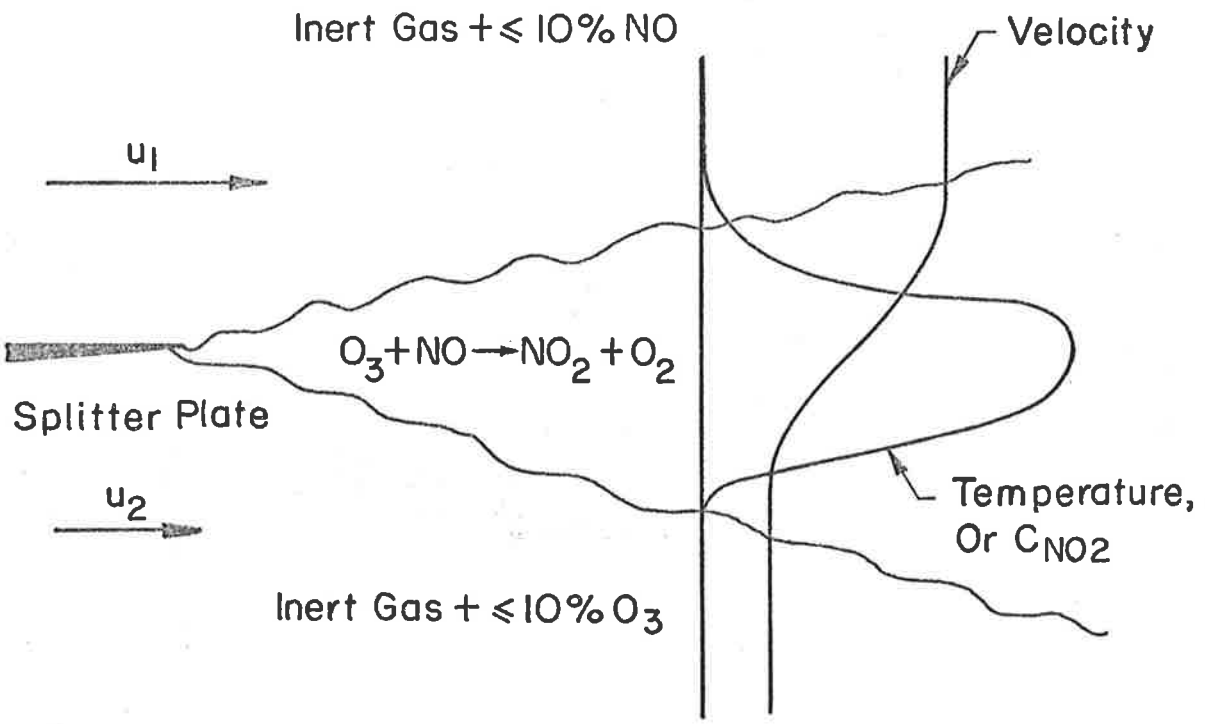

Fig. 1.1 Chemically Reacting Shear Layer Experiment.

2. oxidation of NO

$$NO + \tfrac{1}{2}O_2 \rightarrow NO_2$$

3. dissocation of ozone

$$2/3\ O_3 \rightarrow O_2$$

Data from Verhoek and Daniels (1931) shows that the dissocation of N_2O_4 to NO_2 is highly temperature dependent, and that the reaction product at the temperature occurring in this investigation is substantially NO_2, not N_2O_4. With dilute reactants, when temperature rises are small, the overall effect on the flow due to molecule number change would be insignificant. Comparison of the reaction rate constants for $NO + O_2$ and $NO + O_3$ shows that the first reaction is extemely slow and can be ignored in this flow.† The decomposition of ozone into oxygen was minimized by appropriate design, maintenance and operation of the rig (see 2.4.) and its effect nulled by run time measurement of the ozone concentration (see 2.5.4). Besides simplicity, the ozone,-nitric oxide reaction features unidirectionality, spontaneity, very high speed, high exothermosity and conservation of molecular number. Ignition and extinction problems are thereby avoided, and it is possible to independently vary the heat release in the turbulence from zero to a maximum dictated by experimental or physical constraints.

Calculations in Appendix D show that the chemical reaction time is fast enough for the overall reaction rate in the shear

---

† Some oxygen-nitric oxide runs were made. No reaction was observed in the test section, although some No_2 was present when the gas finally entered the exhaust system.

layer to be considered diffusion limited. A further useful feature is the possibility to independently measure or photograph either NO_2 or O_3 due to their separable and unique absorption spectrums from all other species present (see Figures 2.3).

To achieve a flow with the chemical reaction described here required a new type of test facility. For safety and economy gas quantities should be small, hence an intermittent flow down rig was implicated. Since running times were to be kept small (seconds), fast multichannel data acquisition facilities were also required. The unique system built is described in Section 2. It is highly versatile due to its ability to deliver a constant flow of any reasonably stable gas mixture compatible with Teflon and stainless steel and has been used for studies into non uniform density jets and jet noise besides the shear layers in this investigation. The first results produced by the rig were published by the author in 1977.

1.2.1 Aims of the Research Programme

The discussion in 1.1. indicates that there is a large number of questions to be answered and probably the most pressing of these relates to the effect of the heat released from the chemical reaction on the turbulent flow field. The present facility is ideally suited to incrementally increasing the heat release from zero by simply changing the fuel and oxidiser concentrations, and at the same time effects of changing the fuel-oxidiser ratio can be studied. These two parameters appear later as a temperature rise number, $\theta = \Delta T/T_\infty$, where ΔT

is a temperature rise scale and T_∞ the absolute free stream temperature, and a reactant concentration, $\xi = C_{oO3}/C_{oNO}$. The most important of the effects produced by the chemical reaction to be studied at this stage of understanding of the combustion problem are those relating to the overall flow geometry, the turbulent structure, and the molecular scale mixing rate upon which the reaction depends. Hence the experiment has three main approaches.

1. Effects of θ and ξ on the time average growth rate and entrainment.
2. Effects of θ and ξ on the rate of molecular scale mixing.
3. Effects of θ and the internal flow structure of the turbulent shear layer.

Another important aspect of the work is to partially check the contribution of Konrad (1977) to combustion research. Konrad's measurement of mixture fraction PDFs in the turbulent shear layer can be used, with some assumptions, to estimate temperature rises in that flow. This experiment will provide for the first time a direct check on the PDFs measured in the non-reacting flow, as well as their applicability to the reacting flow.

2. EXPERIMENTAL EQUIPMENT

2.1 Flow Production and Exhaust Treatment

The intermittent blow-down facility used for the present study is shown in Figures 2.1 and 2.2. The gas charge for each side of the mixing layer is mixed and temporarily stored in a gas tight bag made from Fluorinated Ethylene Polythene ("FEP Teflon") 0.125 mm thick and heat sealed at the joints. These bags are contained within two 174 litre steel vessels which are pressurized by a much larger reservoir ($4.65m^3$) of compressed air. Flow is started and stopped by a fast operating (300mS) ball valve before the reinforced PTFE line between the FEP bag and the test section, and is controlled by a finely adjustable multijet low noise metering valve. It consists essentially of a movable piston in a cylinder radially drilled with about 250 small holes equispaced along a helix. Not only does this permit a closely linear variation of area with turns of the hand wheel, but it minimises the noise produced by keeping the frequencies high and having a large number of discrete quadrapole sources. The pressure ratio across this valve is maintained high enough during the run to choke it, and since the system pressure is maintained by the large reservoir to within typically 3% as the bags collapse, the mass flux and flow velocity in the test section are practically constant. After a short time in the settling chamber, the gas passes through the usual flow straightening screens and contractions to the test section.

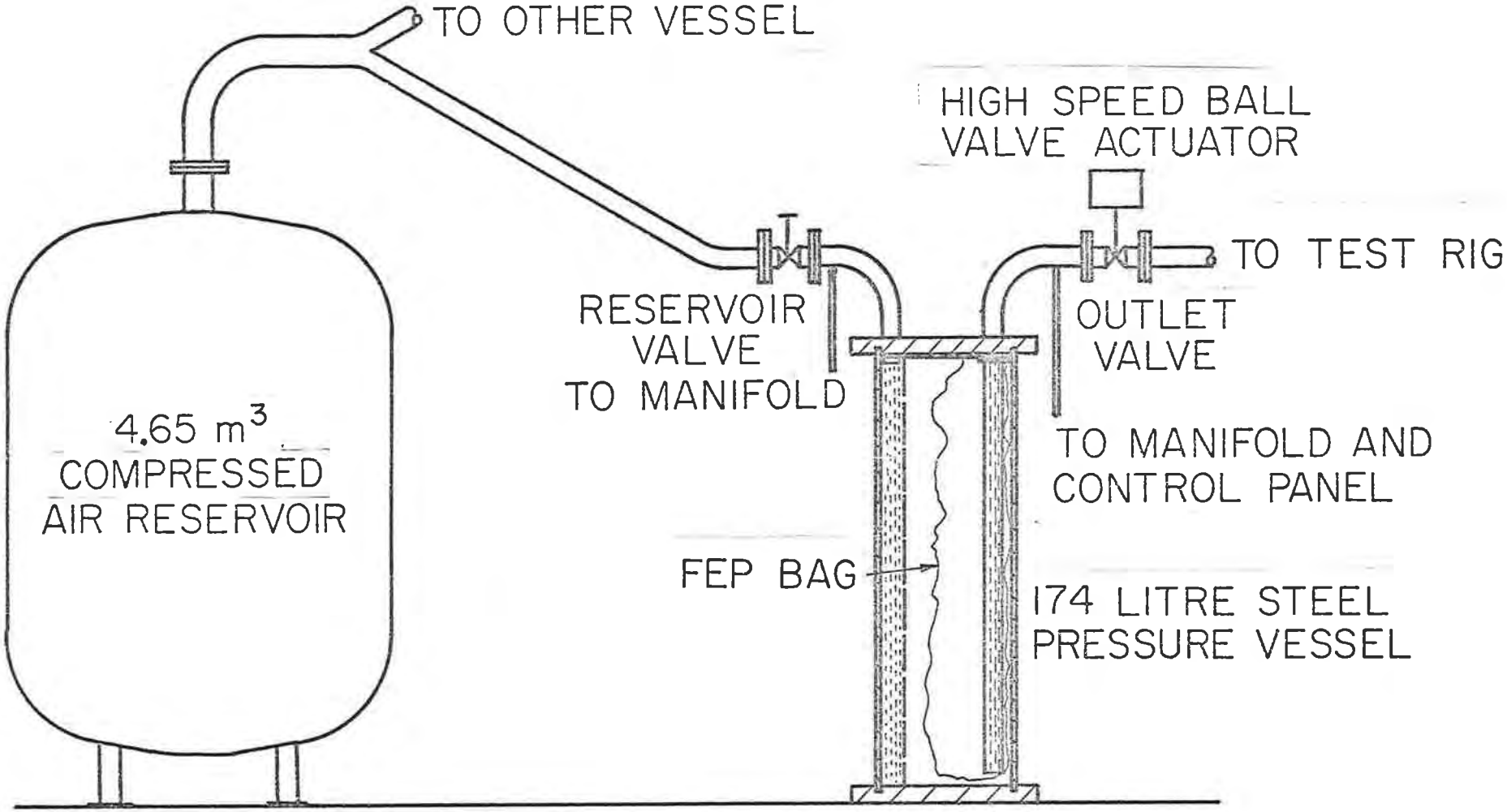

Fig. 2.1 Blowdown Facility (Only One Vessel Shown)

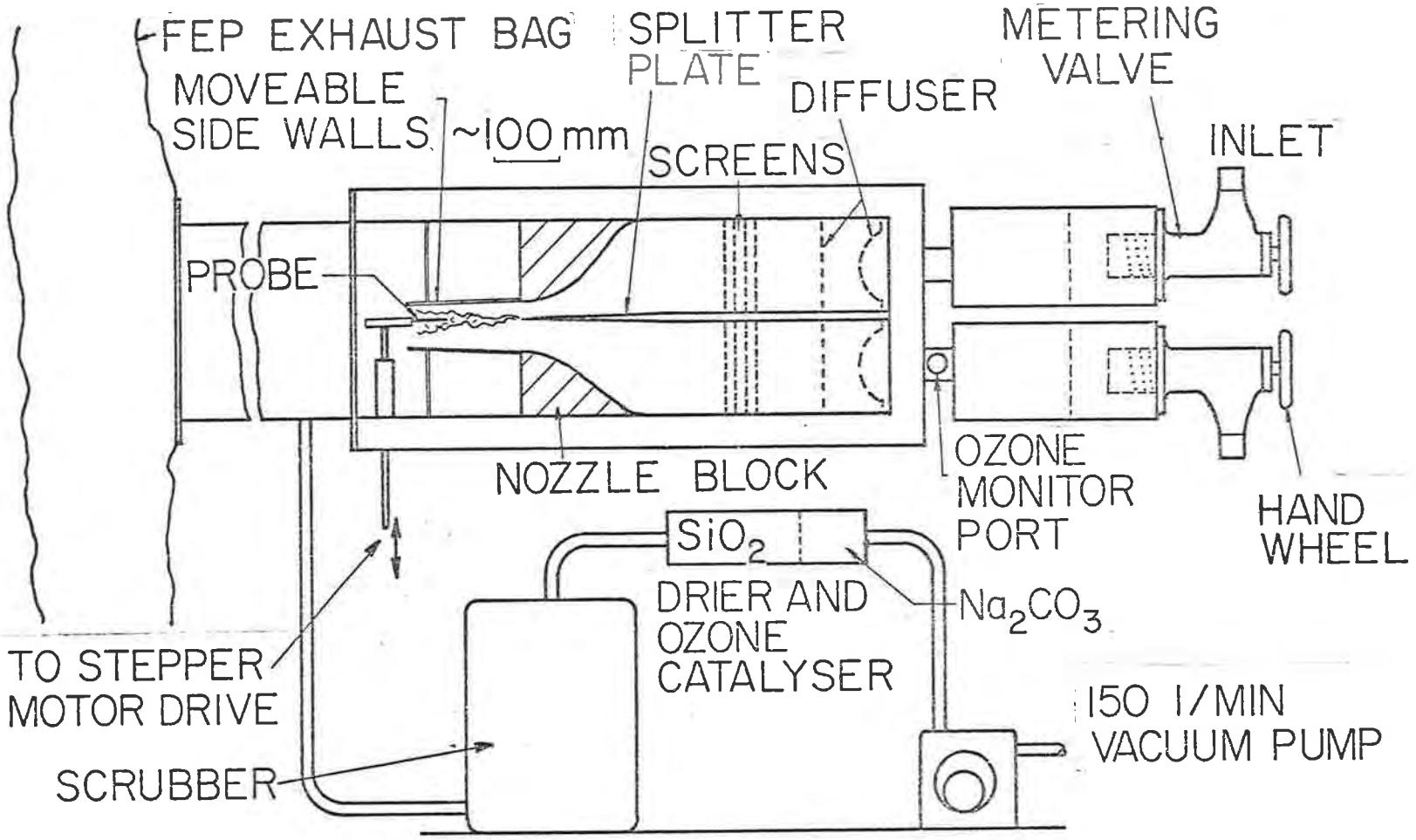

Fig. 2.2 Blowdown Rig- Shear Layer Test Section.

The diffusing section of each duct consisted of two screens of 50% open area perforated sheet, the first bent as shown in Figure 2.2 to approximate an equipotential plane where the streamlines are diverging. Four more screens, two of 30 mesh and two of 100 mesh effectively reduced the turbulence. The entire rig in Figure 2.2. was made of stainless steel except for the contraction blocks (polyester coated wood), the side plates (10 mm perspex) and the moveable side walls (glass). Table 2.1 summarises some specifications of a typical flow.

TABLE 2.1

	High Speed Side	Low Speed Side
Contraction ratio	4:1	2:1
Contraction exit size	100 x 25	100 x 50 mm
Splitter plate included angle	3.6^{o}	
Thickness of end of splitter plate	0.02 mm	
Velocity (nitrogen)	25	5 m/s
Turbulence level	0.25	0.5 %RMS
Boundary layer momentum thickness θ (Thwaite's method) at end of splitter plate	0.06	0.21 mm
B.L. Re $\frac{\theta u_\infty}{\nu}$	100	70
Maximum run time	17 sec	
Typical run time	3 sec	

Included for completeness here also is a plot of the velocity profile very close to the splitter plate. (Figure 2.3). The reason for this is that the initial conditions of the shear layer have been shown to be very significant in determining its subsequent behaviours. The measurements were made by traversing a constant temperature hot wire anemometer. We note that the calculated momentum thickness of the boundary layer on the low speed side is in excellent agreement with the velocity profile measured 1 mm from the end of the splitter plate.

Any mixture of gases compatible with stainless steel and Teflon could be used in the rig and the arrangement supports the safe and convenient use of an unstable gas like ozone (see Section 2.4).

The exhaust gas, usually containing O_2, N_2, NO_2 and O_3 or NO, is collected in a large FEP bag at the atmospheric pressure for temporary storage while a small pump scrubbed it through a solution of sodium hydroxide. This caustic solution catalyses any remaining O_3 to O_2 and absorbs and neutralises most of the nitrous oxides.

The success of the system depends on the FEP bags staying acceptably gas tight and although the bags could withstand repeated complete collapses at full system pressure (700 kPa), care had to be taken not to inflate them beyond their capacity. A special purpose FEP sealing tool was made to manufacture and repair the bags. It consisted of two 100 mm lengths of 12.5 mm diameter thick walled copper tubing heated internally

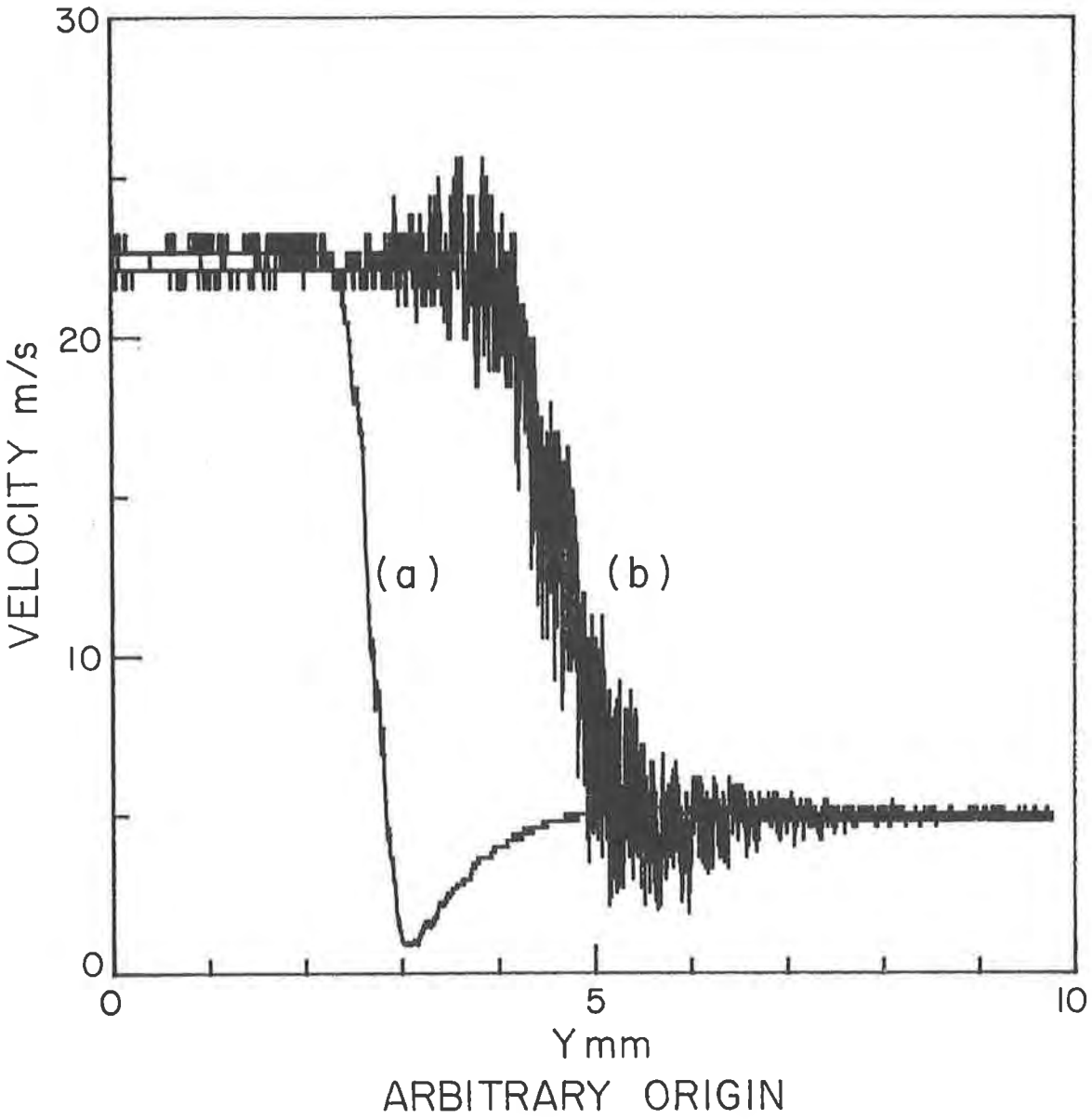

Fig. 2.3 Hot Wire Velocity Traverses Near the Splitter Plate.
(a) x = 1mm
(b) x = 10 mm.

by electric elements and thermostatically maintained at about 260°C. These were brazed to the arms of a spring loaded "scissors" mechanism and handgrip. To make a joint, the two thicknesses of FEP were sandwiched between two thin sheets of PTFE, and then clamped for a fixed time by the sealing device. A little adjustment of time, clamping pressure and temperature soon produced repeatable joints which were as strong in transverse tension as the unjointed FEP sheet.

2.2 Data Acquisition and Traverse Mechanism

Data was acquired on a multichannel high speed analogue to digital conversion system designed and built within the Department of Mechanical Engineering, University of Adelaide. The system accepts data on up to 16 channels simultaneously, 4 digital and 12 analogue. Each input channel can be independently sampled at a pre-programmed rate up to 0.5 MHZ. The analogue inputs are converted to digital values and the numbers stored in a shift register memory of 15k x 8 bit by tes. After an acquire cycle the data is dumped on to a standard 9 track computer tape as a single block headed by 64 bytes of information relating to current channel sample rates, channel memory allocations etc.

The 12 analogue input channels are converted by Analogue Devices Corporation A/D converter types ADC10Z and ADC10QU with 20 and 8 μs conversion time respectively. (These convert to 10 bit accuracy of which the most significant 8 were used). Programming the system to set channel

sample rates and allocate the required memory areas to the channels in use is done via a set of front panel switches. Toward the latter part of the experiment, data not specifically requiring the attributes of the system described above was transferred direct to the computer memory from the experiment.

In this alternative system, based on the Digital Equipment Corporation AR-11 multiplexing A/D converter module with crystal controlled real time clock interfaced with the Unibus on the PDP-11/34 computer (see Section 2.6), the maximum throughput rate was 40kHZ, sufficient for most purposes.

Probe transversing through the flow was accomplished with a stepper motor driven linear ball screw device moving the probe carrier in 0.0005" steps at variable rates up to 5.5kHZ. Clock pulses from the traverse motor control were used to drive the data acquisition system sample commands, ensuring perfect synchronism between the probe position and the sequential location of the measured variable in the output data record.

2.3 Optics and Photography

Part of the motivation for using the ozone-nitric oxide reaction was the separability of the optical absorption spectrums (Figure 2.4). This property enables either ozone or nitrogen dioxide to be detected independently, but it was possible to exploit this even further by taking simultaneous shadowgraph pictures of these components in the flow, separating the two wave-

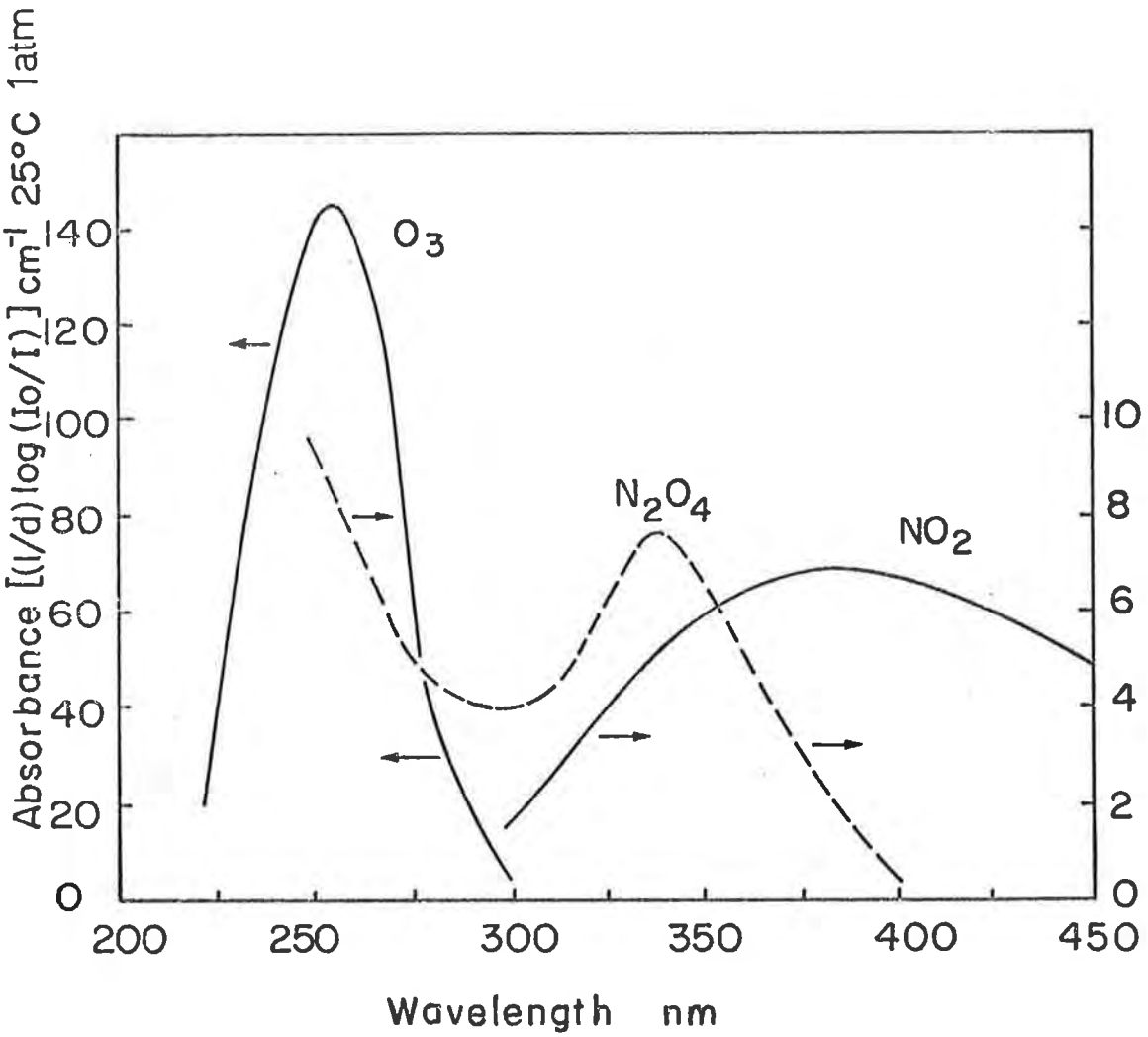

Fig. 2.4 Absorption Spectra of O_3. N_2O_4. and NO_2.

lengths after passing through the test section with a dichroic beam splitting assembly.

The use of a film plate sized interference dichroic beam splitter and interference filters could be avoided by using instead a combination of small narrow band pass filters at the light source, and more economical wide band components at the image end. The narrow band source filters were custom made and had the following characteristics.

	Centre Wavelength	Peak Transmission	50% bandwidth
U.V.	250 nm	30%	± 50 nm
Blue	400 nm	60%	± 50 nm

At the image end, the beam splitter was a piece of 150 mm square x 3 mm thick optical quality glass plate coated with aluminium to 75% reflection at 45^{o} in the visible region. The 3 mm substrate was completely opaque to all UV coming from the light source. Blue light was filtered out from the reflected beam by a 150 x 75 mm optically polished commercial grade "Short Wave Filter" normally used in light sources for activating fluorescent materials. This had a peak transmission wavelength near 250 nm and its band extended to the near ultraviolet allowing some contamination of the UV image by the blue image. However, the plate required over 8 exposures by the blue source to achieve the same exposure as a single exposure from the UV source which is quite acceptable for the current purpose. The layout is shown in 2.5. For a review of ultraviolet technology the reader is referred to Green (1966).

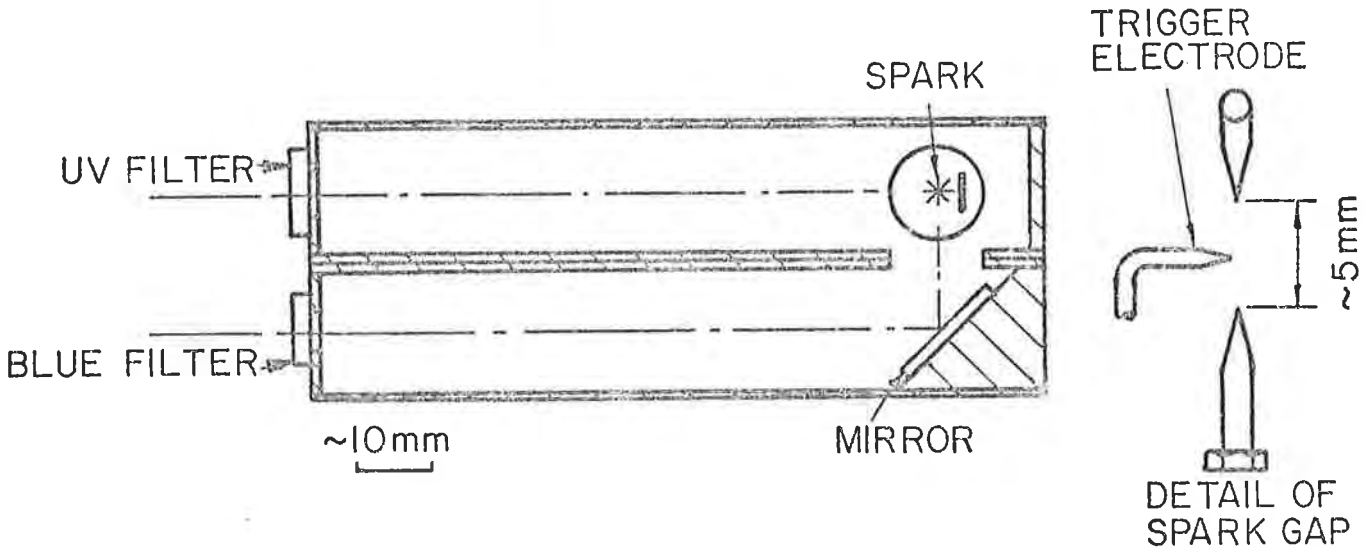

Detail of light source

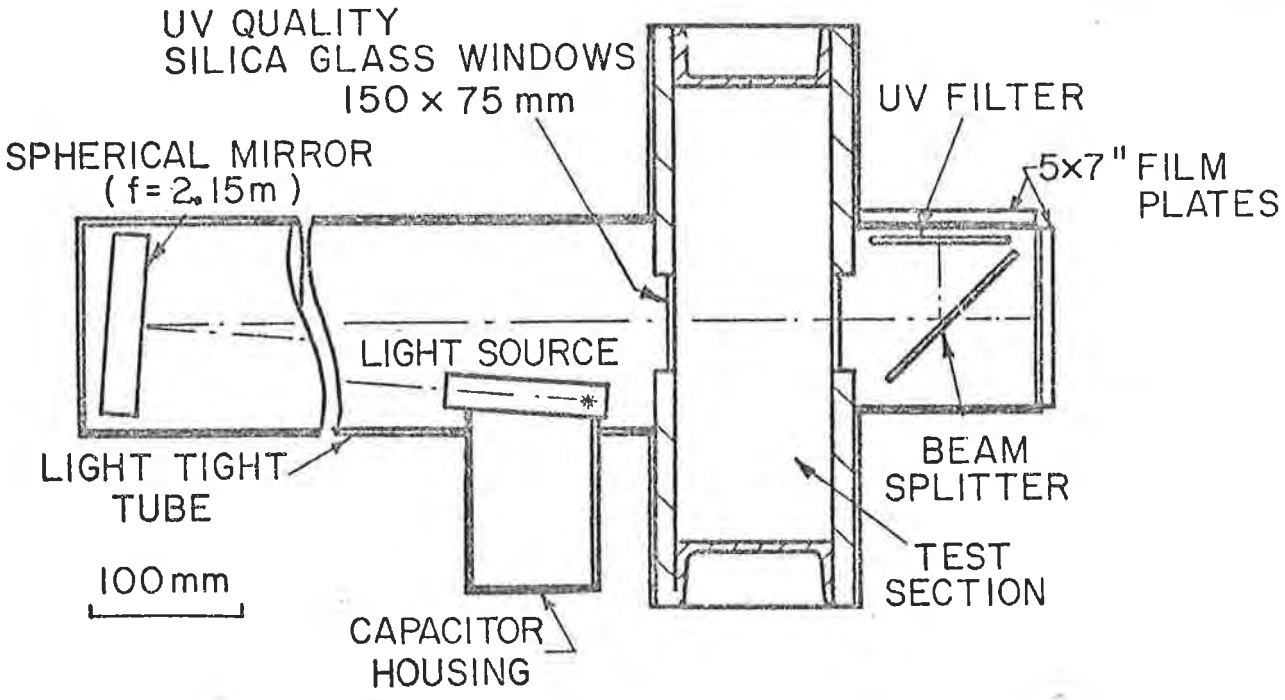

Fig. 2.5 Dichroic Shadowgraph System

An air-arc pulsed light source emitted a wide spectral band extending across the range 250 - 400 nm, being essentially a high temperature black body radiator. A 5.5 μF capacitor provided about 44J of energy to the spark gap giving a pulse with a half power duration of about 1.5 microseconds. Ultraviolet grade silica glass windows enclosed the test section and aluminium coatings gave adequate reflectivities at UV and blue wavelengths. Great care was taken to prevent nitrous oxides contacting the reflective surfaces at any time. A thin coating of magnesium flouride was applied to the beam splitter to protect it from accidental exposure and long term degradation. Standard 5" x 7" flat film negatives (Ilford HP4) were found to have sufficient UV response when developed to about 1000ASA in Ilford Microphen developer.

2.4 Ozone System

The unique properties of ozone demand special care and handling techniques. It is a highly unstable allotrope of oxygen, making it a particularly powerful oxidising agent which easily reverts to diatomic oxygen on contact with material surfaces. Ozone concentration decays with time at a rate proportional to the surface area to volume ratio and the material of its container, with rubber, fabrics and most plastics causing a faster decay than metal or glass† (Sobersky and Simena, 1973).

---

† The only plastics used in the apparatus were polytetra fluorethylene (PTFE), fluorinated ethylene polythene (FEP), Perspex, and polyester resin. None of these exhibited undue deterioration after repeated exposures to high concentration ozone.

Added to its passive decay behaviour is its very real propensity to violent, spontaneous detonation, being "much more sensitive toward detonation than hydrogen-oxygen mixtures" (Harper and Gordon, 1959). Harper and Gordon found that the lower concentration limit for detonation of an oxygen-ozone mixture was only 9%, at which point a shock-wave-with a temperature of 400°C was adequate for ignition. It is also commonly known (and demonstrated within the present rig) that unexpected explosions occur, presumably initiated by the presence of small quantities of organic impurities in the apparatus. The requirements for cleanliness become more stringent as the ozone concentration increases. Naturally the incompatibility of ozone with organic tissues makes it very noxious to the human respiratory system as well: it is well documented as an atmospheric pollutant, interfering with oxygen access in the lungs. All of these factors were considered when designing the ozone system.

The main requirement of the ozone system, Figure 2.6, was to as safely and conveniently as possible provide up to around 10% ozone in a passive carrier gas. Ozone was produced by a conventional electric discharge ozonator (Wallace and Tiernan, Model BA023) at concentrations of 1 to 2% in oxygen. It was then separated from the oxygen by a low temperature sorption process described by Cook et al (1966). Approximately 1 kg of chromatographic grade (28-200 mesh) silica gel was contained in a stainless steel pressure vessel which was placed inside a large dewar flask

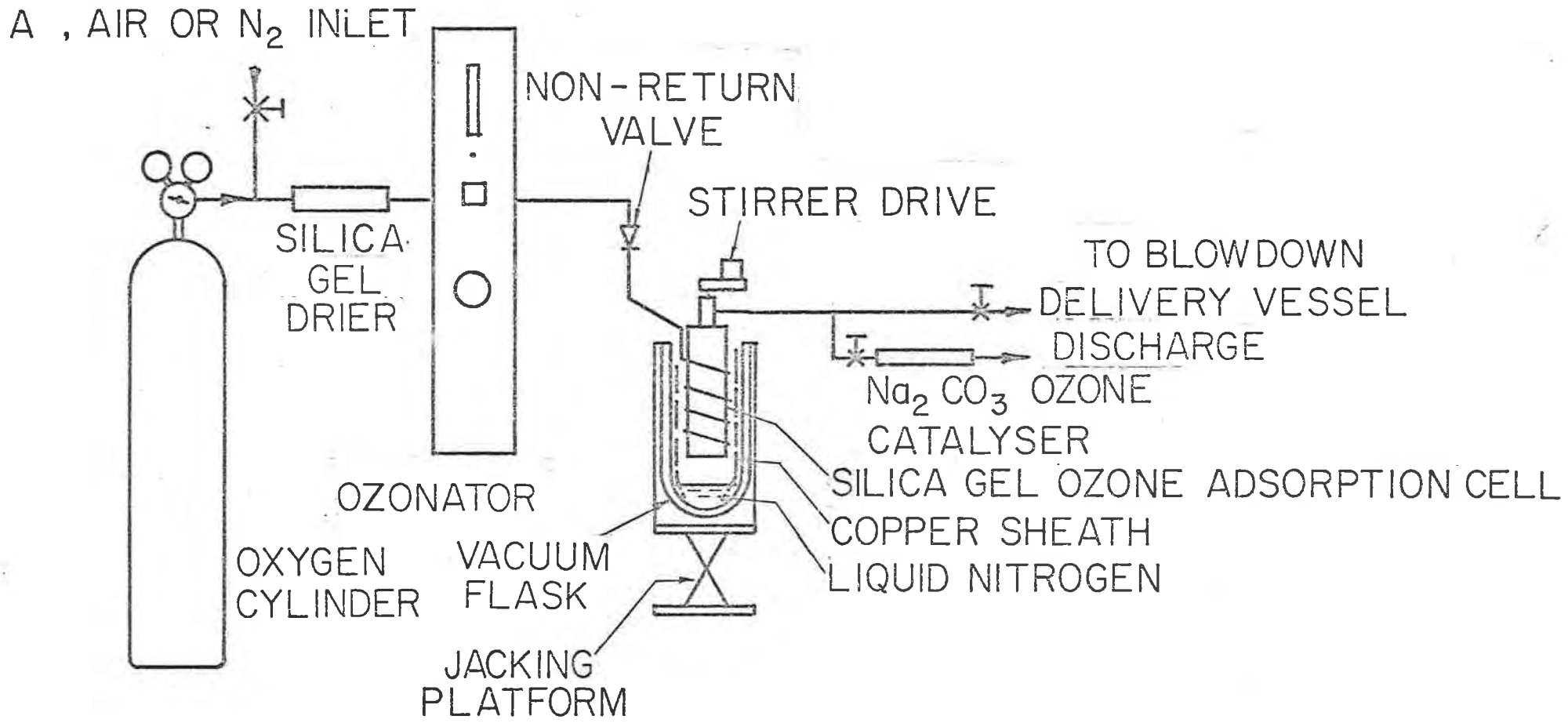

Fig. 2.6 Ozone Generation and Concentration System

above a reserve of liquid nitrogen. A 1.5 mm thick cylindrical copper sheath, laid against the inside of the dewar and dipping into the liquid nitrogen, helped distribute the temperature inside the flask. This sheath was experimentally shaped and fenestrated to maintain a temperature in the silica gel somewhere between - 150°C and - 100°C. Overcooling was found to cause condensation problems in the silica gel, and at above - 80°C the adsorption capacity of the gel was insufficient. The dry ozone-oxygen mixture from the ozonator passed through this cell, which absorbed ozone in preference to oxygen. After the required quantity of ozone had been loaded into the silica gel, the dewar flask was removed and a water jacket placed around the cell as the carrier gas (nitrogen, argon, etc) was drawn through to pick up the liberated ozone and carry it to one of the FEP storage bags in the blow down rig.

The reliability of the process is assured when several experimental maxims are followed. Firstly, only low decay constant materials must contact the ozone, and they must be scrupulously clean. In this rig, the only materials were stainless steel, aluminium and glass as well as the plastics mentioned above, and all surfaces were cleaned with xylene, acetone and methanol (Shea, 1976) before assembly. Secondly, it was beneficial to ensure a good porosity in the silica gel before each adsorption by temporarily fluidising it with a burst of dry oxygen. A mechanical stirrer was particularly useful while desorbing

since it assisted heat transfer and gas flow within the cell. The paddle of the stirrer was helical and rotated in the sense to lift the silica gel. All other forms tried were found to compact the gel and jam, particularly at low temperature. Thirdly, the oxygen supply must be kept as dry as possible to avoid blockage at the cell by ice crystals, and to preserve the adsorbtive capacity of the silica gel. It was necessary to regenerate the silica gel after approximately every twenty cycles by heating in air to 160°C for 2 to 4 hours.

The risk of exposing laboratory personnel to ozone was minimised by forced ventilation in the vicinity of the rig and passing all vents from the apparatus through an ozone catalyst. Both soda lime and activated charcoal were effective for this purpose. The whole system from the check valve after the ozonator to the delivery valve, was designed to withstand at least 14 MPa, a worst case detonation condition.

2.5 Instrumentation

2.5.1 Velocity Measurement

The average velocity in the x direction was obtained from both the pitot static differential and the local average temperature using the relation.

$$\bar{u} = \overline{(2R\bar{T}\ (P_s - P)/P)^{\frac{1}{2}}}$$

where P = static pressure

P_s = stagnation pressure

$\bar{T}$ = local time mean temperature

R = gas constant

For the local temperature measurement technique, see 2.5.2. A Datametrics type 1014A fast response differential electronic manometer was connected to the pitot static tube assembly detailed in Figure 2.7(a). The signal was recorded in digital form and subsequently smoothed with a low pass zero phase shift recursive digital filter described in Appendix C.

2.5.2 Temperature Measurement

In the earlier stages of the project, a tungsten wire operated in the constant current mode (i.e., as a resistance thermometer) was traversed across the shear layer to obtain a mean temperature profile. The probe detailed in Figure 2.7(a), was made from two 0.3 mm diameter steel needles epoxied into a length of 5 micron diameter hollow ceramic rod. A piece of 3 micron tungsten wire, copper plated except for the middle 1 mm, was soft soldered across the prongs. The resulting active portion of the wire therefore had a length-to-diameter ratio of about 200, and a cold resistance of about 7 ohms. (These wires were used by Thomas (1977) as hot wire anemometers).

A simple circuit (Figure 2.7(b)) provided a 1.0 mA constant current to measure the wire resistance. An energy balance on the wire in still air shows that the temperature rise due to electrical heating is less than $0.2^{o}K$, which is negligible compared to the fluid temperature variations and hence the probe calibration is velocity independent. Neglecting the $0.2^{o}K$ overheat, the small higher order non-linearities in the temperature coefficient of resistivity, and assuming a perfectly con-

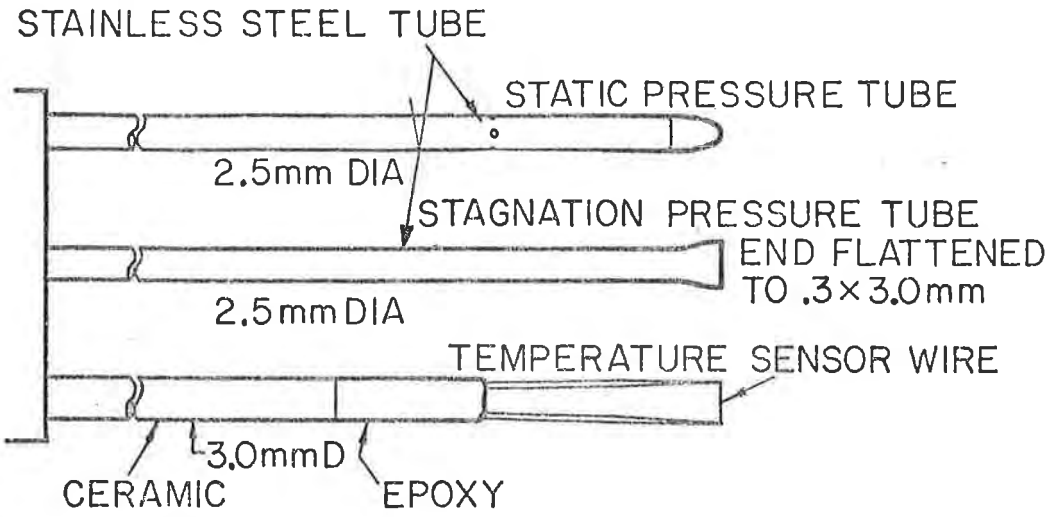

Fig. 2.7(a) Temperature and Velocity Probe

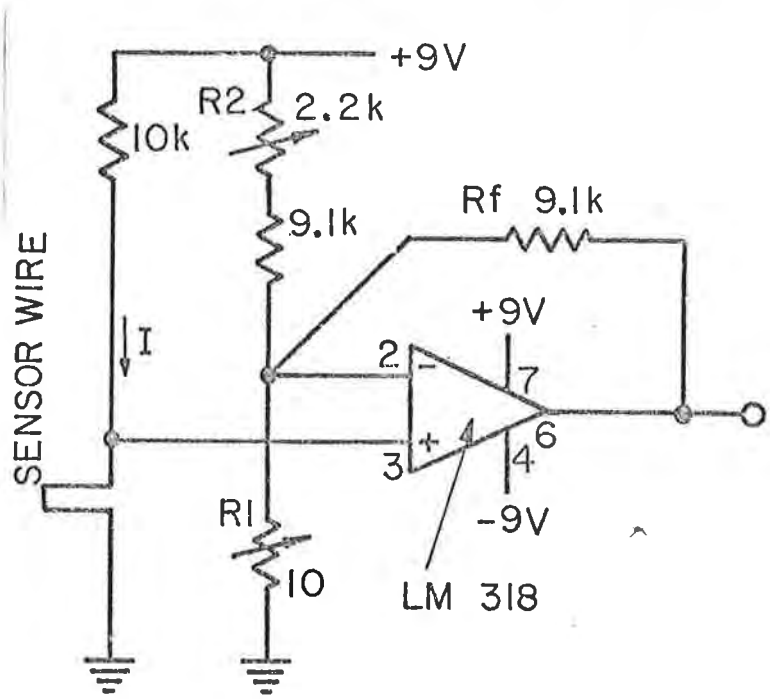

Fig. 2.7(b) Circuit for Temperature Probe.

stant current, I, it is easily shown that

$$\Delta V/\Delta T = I \propto R_f$$

where R_f is the circuit feedback resistance and $\propto$ is the temperature coefficient of resistivity of the wire material. The quantity on the right is easily maintained constant within the range of experimental error, so adequate linearity is assured.

Since the calibration was somewhat subject to drift, (see below), it was necessary to clean and calibrate it prior to each run. Saturated steam was used as a reference temperature.

The frequency response is that of a first order linear system, with a cutoff frequency around 100 Hz in air at 15 m/s.

This type of probe had several drawbacks in use, which became more severe with higher temperature runs. The nitrous chemicals present in the test section were highly hygroscopic, leading to deposition of acidic droplets on the probe, which in turn led to rapid corrosion and unstable resistance. Besides this, the soldered junctions at each end of the wire produced some component of thermovoltaic asymmetry which varied from probe to probe.†

In order to make reliable temperature measurements in runs exceeding about $30^{\circ}K$ rise, it was necessary to develop a fast thermocouple probe (Figure 2.8(a)). A chromel-

---

† The simplest way to check was to move the probe through a jet of hot air and watch the recovery of the amplifier output. The thermovoltaic component has a comparitively long time constant.

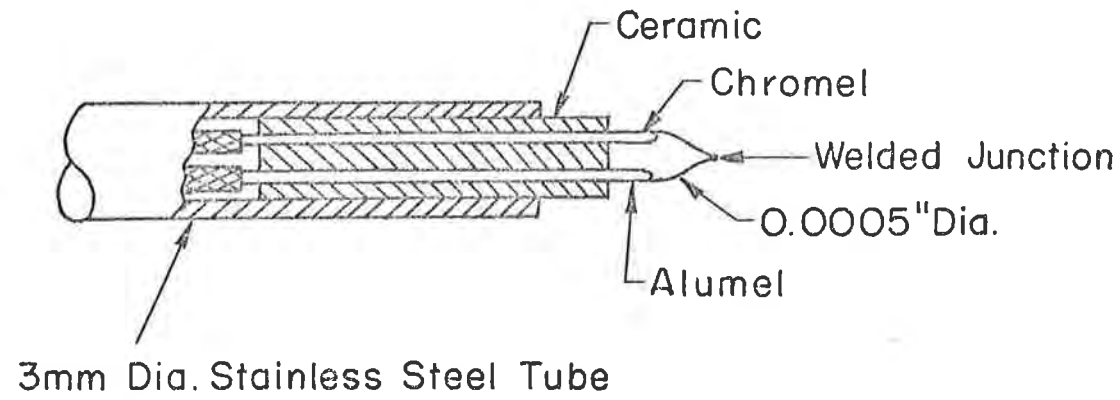

Fig. 2.8(a) Detail of Thermocouple Probe.

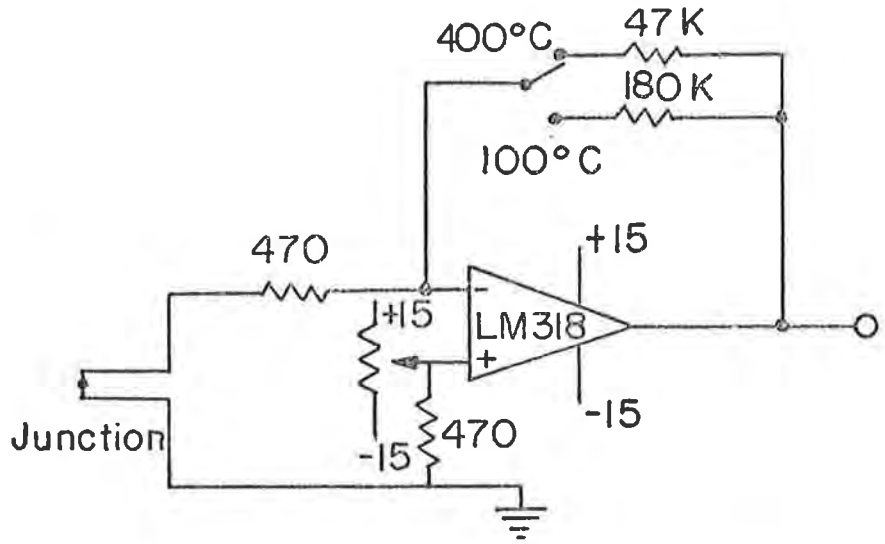

Fig. 2.8(b) Thermocouple Amplifier.

alumel wire pair, 13 micron diameter, was welded together to form the active junction. These were soft soldered to 0.25 mm prongs of the same material anchored in a piece of 3 mm diameter dual bore ceramic insulator. The frequency cutoff for this probe was measured at around 200 Hz in air at 20 m/s which was quite adequate to resolve a mean temperature profile (Figure 2.9). As with the resistance wire, the sensor was prone to hygroscopic formation of droplets, but these would not change the calibration unless they bridged the actual welded junction, which could easily be prevented by washing in distilled water and drying immediately before a run. Corrosion was still a problem, which could be minimized by storing over dry silica gel, but no evidence of significant calibration error could be found to the point where the probe went open circuit. The mean life was 4 or 5 runs. Internal resistance of the thermocouple with leads was typically 45 Ω, and this was taken into account when calculating the voltage gain of the circuit shown. (Figure 2.8(b)). Since a temperature rise was being measured, there was no necessity for a reference junction.

2.5.3 Pressure Gradient

The static pressure gradient was measured in the low speed stream with two static pressure probes (similar to the one in Figure 2.6) placed at X = 0 and 100 mm. The pressure was measured by a Datametric electronic manometer and differential pressure head and the signal filtered with an RC filter with a 50 Hz cutoff frequency. Initial runs proved the pressure gradient to remain constant throughout

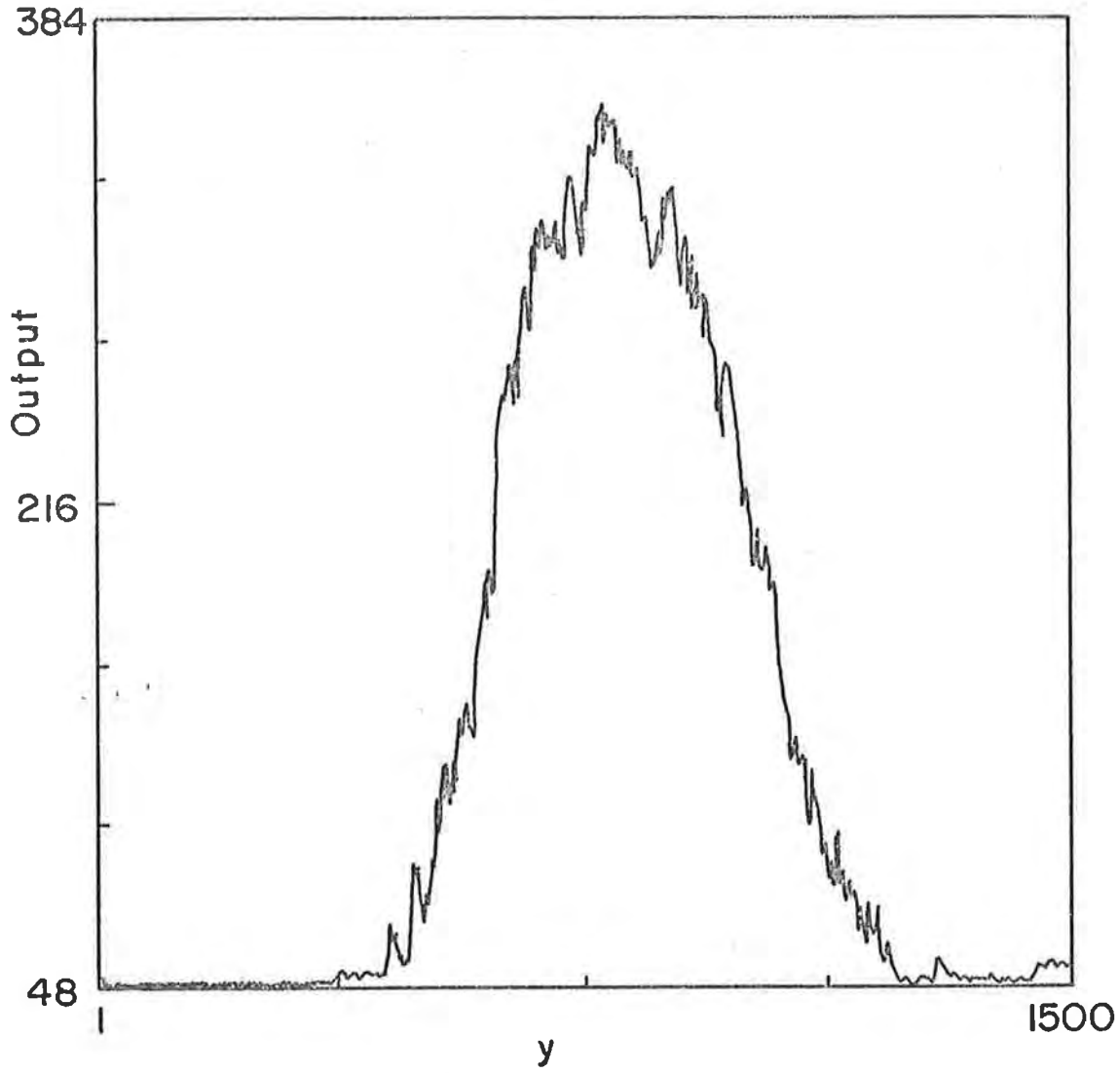

Fig. 2.9 Raw Temperature Probe Data from Traverse of Reacting Shear Layer.

the run, thus requiring only a low sample rate, and this filtering removed the risk of error due to Nyquist folding about the sample frequency.

2.5.4 Ozone Concentration

Due to the unstable nature of ozone and the number of variables in the ozone generating process, it was necessary to measure the ozone concentration immediately upstream of the test section as indicated in Figure 2.2. The ultaviolet absorption meter is detailed in Figure 2.10. It operates on the principle of Beer's Law.

viz $$I/I_o = e^{-kn_{03}d}$$

where I_o = incident light intensity

I = transmitted light intensity

k = absorptivity

n_{03} = ozone number density

d = path length

The construction of the device made it possible to set the gap with micrometer accuracy. The light source was a Penray Model SC-1 low pressure mercury lamp which is very stable and radiates most energy at 253.7 mm. It was driven by a regulated inverter power supply running at 20 kHz (to make it inaudible). Two optical filters were placed in series to isolate the 253.7 mm mercury line. One was an absorption filter supplied by the Penray Company and the second was a bandpass interference filter with a 50% intensity bandpass of 240 - 260 nm.

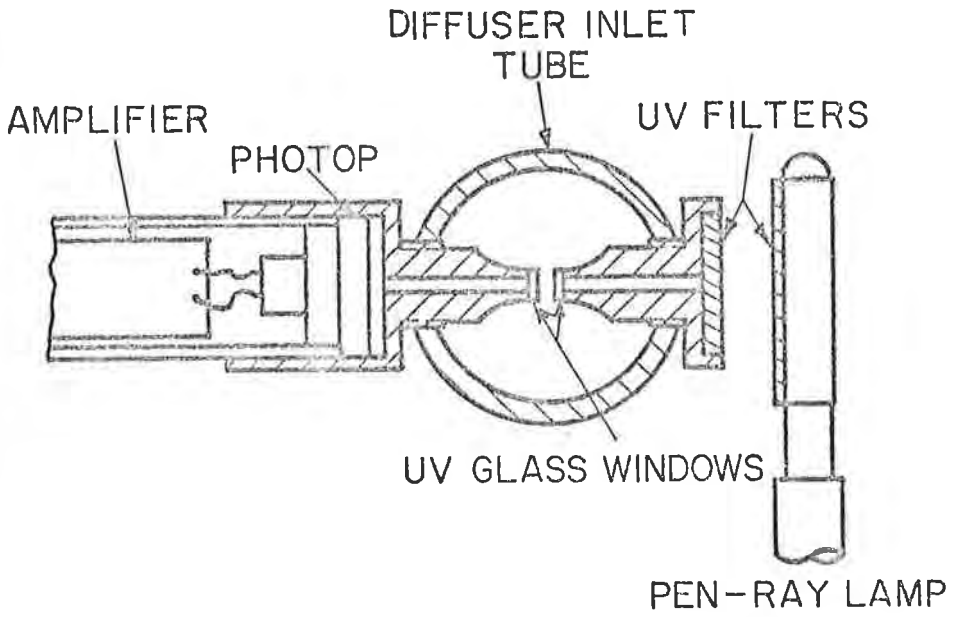

Fig. 2.10(a) Arrangement of Ozone Monitor

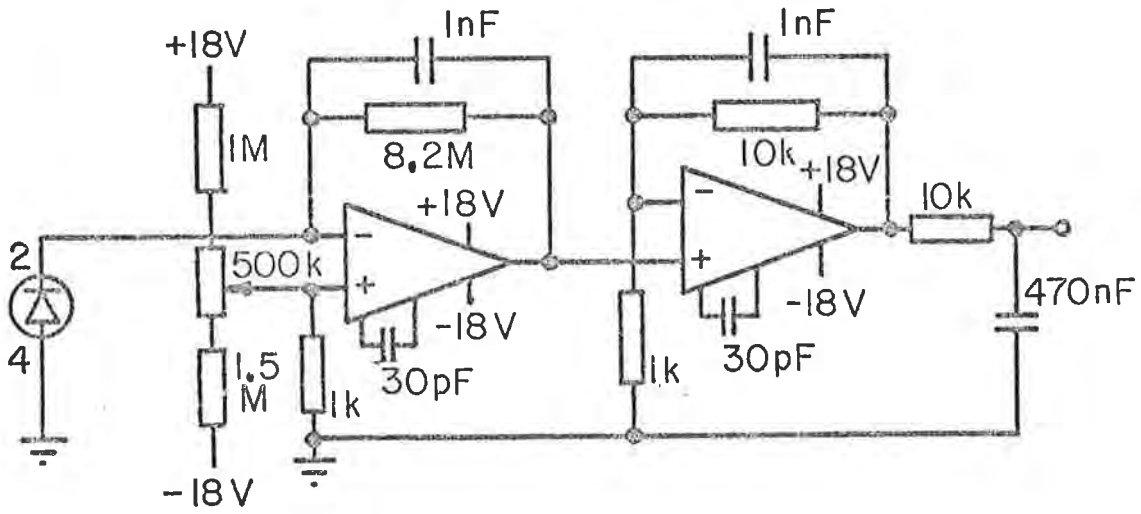

Fig. 2.10(b) Circuit for Ozone Monitor

Having effectively isolated the single wavelength the value of k was known to extremely good accuracy (Griggs, 1968).

A photodetector supplied by United Detector Technology, model Photop 500 with special UV enhancement was used to measure the transmitted light intensity. The circuit detailed is a simple transconductance amplifier with provision for offsetting the output to zero volts under dark conditions, and an RC filter to remove noise and ripple from the 20 kHz lamp supply.

The lamp was turned on at least 30 minutes before a run to give it time to stabilize. Immediately before the run, the lamp was shielded and the output adjusted to zero with the offset control. The output was sampled and digitized immediately before the solenoid operated valves were given the open command in order to establish the value of V_o.

Since the system did not use a reference beam, the drift rate was very carefully checked, and found to be less than 0.7% in V_o and less than 0.1% in V_d over a period of 5 minutes.

2.6 Computing Facilities

Throughout the study a PDP11/34 processor was used, with 28k of volatile memory. Peripheral devices were two RK05 disk drives, an IBM nine track tape drive, a line printer, a teletype terminal and a Hewlett Packard 7221A plotter.

3. RESULTS

3.1 Photographic Investigation

Due to the unusual nature of this flow visualization, this study will be more meaningful if the optical properties of the system are recognized. The information seen on the photographs is in general some combination of refractive index information and species absorption information. The refractive index information is the conventional shadowgraph, where the angular deflection of a ray is a function of the normal refractive index gradient integrated along its path. Refractive index is a function of density, wavelength and species, so both thermal gradients and species gradients (when present) will appear on the plates. The refractive index signature must similarly appear in both UV and blue shadowgraphs, but due to dissimilar light intensity as well as film plate characteristics the contrast is different. Due to the large optical path length between the test section and film plate (Figure 2.5) the bent ray becomes considerably displaced by the time it reaches the film, which accounts for some loss in resolution. The light absorption by a gaseous species is an exponential function of density, path length and absorptivity. The optical density-exposure characteristic of the film is logarithmic so that the optical density at a point, within a certain range, is a linear function of the total absorbing species within the ray. At the wavelengths used, however there is a factor of 20 difference between the absorp-

tion coefficients of nitrogen dioxide and ozone. The mean concentration required to register a difference of one stop on the plate is 0.5% and 0.02% respectively, so the sensitivity of the UV plate to ozone is far greater than the blue plate to nitrogen dioxide. Effects from the boundary layer on the viewing windows are generally negligible except for the ozone pictures. No significant refractive bending would occur because the boundary layers are thin (~ 0.5 mm) and the gradients tend to be aligned with the light beam. However in the case where the boundary layers are locally contaminated with a typical maximum possible concentration of nitrogen dioxide or ozone, the appropriate light beam would be attenuated to the extent of 0.1 and 2 stops respectively. Some tests were done to determine how good the dichroic optics were in separating the frequencies. Contamination of the UV plate by blue light was found to be 3 stops down, while UV contamination of the blue plate was immeasurable. Smear due to finite exposure time is insignificant, amounting to about 50 μm (.002") on the full size plate. Finally, all pictures were taken through a 100 mm width of flow, about 4 of the maximum visual shear layer thicknesses seen in the photographs. In discuss ing the photographs, for brevity the location along the layer will be stated simply as the proportion of the total length from the left hand edge, e.g., x = 1 refers to the extreme right hand edge.

The first set of pictures is from a series of runs

in the He/N_2 shear layer, in which the heat release was progressively increased while keeping all other variables constant (Figures 3.1 - 3.4). Figure 3.2 is from an identical flow as 3.1. It is included to demonstrate the variability between different realisations. The Reynolds number at x = 1 in the non-reacting pictures (3.1, 3.2) is $\frac{\Delta u \delta_\omega}{\nu_{N_2}} \sim 4 \times 10^4$ and since the maximum temperature that can exist at the flame sheet is 300 and 420°C in Figures 3.3 and 3.4 respectively, the corresponding local Reynolds numbers in these regions of maximum temperature are decreased to 35% and 27% of the cold value. A detailed examination of these three pictures reveals several effects as a result of heat release. Firstly, the initial roll-up of the Kelvin-Helmholtz instability in the laminar layer appears to be delayed. Secondly, there is a dramatic change in the appearance of the small scales. Heat release apparently has the effect of delaying transition and inhibiting the energy cascade to higher frequencies. It is worth noting here that the Kolmogorov microscale varies as $T^{1.3}$ but is well below the resolution of the photographs. The behaviour of the small scales would appear to be some function of the local Reynolds number (based on the temperature in the local flame sheet). Clearly the dynamics of these small scales must be directly effected by volume expansion as well as simple viscosity increases, and this may be the dominant factor in the suppression of the highest frequencies. Hence, the effect of heat release in the shear layer is a stabilizing one, since the molecular scale mixing processes upon which the reaction itself ultimately

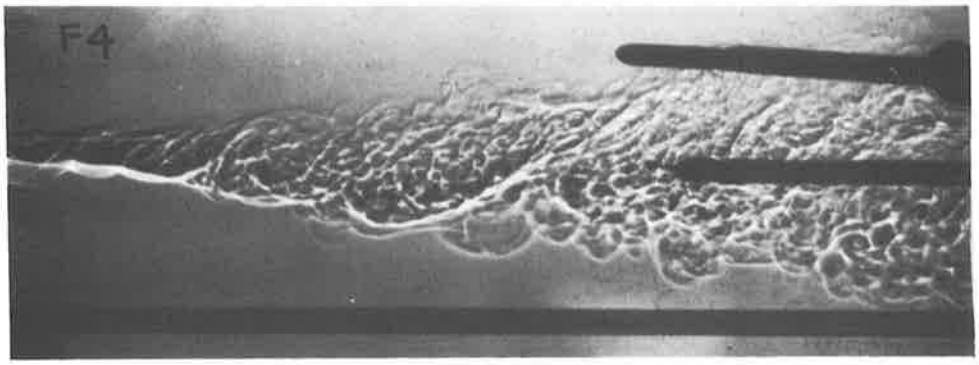

(a)

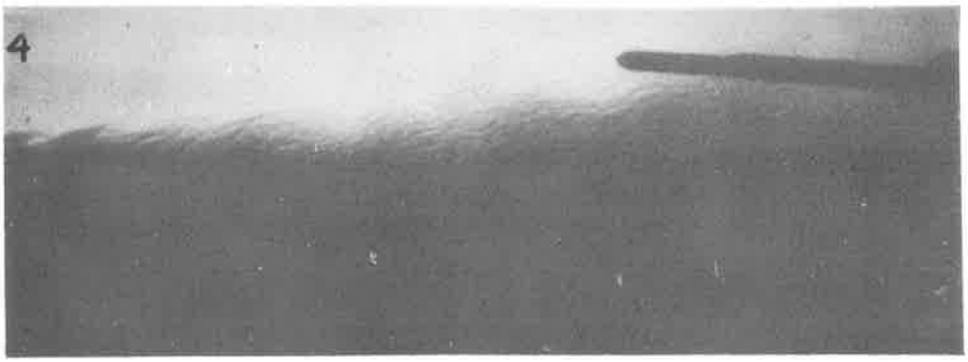

(b)

FIGURE 3.1 Simultaneous Blue, (a) and UV, (b) Shadowgraphs of Non-Reacting He/N_2 Shear Layer

Upper Stream He 25 ms^{-1}

Lower Stream N_2 5 ms^{-1} $C_{0\ 03}$ =.75%

FIGURE 3.2 Shadowgraph of Non-Reacting He/N_2 Shear Layer

Upper Stream He 25 ms^{-1}
Lower Stream N_2 5 ms^{-1}

(a)

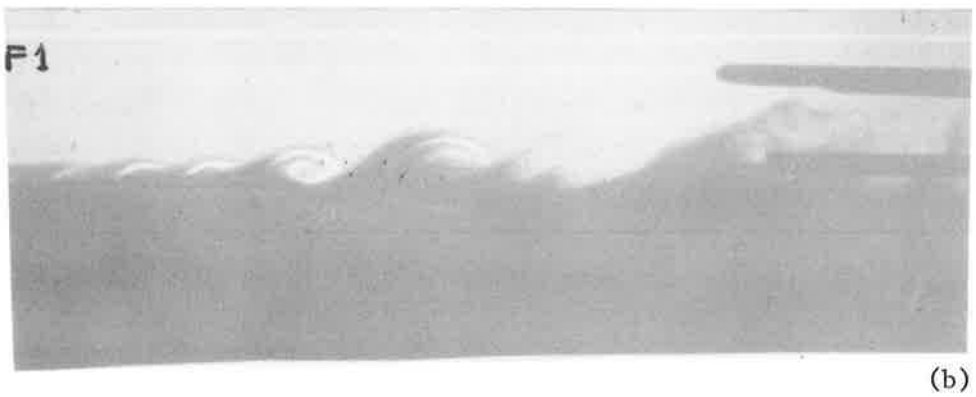

(b)

FIGURE 3.3 Simultaneous Blue, (a) and UV, (b) Shadowgraphs of Reacting He/N_2 Shear Layer

Upper Stream He 25 ms^{-1} $C_{0\ NO}$ = 7.0%

Lower Stream N_2 5 ms^{-1} $C_{0\ 03}$ = 7.7%

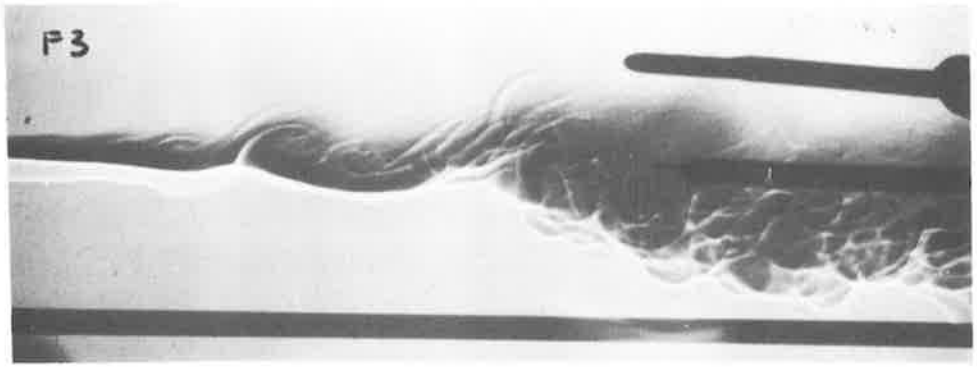

(a)

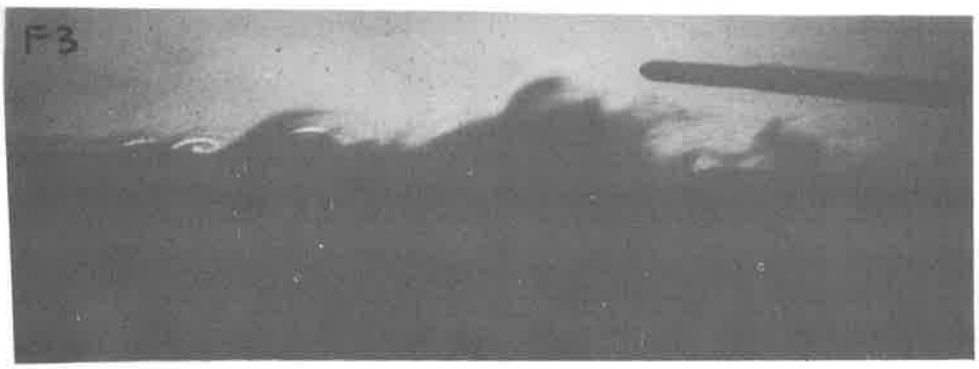

(b)

FIGURE 3.4 Simultaneous Blue, (a) and UV, (b) Shadowgraphs of Reacting He/N_2 Shear Layer

Upper Stream He 25 ms^{-1} $C_{0\ NO}$ = 10.0%

Lower Stream N_2 5 ms^{-1} $C_{0\ 03}$ = 10.0%

depends appear to become less efficient. (Obviously it would be questionable to draw such conclusions merely from the three realizations shown; however, this observation is generally consistent with a number of other realizations, including those made in other gases. The main reason for exhibiting the helium-nitrogen layer here is that much more information is present due to the refractive index difference).

A priori it is not clear whether heat release increases or decreases the width of the layer. Certainly the volume expansion due to heat release causes a v component of velocity at infinity. However there is no significant width increase indicated on the pictures. Measurements presented below will confirm this. Since the density is lower, the amount of mass within the layer is therefore decreased, implying a reduced overall entrainment of free stream fluid. The extent of entrainment reduction is apparently enough to more than offset the mean volume expansion within the layer. From the photographs it is not clear what effect the heat release has had on the dynamics of the large structure that might account for this greatly reduced entrainment. Nevertheless the presence of a large structure remains clear at least up to the temperature rises and Reynolds numbers in this experiment.

A series of photographs of nitrogen-nitrogen shear layers was also taken (Figures 3.5 to 3.8), using the same velocities as for the previous set. The maximum

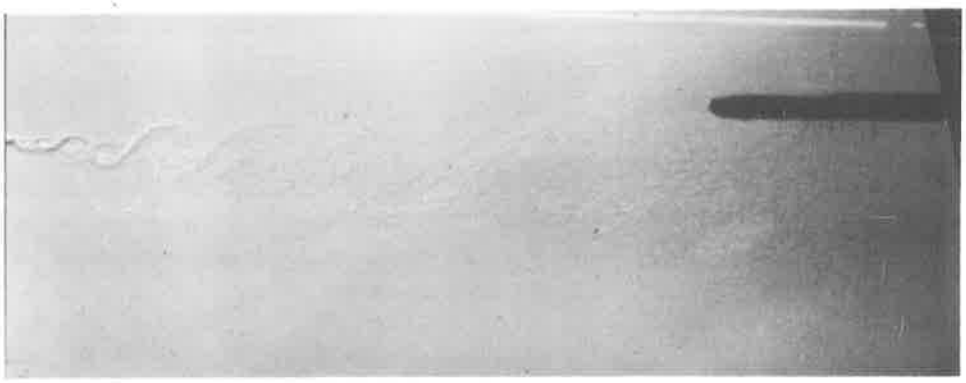

(a)

(b)

FIGURE 3.5 Simultaneous Blue, (a) and UV, (b) Shadowgraphs of Reacting N_2/N_2 Shear Layer

Upper Stream 25 ms^{-1} $C_{0\ NO}$ = 5.0%

Lower Stream 5 ms^{-1} $C_{0\ 03}$ = 0.1%

(a)

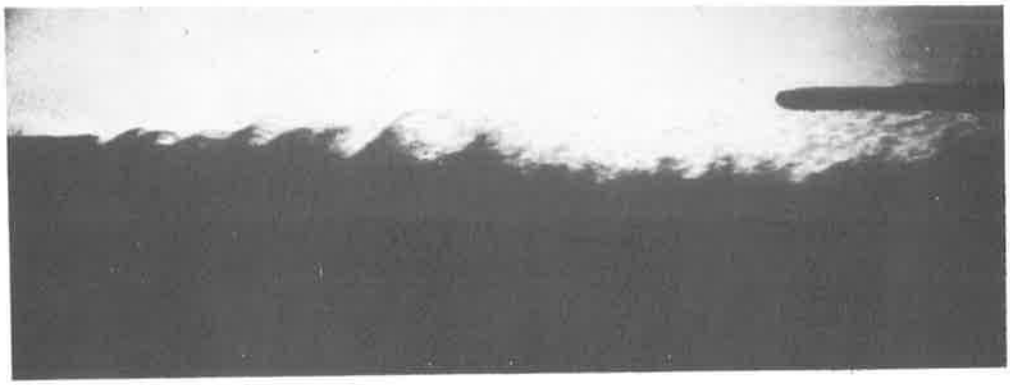

(b)

FIGURE 3.6 Simultaneous Blue, (a) and UV, (b) Shadowgraphs of Reacting N_2/N_2 Shear Layer

Upper Stream 25 ms^{-1} $C_{0\ NO}$ = 5.0%

Lower Stream 5 ms^{-1} $C_{0\ 03}$ = 2.4%

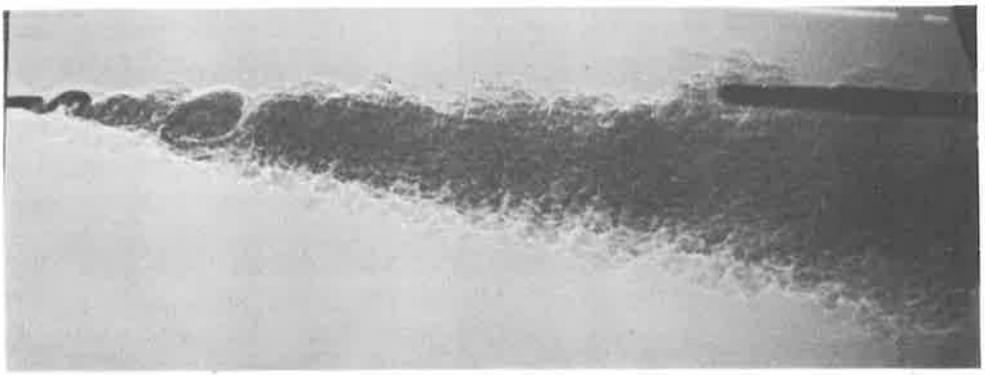

(a)

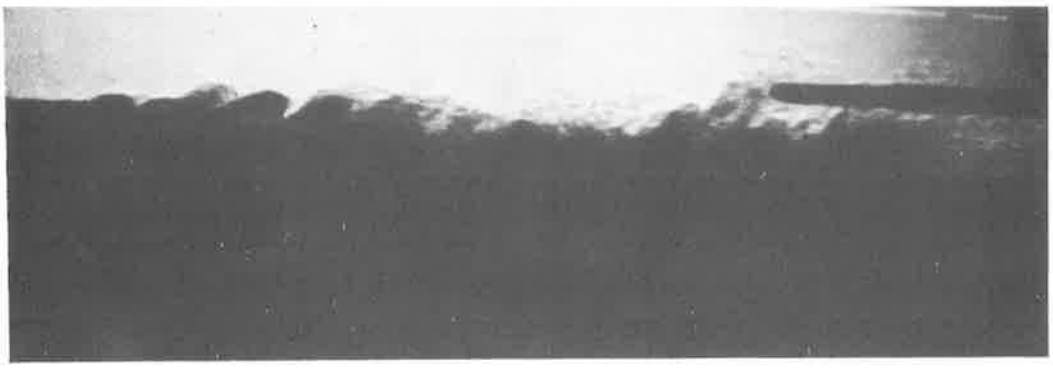

(b)

FIGURE 3.7 Simultaneous Blue, (a) and UV, (b) Shadowgraphs of Reacting N_2/N_2 Shear Layer

Upper Stream 25 ms^{-1} $C_{0\ NO}$ = 5.0%

Lower Stream 5 ms^{-1} $C_{0\ 03}$ = 3.8%

(a)

(b)

FIGURE 3.8 Simultaneous Blue, (a) and UV, (b) Shadowgraphs of Reacting N_2/N_2 Shear Layer

Upper Stream 25 ms^{-1} $C_{0\ NO}$ = 5.0%

Lower Stream 5 ms^{-1} $C_{0\ 03}$ = 7.8%

mean temperature rises are 4.4, 77, 98, and 122°C respectively. Since the refractive indexes of the free stream gases are the same only the thermal gradients (not the species gradients) will be visible. For this reason, and due to the high level of small scale turbulence, large scales in the layer are not as clear as in the helium-nitrogen layer. However, there is evidence of large scale clumping of the nitrogen dioxide in Figure 3.8. These nitrogen-nitrogen reacting shear layers show similar effects of heat release as the nitrogen-helium shear layers. The overall growth rate changes very little, and the finest turbulence scales are progressively suppressed.

Looking at the UV pictures of ozone associated with all the above figures, it is clear that the penetration of ozone across the layer depends on the reactant concentration ratio ξ, and the level of small scale turbulence. (It must be remembered that the frequency of UV light used was highly sensitive to ozone, and that any mean ozone concentration above about 0.2% will be opaque). The engulfment process is particularly clear in Figure 3.3 at $x \doteq 0.5$. The ozone carrying stream is entwined into the periphery of the clump of vorticity, and carried around by it while reaction is occuring at the interface between the two gas streams. This appears to be occuring mainly by laminar diffusion from both sides, and is seen to thin down the "tongue" of ozone until it disappears entirely before achieving ½ a rotation of the large structure. The effect of introducing some small

scale turbulence can be observed by contrasting this with a structure further downstream at $x \doteqdot 0.8$, where the "tongue" of ozone is much more rapidly consumed, particularly from the inside edge where there is a higher level of turbulence. A similar behaviour is seen in the nitrogen-nitrogen shear layer pictures (e.g., Figure 3.6) but the small scale turbulence is even more energetic and results in a comparatively short life of entrained ozone. Clearly, increasing the ozone concentration relative to nitric oxide concentration causes ozone to penetrate further across the layer, and in the case of Figure 3.8, ozone has become the majority species (i.e, there is an excess of ozone after all the nitric oxide is burnt) almost throughout the layer. These pictures provide a qualitative support for the PDFs measured by Konrad (1977), (see Appendix A1), if it is borne in mind that mixtures of mixture fraction c where $0 \leq c < c_s$ appear transparent to the UV light, and mixtures where $c_s < c \leq 1$ appear opaque.

The mechanics of the large structure under conditions of heat release can be usefully studied prior to transition. The growth rate and entrainment rate are evidently quite similar before and after transition, the predominant change being an increase in the molecular scale mixedness (Konrad 1976, Breidenthal 1978). Figure 3.9 shows two flows with temperature rises of 10 and 160°C respectively. The maximum Reynolds number in each case is about 10^4.

(a)

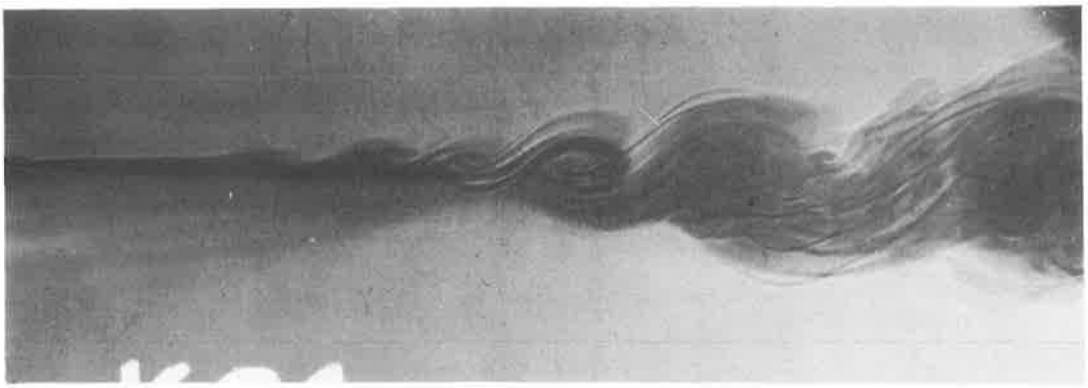

(b)

FIGURE 3.9 Blue Shadowgraphs of Low Speed Reacting N_2/N_2 Shear Layers
Upper Stream $5\ ms^{-1}$
Lower Stream $1\ ms^{-1}$

(a) $\overline{\Delta T}_{max} \doteq 10K$

(b) $\overline{\Delta T}_{max} \doteq 160K$

The absence of fine scale turbulence permits a clear view of a dramatic change in the character of the large structures. A measure of the relative strength of vorticity clumping can be seen in the width of the connecting braid between adjacent structures, and by this measure alone it is observed that the vorticity clumping is weakened with increasing reaction. Although the far field strength of the induced velocity field around an isolated patch of vorticity depends on the total vorticity, not on how it is distributed, the induced velocity in the near field, being a summation effect of distributed vorticity will be somewhat less. This will tend to inhibit two of the mechanisms responsible for entraining free steam fluid into the layer. The first is the entwining process, causing a particular eddy to grow by simple acquisition of fluid and the second is the vortex pairing process, which is observed to entrain by engulfment of free steam fluid.

A further effect on entrainment, present after transition, is that due to the wiping out of the higher frequency turbulence. However this is a small component of the total entrainment (Konrad reports eight percent).

3.1.1 The Role of Baroclinic Torque

The possible action of baroclinic torque† in causing non-reacting shear layers with unequal free stream densities to have unequal entrainment rates from each of the free

---

† Many of the ideas in this section arose during discussions with Professor G.L. Brown.

streams is discussed in section 3.5. The baroclinic torque action is used to show how the vorticity is transferred to the less dense side of the layer and thereby induces a greater proportion of less dense fluid to enter the layer. Baroclinic torque is a result of non-aligned density gradient and acceleration vectors, which are obviously a feature of mixing flows with chemical heat release. The derivation of the expression for baroclinic torque from Euler's equation is relatively simple, but summarized here for the sake of completeness.

Euler's equation

$$\frac{\partial \underset{\sim}{u}}{\partial t} + (\underset{\sim}{u} \cdot \underset{\sim}{\nabla})\, \underset{\sim}{u} = -\frac{1}{\rho} \underset{\sim}{\nabla} p + \underset{\sim}{g}$$

Taking the curl, and neglecting gravity

$$\frac{\partial \underset{\sim}{\omega}}{\partial t} + \underset{\sim}{\nabla} \times (\underset{\sim}{u} \cdot \underset{\sim}{\nabla})\, \underset{\sim}{u} = -\left(\underset{\sim}{\nabla} \times \frac{\underset{\sim}{\nabla} p}{\rho}\right)$$

$$\frac{\partial \underset{\sim}{\omega}}{\partial t} + (\underset{\sim}{u} \cdot \underset{\sim}{\nabla})\, \underset{\sim}{\omega} = \frac{1}{\rho^2} (\underset{\sim}{\nabla} \rho \times \underset{\sim}{\nabla} p)$$

substituting for $\underset{\sim}{\nabla} p$ from Euler's equation gives

$$\frac{D \underset{\sim}{\omega}}{Dt} = -\frac{1}{\rho} \left(\underset{\sim}{\nabla} \rho \times \frac{D \underset{\sim}{u}}{Dt}\right)$$

That baroclinic torque is relevant to the question of entrainment reduction in the reacting shear layer depends on the view that the mechanics of the layer are controlled by large structure which is basically two dimensional. Some idea of the distribution and action of baroclinic torque can be obtained by considering the mean density gradient and acceleration vector around the large structure shown in Figure 3.9. It is shown in

Appendix A that NO_2 concentration, as seen in Figure 3.9, is analogous to temperature rise (or density decrease) since the Schmidt and Lewis numbers are approximately one. An envelope drawn along the interface of this hot (turbulent) region with the non-turbulent free stream fluid then defines a surface normal to the mean density gradient. Such a surface is shown schematically as a dashed line in Figure 3.10, superimposed on a representation of the mean streamlines (where the observer is moving with the large structure). The flow pattern shown is similar to that given by Patnaik, Sherman and Corcos (1976). Careful inspection of the vector product of $\nabla\rho$ and $\frac{D\tilde{u}}{Dt}$ around the dashed envelope indicates that the dominant contribution to the vorticty by baroclinic torque action occurs at the points labelled 'A', and this contribution is in the same direction as the general circulation. Control volume analysis shows that in any given length of the layer, the mean total circulation must remain constant, implying that the vorticity at points A is growing at the expense of the vorticity concentrated in the core of the large structures and/or in the braids. This action is qualitatively consistent with the effect of heat release shown in Figure 3.9, and provides an explanation for the observed reduction in entrainment rate of free stream fluid. The crucial feature is the weakened near field induced velocity, due to the more diffuse vorticity. In particular, components of velocity in the y direction will be relatively weaker, thereby slowing both the entwining and engulfment mechanisms

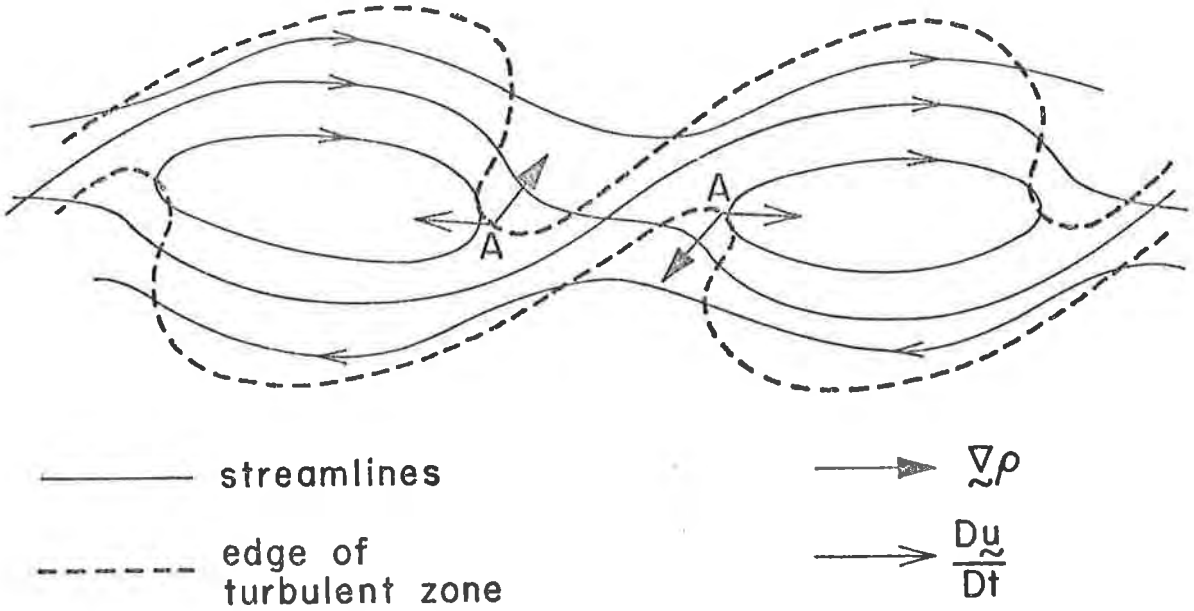

Fig. 3.10 Illustration of Baroclinic Torque Action in the Reacting Shear Layer with Heat Release.

responsible for most of the entrainment.

3.2 Mean Temperature Profiles

3.2.1 Comparison Between These Experimental Results and the Non-Reacting PDF Solution

The present data, and that of Konrad were taken at different velocity ratios, vis r = 0.22 and 0.38 respectively, but at similar Reynolds number. In order to compare the two, the data were scaled by the maximum slope thickness. Figure 3.11 shows both velocity profiles and y = 0 represents the dividing streamline calculated as described in Appendix B. The reasons for the very slight differences in profile shape are not clear but it seems unlikely to be due to some effect of heat release as the maximum temperature rise was only 20°C. They have been plotted together to confirm the similarity form of the profiles and particularly to clarify the relative positions of the temperature profiles shown on the same figure. The typical result shown exhibits a widened and rightward shifted inferred temperature profile. Inspection of a series of runs made with varying ξ and $\overline{\Delta T}_{max}$ confirmed this trend. In a sample of seven of these results, the mean shift of the position of $\overline{\Delta T}_{max}$ was $0.2\delta_\omega$, and the standard deviation in the sample was $0.11\delta_\omega$. For the purposes of comparing widths of mean temperature profiles, if δ_T, a half maximum amplitude width is defined, then the mean value of δ_T/δ_ω in the above sample is 0.84, compared with 1.26 for the inferred temperature profiles.

The value of $\overline{\Delta T}_{max}$ is used later as a parameter for

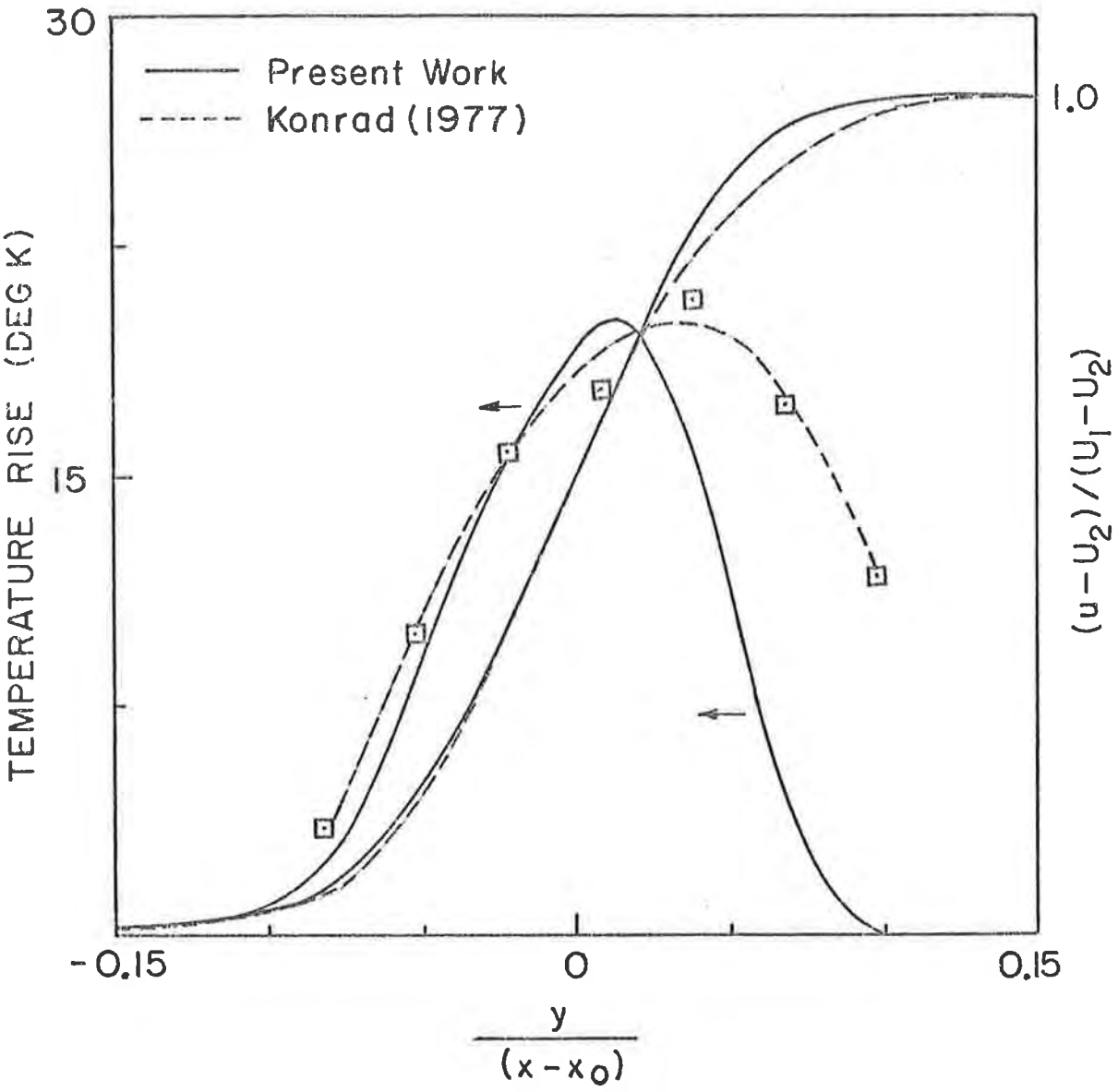

Fig. 3.11 Comparison of Velocity and Temperature Profiles.

for comparison between experimental and inferred results, since it is a readily identifiable point on any temperature profile which is directly dependent on the entrainment and mixing processes in the shear layer. Detailed results relating to different $\overline{\Delta T}_{max}$ in the experimental and inferred profiles are presented in Section 3.4.2.

It is not clear why these differences between the inferred and measured temperature profiles exist. It is possible that there could be some effect of finite reaction rate being more pronounced on the high speed side, but increasing the reactant concentration by a factor of five (thereby reducing τ_{chem} by the same order) does not appear to change the observed behaviour. There is some uncertainty about the signal to noise ratio of the composition probe used by Konrad to determine the PDFs in his uniform density flow† consisting of a mixture of helium and argon flowed with nitrogen on the other side of the layer. This was not a problem in his helium-nitrogen shear layer data since the signal was much stronger. However, when inferred and measured temperature profiles for a helium-nitrogen layer are plotted (Figure 3.12) the discrepancy is still present. For this figure the experimental profile was obtained for the same flow parameters as Konrad's data (r = 0.38, s = 7.0) and since the

---

† Private communication, Professor G.L. Brown.

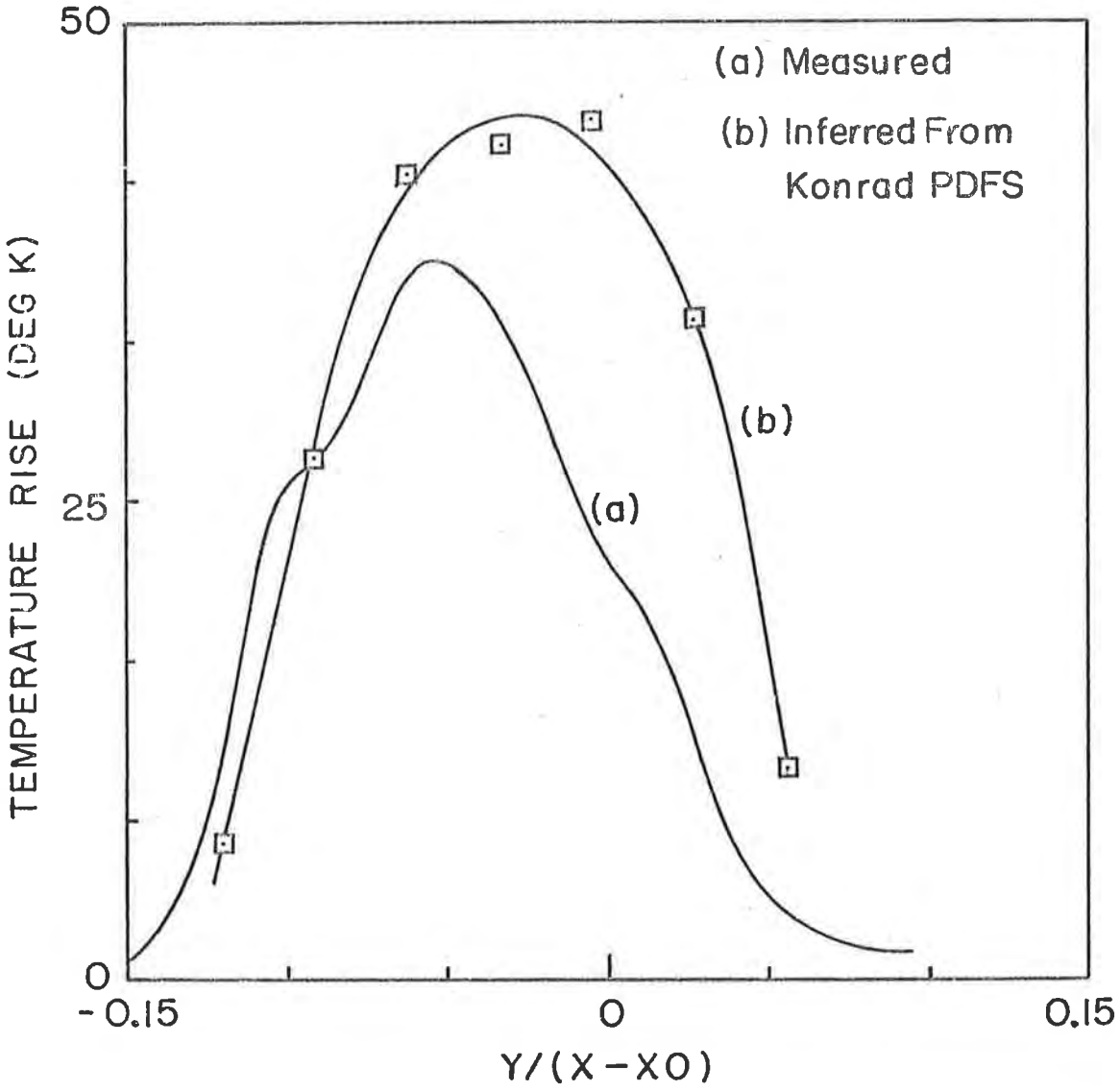

Fig. 3.12 Comparison of Temperature Profiles.

the dividing streamline could not be determined from this experimental data, its position was established by matching the $\overline{\rho u^2}$ profile with Konrad's.

3.2.2 Calculation of the Mixture Fraction PDFs from the Experimentally Measured Temperature Profiles - the Inverse Problem.

In Appendix A it is shown how the temperature at a point can be calculated from the mixture fraction PDF and the free stream reactant concentrations, given the heat release of the reaction, the specific heats, and the assumption of infinite reaction speed. In this way it was possible to infer temperature rises from the non-reacting PDF measured by Konrad, although the procedure is strictly only valid for negligible temperature rise because the PDFs could be expected to change under heat release conditions. The solution for the mean temperature at a given location is simply

$$\overline{\Delta T}\ (\xi,\ C_{0\ NO}) = \int_0^1 p_c(c)T(c,\ \xi,\ C_{0\ NO})dc \qquad (3.1)$$

where ξ = free stream reactant concentration ratio, $C_{0\ 03}/C_{0\ NO}$, and p(c) is the mixture fraction PDF. The function T is shown in Appendix A to be

$$T(c,\ \xi,\ C_{0\ NO}) = C_{0\ NO}\frac{\Delta H_f}{C_p}\left[c\ H(c_s - c) + \xi(1 - c)H(c - c_s)\right]$$

where $c_s = \xi/(1 + \xi)$, the stoichiometric mixture fraction, and H(c) is the Heaviside step function.

Define

$$T^* = \frac{T(c, \xi, C_{0\ NO})C_p}{C_{0\ NO}\ \Delta H_f} = cH(c_s - c) + \xi(1 - c)H(c - c_s) \tag{3.2}$$

(i.e., scale the temperature by the temperature rise that would be obtained if all the free stream NO were burned).

Then

$$\Delta T^* (\xi) = \int_0^1 p_c(c)\ T^* (\xi, c)dc \tag{3.3}$$

This result is an integral equation of the first kind for p(c) if $\Delta T^* (\xi)$ and $T^* (\xi, c)$ are known. Although T^* is known everywhere (equation 3.2), each run of the experiment determines ΔT^* for only a single value of the free stream reactant concentration ratio ξ.

It is clear from 3.3 however that the inert PDF p(c) could be obtained experimentally if $\Delta T^* (\xi)$ is measured for a wide range of values of ξ. The equation could be inverted in a number of ways, one of which would be to approximate the measured $\Delta T^* (\xi)$ by a function which closely fits the data over a wide range of ξ. This method of determining the PDF has great merit in that it does not require probes with the time response and spacial resolution to resolve the Kolmogorov microscale: the probe is only required to measure the time mean temperature rise. The main difficulty in the present application is the extent to which the approximation of fast chemistry is valid (see Appendix D).

The function p(c) was approximated by an arbitrary number n delta functions, each of area a_i, and n - 1 values of ΔT^* at various ξ were chosen.

$$\ddot{p}_c(c) = \sum_{i=1}^{n} a_i \delta(c_i) \qquad (3.4)$$

Equation 3.3 was then solved numerically by a matrix method to solve for the areas of n - 1 of the delta functions, the last being found from the PDF property relation

$$\int_0^1 p_c(c)dc = 1$$

i.e.,

$$\sum_{i=1}^{n} a_i = 1 \qquad (3.5)$$

(The n^{th} area is actually the sum of the areas of the delta functions at c = 0 and c = 1: this inverse problem cannot solve for them separately because at c = 0 and 1, T* = 0, giving these areas zero coefficients in the matrix equation). This attempt to solve for p(c) failed because the quantity and precision of the data were insufficient to establish the correct function for ΔT^*. The failure criterion was that $p_c(c)$ should be positive everywhere in the range $0 \leq c \leq 1$. A study of the disposition of the matrix equation revealed that it would be more sensitive to inaccuracies in ΔT^* as n increased. Consequently a value of n = 5 was chosen, because of all the experimental data, only 4 runs fell

within the acceptance conditions of (a) identical flow velocities and gases (b) low temperature rise ($\leqslant 70^{\circ}C$) (c) wide, well spaced range of ξ. The necessity of fitting a function ΔT^* was thereby avoided. The procedure was repeated for ΔT^* taken at seven values of η, thereby creating seven PDFs for the mixture fraction at these locations across the layer, Figure 3.13. In this figure it must be remembered that the absolute values of the delta functions corresponding to c = 0 and 1 are not determined, only their sum as explained above. This area has been arbitrarily distributed between the two pure mixtures in the same ratio as the mean mixture fraction resulting from a combination of the mixtures represented by the other four delta functions. With the exception of the end delta functions, Figure 3.13 can be compared with Konrad's PDFs shown on the next figure. Although the details in the PDFs inferred by the inverse method are lacking, it is apparent that the qualitative and quantitative features of both sets of PDFs are compatible, in particular the evidence of the same most probable mixture being present all across the mixing layer, while the mean mixture fraction is different at each location.

It was thought that by assuming a histrogram form for $p_c(c)$ instead of a delta function form would lead to a physically more satisfactory PDF. This form also produced regions of negative probability due to the measured ΔT^* being insufficiently precise. An examination

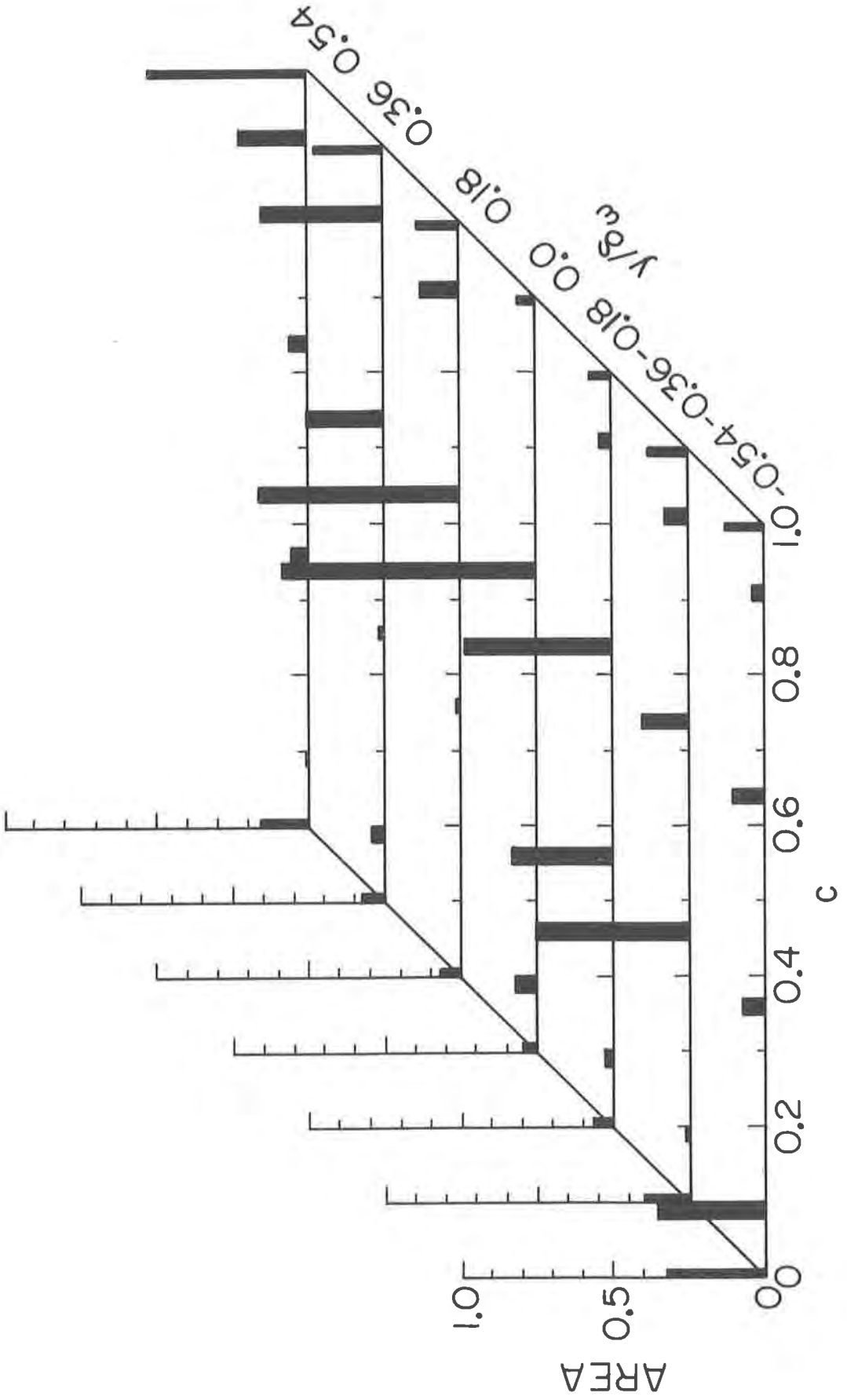

Fig. 3.13(a) Mixture Fraction PDF.

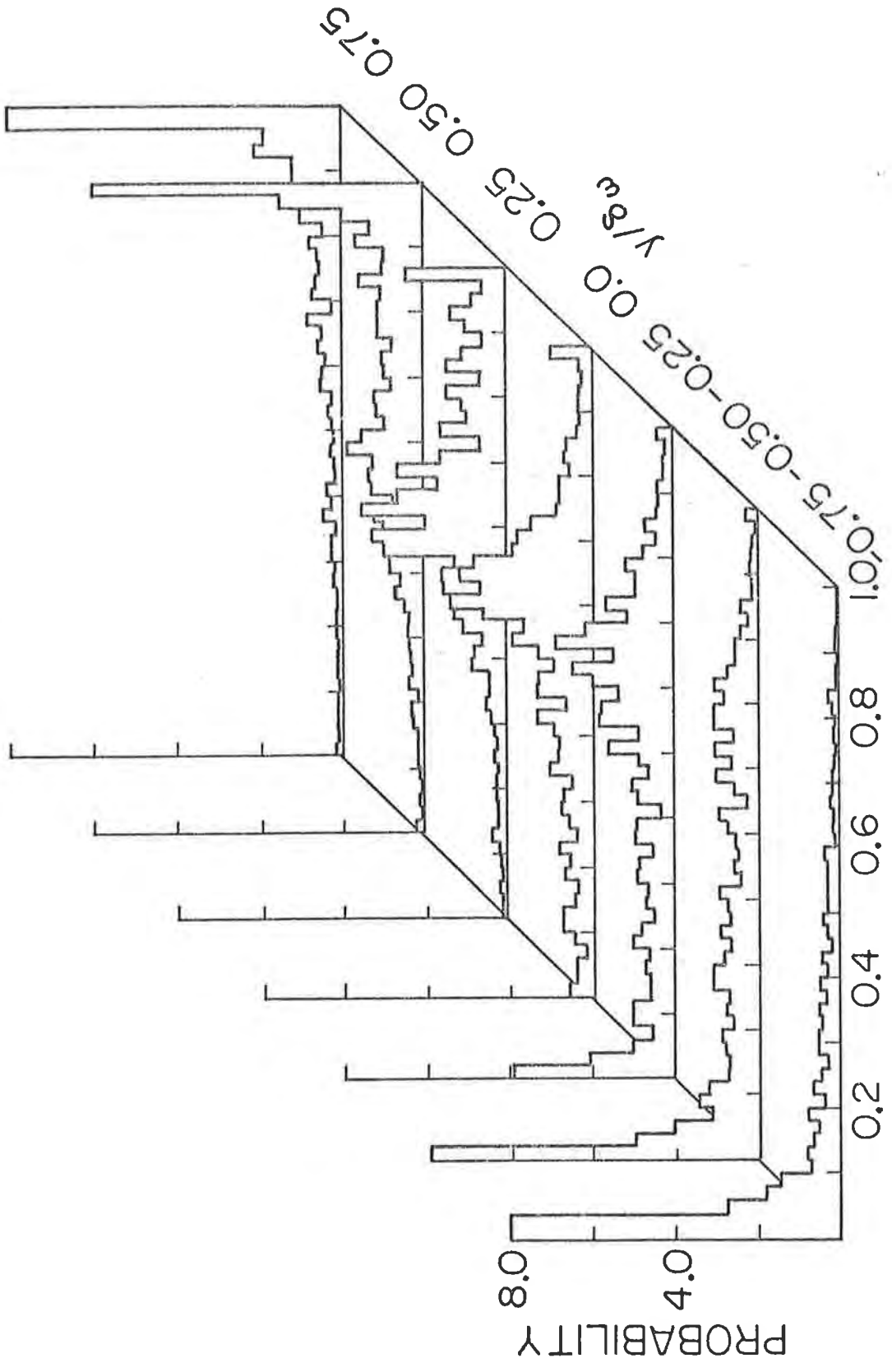

Fig. 3.13(b) Mixture Fraction PDF (From Konrad).

of the matrix solution procedure indicated that a histogram form of $p_c(c)$ produced relatively small pivoting coefficients in the matrix, making the solution very sensitive to inaccuracies in the data. Further refinements did not seem warranted until data for a more comprehensive set of values of ξ are obtained.

From the PDF it is possible to estimate $\overline{c_T}$, the mean mixture fraction in the turbulent zone. This is obtained by taking the mean mixture fraction of the PDF without the contribution of the delta functions at c = 0 and 1. A plot of $\overline{c_T}$ against the maximum slope thickness is shown in Figure 3.14 (a) for the PDFs of Konrad and the present work. The reason for the steeper slope of the present result is not clear, but it is consistent with the different widths of the temperature profiles given by the two sets of PDFs (see Figure 3.11). In fact, when the plot of $\overline{c_T}$ is scaled by δ_T instead of δ_ω, the agreement is remarkably good (Figure 3.14(b)) considering the vastly different methods of estimating $\overline{c_T}$. Despite this good agreement, the problem still remains as to why the $\overline{c_T}$ profiles are so different relative to their respective velocity profiles.

3.3 Effect of Free Stream Reactant Concentration Ratio

3.3.1 Product Formation

The concentration ratio, ξ, is defined in equation A4 as the ratio of the free stream ozone concentration to nitric oxide concentration. In this series of runs the nitric oxide concentration was held fixed at 0.5%

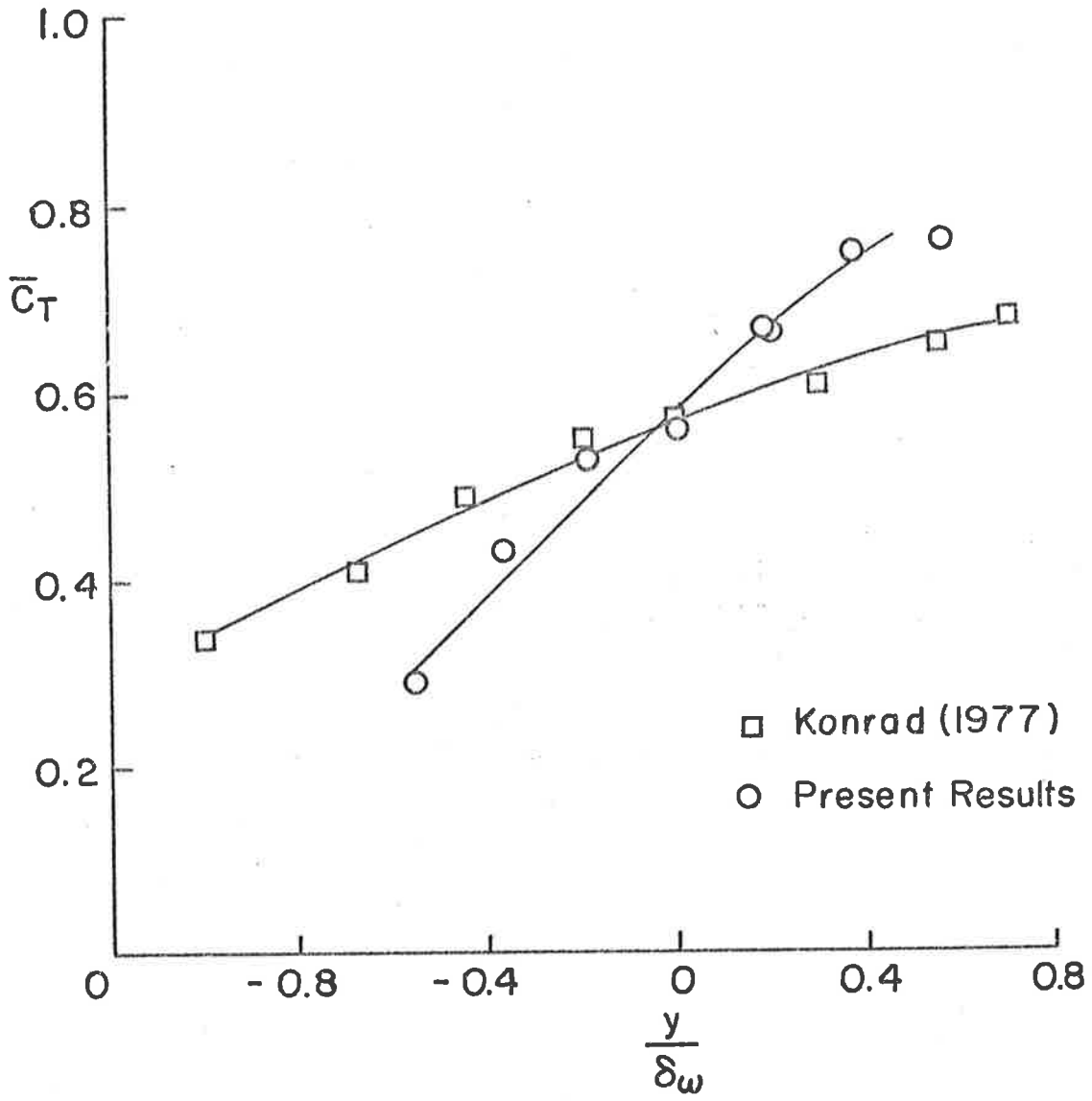

Fig. 3.14(a) Comparison of $\bar{c}_T$ vs. y/δ_ω.

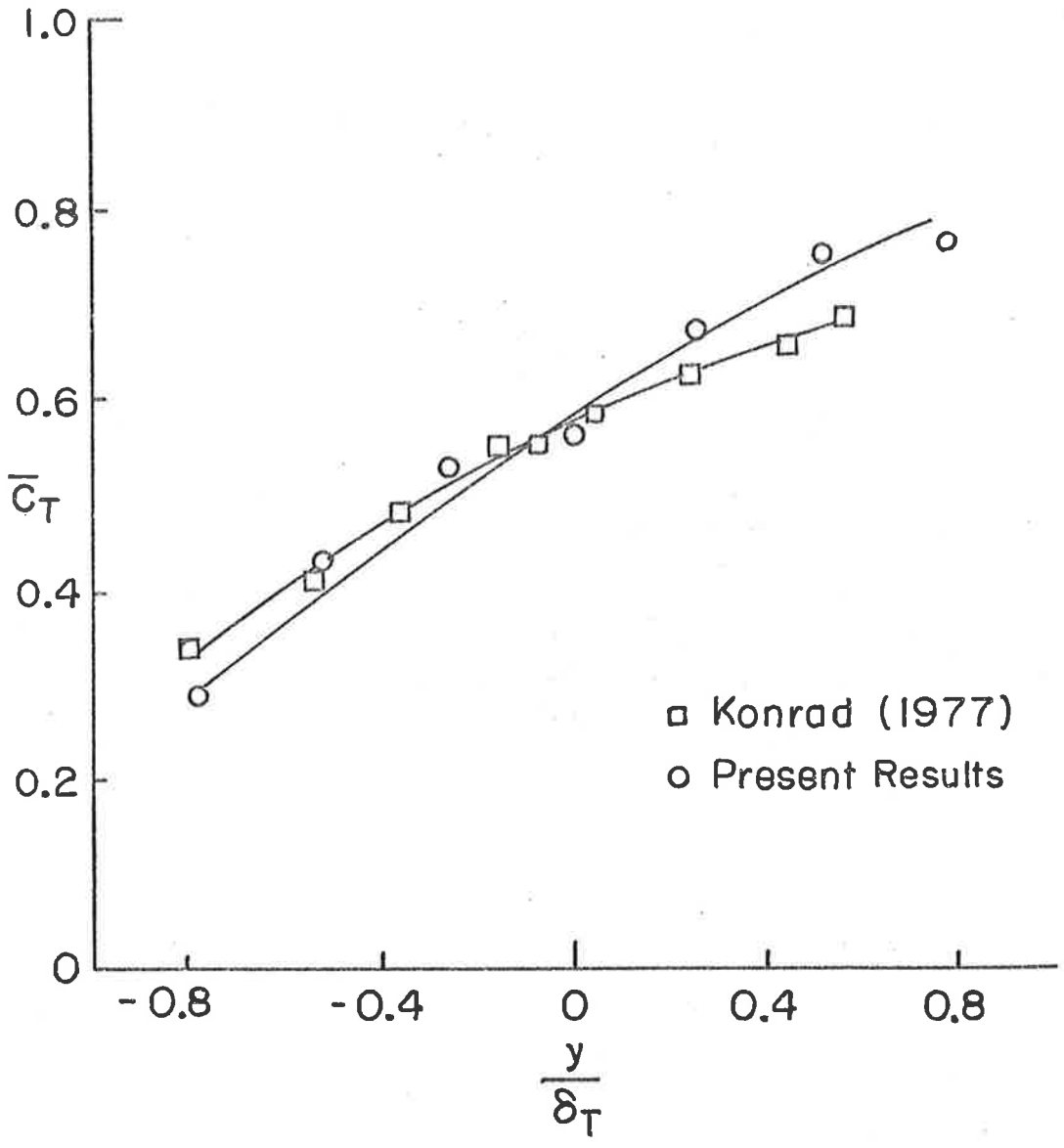

Fig 3.14(b) Comparison of $\bar{c}_T$ vs. y/δ_T.

while the ozone concentration varied from 0.5 to 7%, giving a range of ξ from 1 to 14. Free stream velocities were 5 and 25 ms^{-1} and the moveable side walls were adjusted for zero pressure gradient with zero reaction. The small negative pressure gradient (i.e., free stream acceleration) caused by the volume expansion in the reacting case was negligible at these temperature rises. The measured variable was maximum mean temperature rise obtained in a traverse 100 mm downstream of the splitter plate. This was measured with a tungsten cold wire (section 2.5.2), which was calibrated during the run with a thermocouple at a known fixed location near the dividing streamline. A reference junction was placed in one free stream. Response time of these thermocouples was approximately 0.4 sec in air at 5 ms^{-1}. (The faster thermocouples described in 2.5.2 were not available at this stage of the experiment).

The results obtained are plotted in Figure 3.15 and are compared with the predicted values obtained from the non-reacting PDFs measured by Konrad, as described in Appendix A. It is apparent that the maximum mean temperature rise predicted from the PDF is very close to the measured value at these low temperature rises. It is also evident that the temperature rise does not appear to asymptotically approach a limiting value, at least within this range of ξ.

The existence of an asymptote can be demonstrated mathematically in the case of infinite reaction speed.

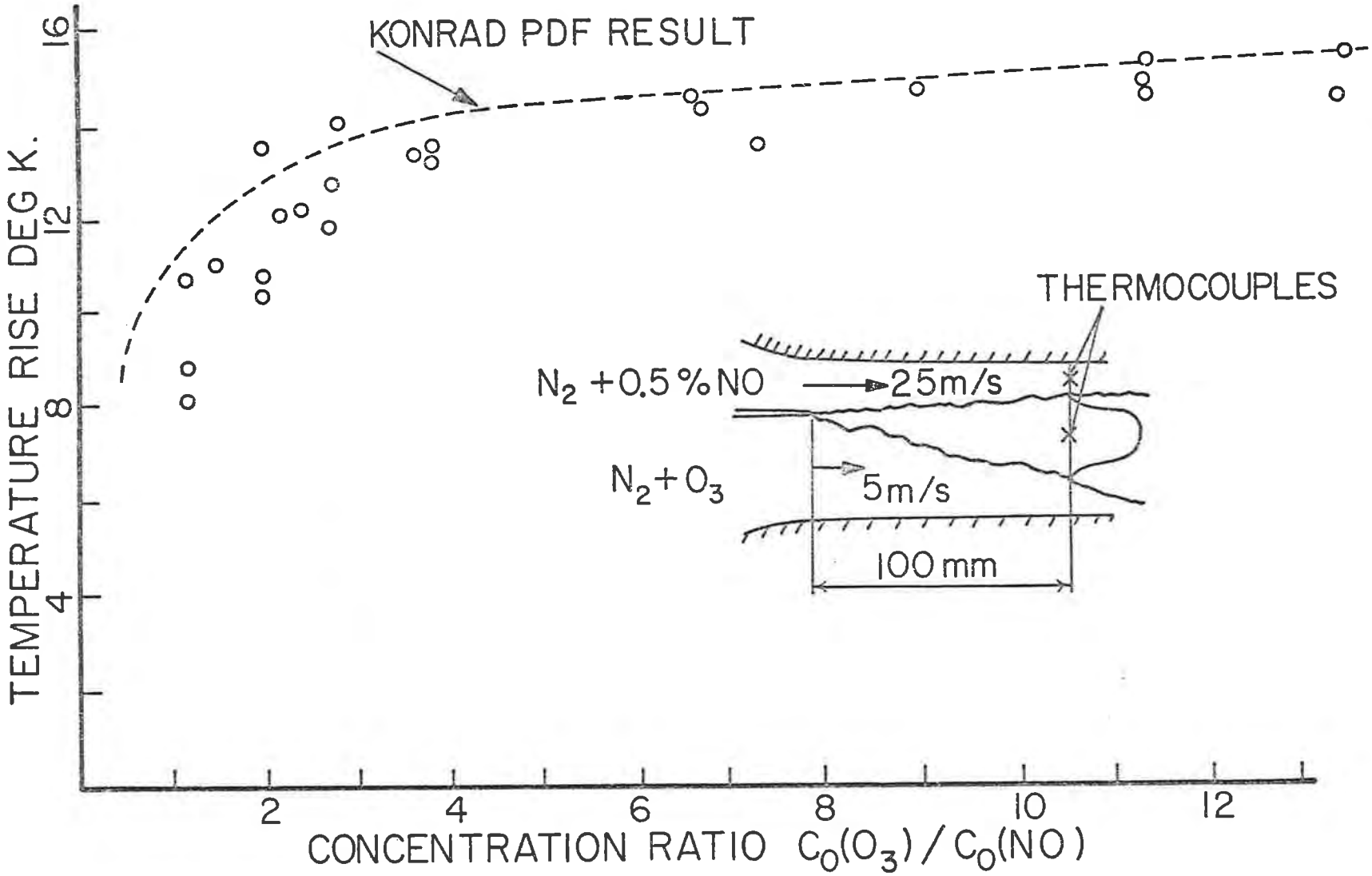

Fig. 3.15 Temperature vs. Concentration Ratio.

Given the mixture fraction PDF, $p_c(c)$, and the temperature rise as a function of mixture fraction $T(c)$ the mean temperature rise at a point is given by

$$\overline{\Delta T} = \int_0^1 p_c(c)T(c)dc \qquad (3.6)$$

where

$$T(c) = c\, C_{0\ NO}\, \frac{\Delta H_f}{C_p} \text{ for } c \leq c_s$$

$$(1 - c)\, C_{0\ 03}\, \frac{\Delta H_f}{C_p} \text{ for } c \geq c_s \qquad (3.7)$$

c_s is the stoichiometric mixture fraction, and is shown to be

$$c_s = \frac{C_{0\ 03}}{C_{0\ NO} + C_{0\ 03}} = \frac{\xi}{1 + \xi} \text{ in Appendix A.}$$

Hence

$$\frac{\overline{\Delta T}}{C_{0\ NO}\, \frac{\Delta H_f}{C_p}} = \Delta T^*(\xi) = \int_0^{\frac{\xi}{1+\xi}} c\, p_c(c)dc + \xi \int_{\frac{\xi}{1+\xi}}^1 (1 - c)\, p_c(c)dc \qquad (3.8)$$

We require the limit as $\xi \to \infty$ of ΔT^*, i.e., the limit as $\frac{\xi}{1+\xi} = 1$. Replacing $\frac{\xi}{1+\xi}$ with $1 - \varepsilon$ we write

$$\lim_{\xi \to \infty} T^* = \lim_{\varepsilon \to 0} \left[\int_0^{1-\varepsilon} c\, p_c(c)dc + \frac{1 - \varepsilon}{\varepsilon} \int_{1-\varepsilon}^1 1 - c)p_c(c)dc \right] \qquad (3.9)$$

Given that p(c) is a probability density function whose integral is therefore unity, the largest value of ΔT^* would occur in the limit as $\xi \to \infty$, only if $p_c(c)$ were a delta function arbitrarily close to c = 1. i.e., supposing $p_c(c) = \delta(1 - \alpha)$ then $\Delta T^* = \frac{\alpha}{\epsilon}$ for $\epsilon \geq \alpha$ and $1 - \alpha$ for $\epsilon > \alpha$.

Hence, the maximum possible value of ΔT^* is one which corresponds physically to a perfectly mixed stoichiometric mixture in which ξ approaches infinity.

In Appendix D, it is shown that the chemical reaction time is always decreasing with increasing reactant concentrations. This leads to the possibility of a Damkohler number effect, since at the lower ozone concentrations used in this experiment the reaction time becomes comparable with the larger turbulent time scales. The PDF solution assumes of course an infinite reaction speed and the effect of finite Damkohler number would be to give a lower temperature than predicted by the PDF solution. This may account for the average temperature being somewhat below the predicted values from the PDF at low values of ξ in Figure 3.15.

3.3.2 Skew of the Mean Temperature Rise Profile

Figure 3.16 plots three temperature profiles obtained over a wide range of concentration ratio, showing a skew in the profile toward the minority species side. For the sake of comparison individual profiles have been scaled to the same height. Figure 3.17 shows the same profiles inferred from the non-reacting PDF solutions with the same scaling. A detailed comparison between experimental and predicted profiles is made in Section 3.2

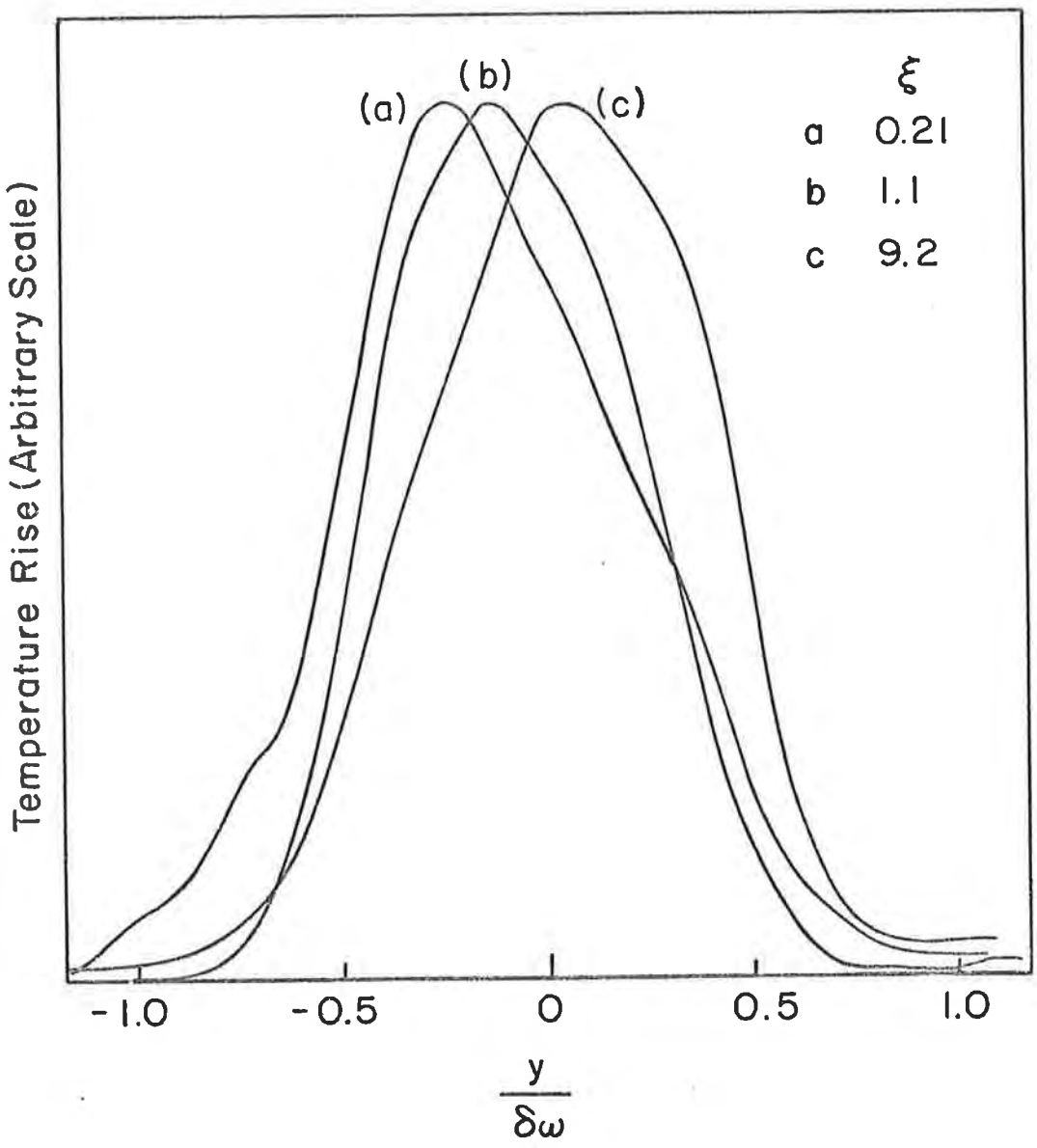

Fig. 3.16 Effect of ξ on Measured Temperature Profiles.

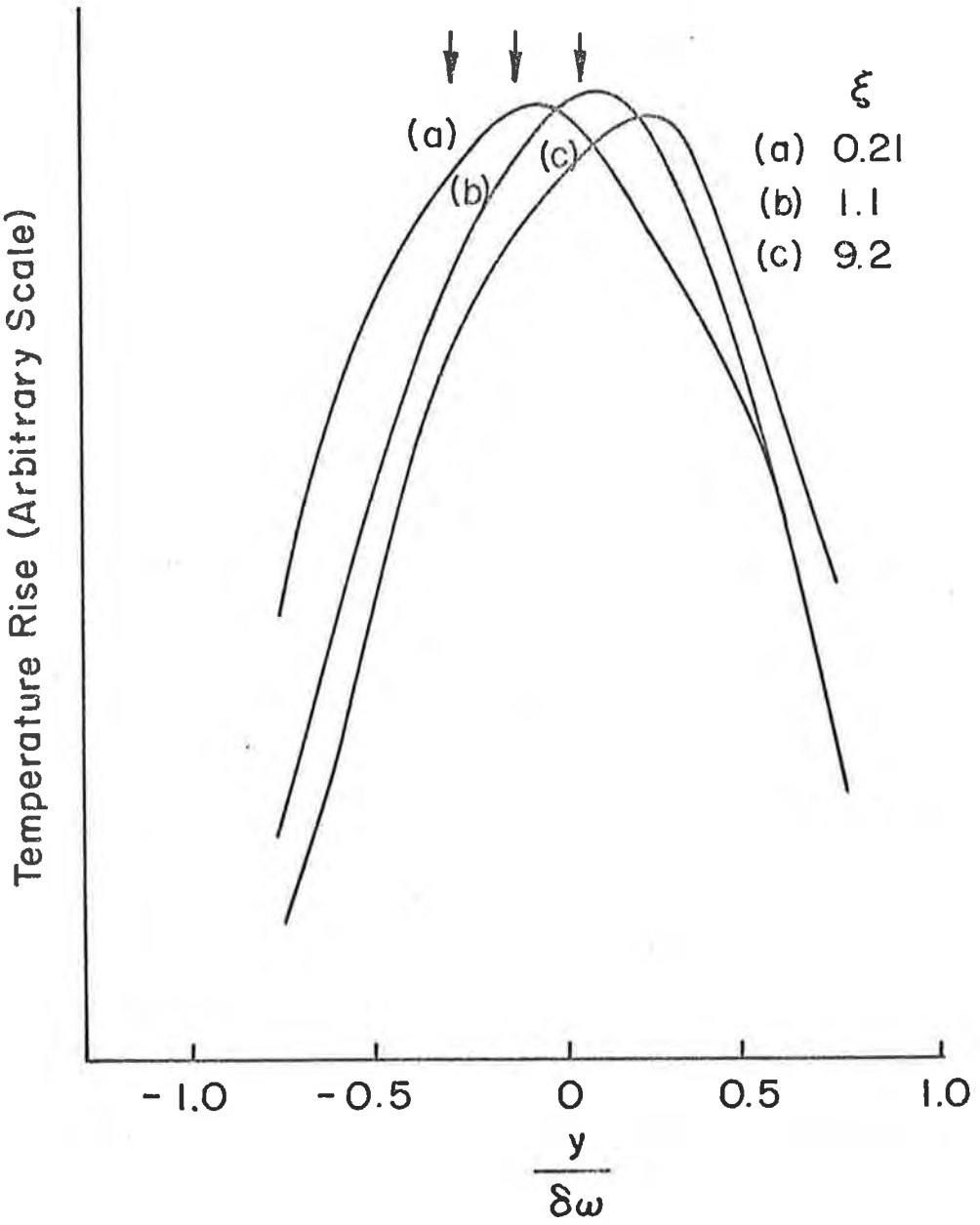

Fig. 3.17 Effect of ξ on Temperature Profiles Inferred from Konrad's PDFs.

but this discussion concerns the effects of changing ξ. The three arrows at the top of the figure indicate the position of the peak of the experimental profiles in 3.16. The rightward shift of the inferred profiles (discussed in Section 3.2) is evident here, but the relative displacement due to changing ξ are apparently very similar. The magnitude of this skew as a function of ξ becomes meaningful when it is compared to the skew obtained in a laminar diffusion shear layer (or a corresponding turbulent shear layer if the molecular diffusivities are replaced by assumed analogous eddy diffusivities).

The solution of the non-reacting, uniform density laminar diffusion shear layer in the temporal framework becomes the solution of the one dimensional species conservation equation with diffusion

$$\frac{\partial n_i}{\partial t} = D \frac{\partial^2 n_i}{\partial y^2} \qquad (3.10)$$

which has the similarity solution

$$\frac{n_i}{n} = \frac{\text{erf } (\eta) + 1}{2} \qquad (3.11)$$

where η is the similarity variable $\frac{y}{\sqrt{4DT}}$.

Since the number density is constant, $\frac{n_2}{n} = 1 - \frac{n_1}{n}$. Knowing the mixture fraction for any y it is simple to infer the temperature rise, using equation 3.7, and arrive

at a temperature profile for any given ξ, as shown in Figure 3.18. This analysis ignores the effect of heat on the density and diffusivities, but is adequate for the present purpose. In order to compare these temperature profiles with the experimental ones, the η coordinate was scaled by the maximum slope thickness of the species concentration profile (equation 3.11), in the same way as the experimental profiles were scaled by the maximum slope thickness (δ_ω) of the velocity profile.

Figure 3.19 shows the normalized temperature profiles given by the diffusion model for the same values of ξ as the three cases in Figure 3.16 and 3.17. The arrows indicate the positions of the peaks of the experimental profiles and show that the diffusion model gives a profile skew about twice as large as the skew actually measured in the turbulent flow.

This result is another clear demonstration of the role played by the actual PDF and the misleading picture that might be obtained if the turbulent flow were thought of as being in some ways analogous to a laminar problem but with eddy diffusivities replacing molecular diffusivities.

3.4 Effect of Heat Release

3.4.1 Velocity Profile and Entrainment

It was observed from the photographs that the spreading rate of the layer with heat release did not appear to be greatly changed. The velocity profiles presented in Figure 3.20 give an example of the apparent

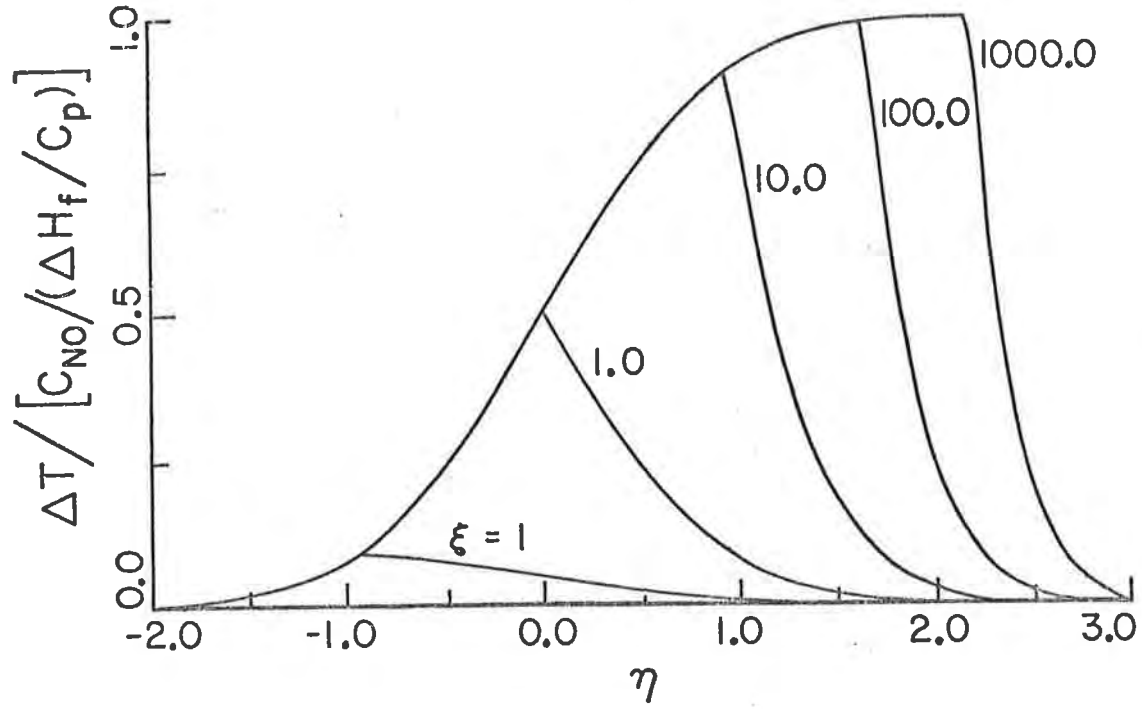

Fig. 3.18 Normalized Temp Rise Profiles, Laminar Diffusion Model.

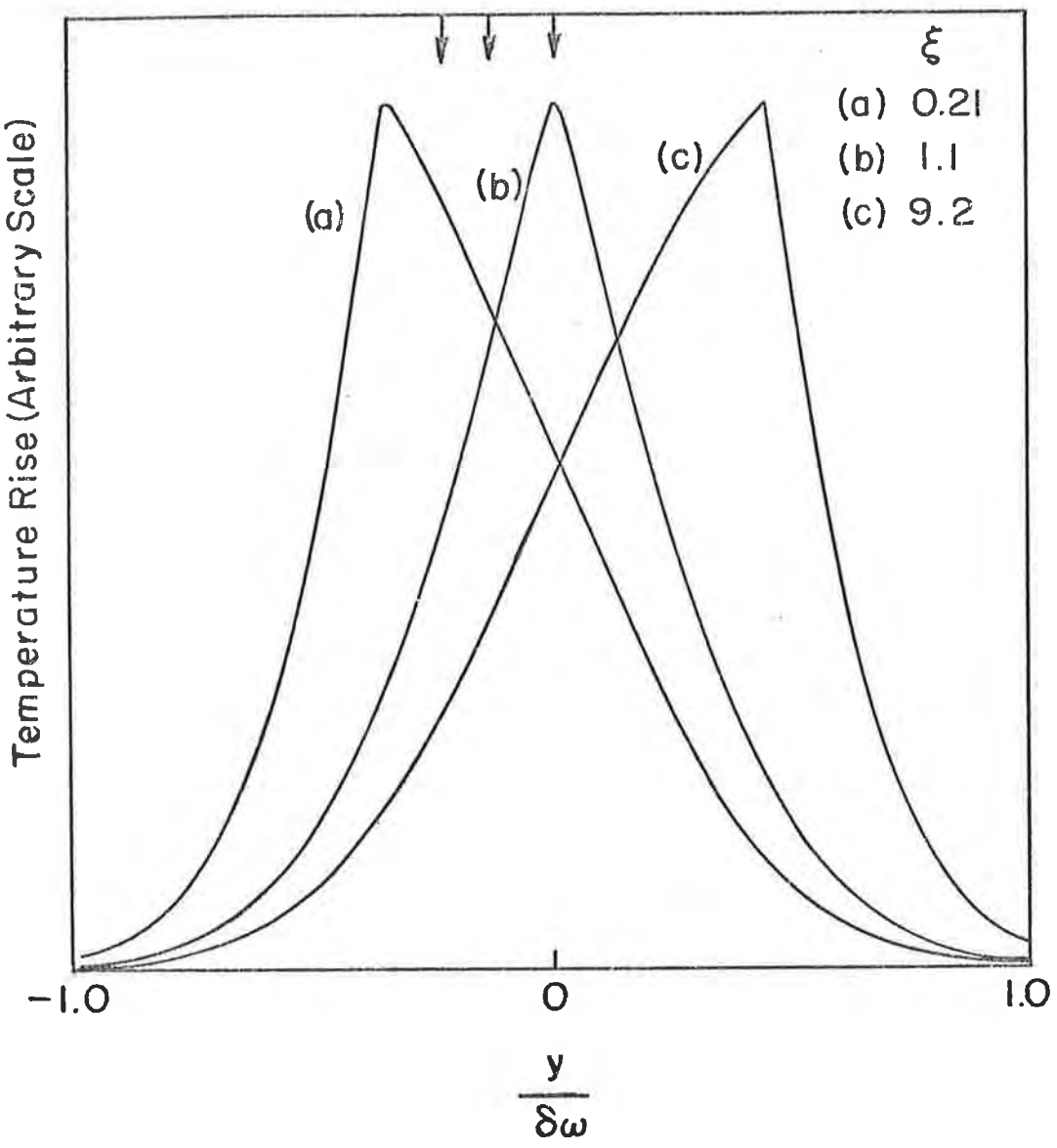

Fig. 3.19 Effect of ξ on Laminar Model Temperature Profiles.

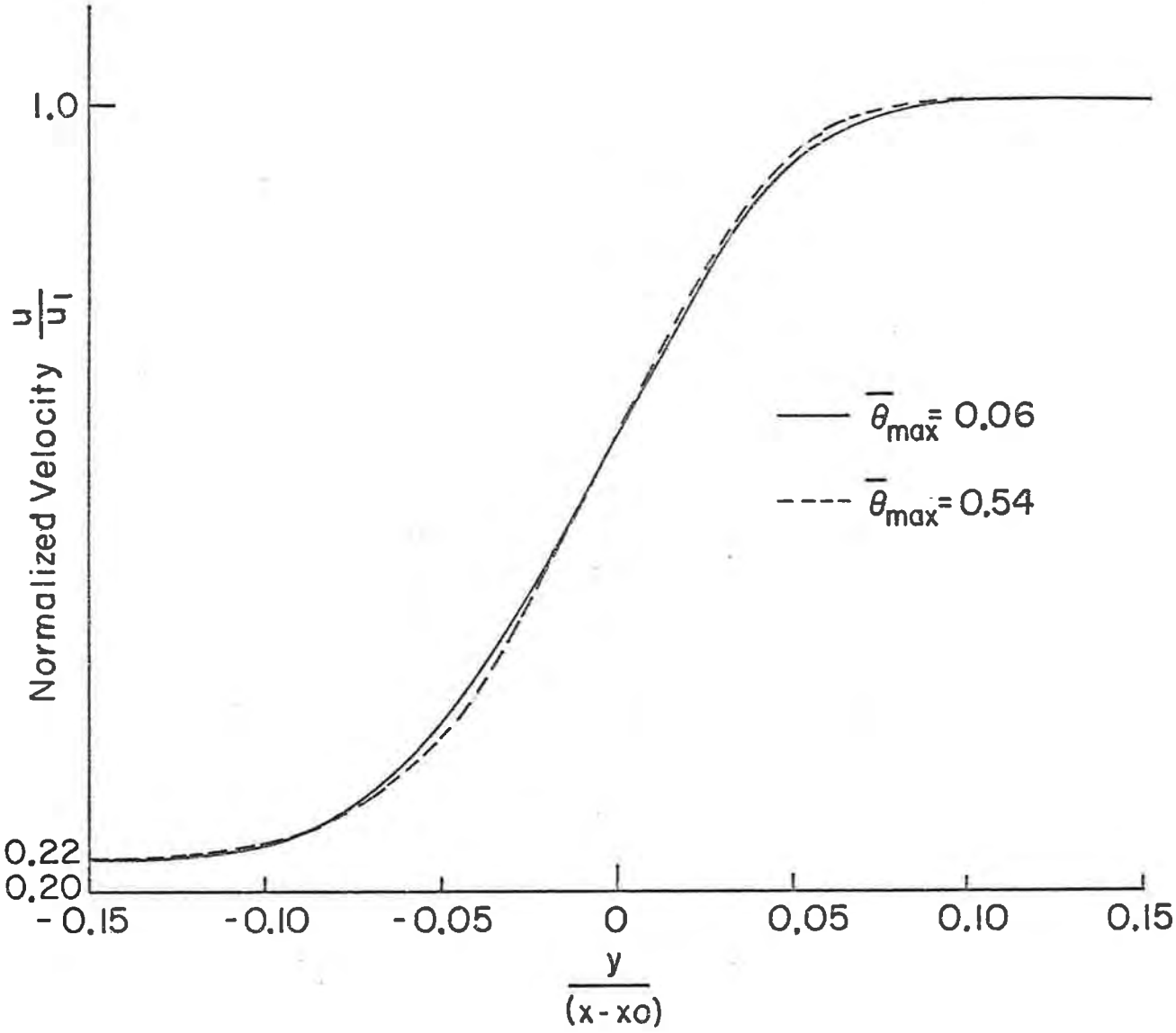

Fig. 3.20 Effect of Heat Release on Velocity Profile.

slight thinning of the layer at a particular downstream location with increasing heat release. Figure 3.21 plots $\delta_\omega/(x - x_o)$ against maximum mean temperature rise for layers of various concentration ratios. It is not strictly correct to interpret this quantity as the overall spreading rate because the value of x_o, the displacement of the effective origin of the fully developed layer from the splitter plate edge, is assumed constant, and was measured only in the non-reacting flow. Its determination in each reacting flow would have required a number of identical runs for each value of heat release, which was not a practical proposition in the present rig. Clearly, the effective origin will depend on the growth history of the laminar part of the layer, a process which is influenced by heat release as indicated by the photographic evidence. A study of a number of photographs of the flow with various heat release indicated that the change in x_o would have been of the order of 7 mm at $\overline{\theta}_{max} = 0.5$. ($\overline{\theta}_{max} = \overline{\Delta T}_{max}/T_\infty$.) This corresponds to a reduction of $(x - x_o)$ by about 6% over the range of these experiments, which implies that at any fixed value of x, about two thirds of the perceived thinning of the layer is due to transition delay, and one third due to reduced growth rate.

Even though the growth rate is only slightly reduced it is obvious that the entrainment of mass into the layer has been strongly reduced, as shown in Figure 3.22 which plots the normalized mass flux against $\overline{\theta}_{max}$.

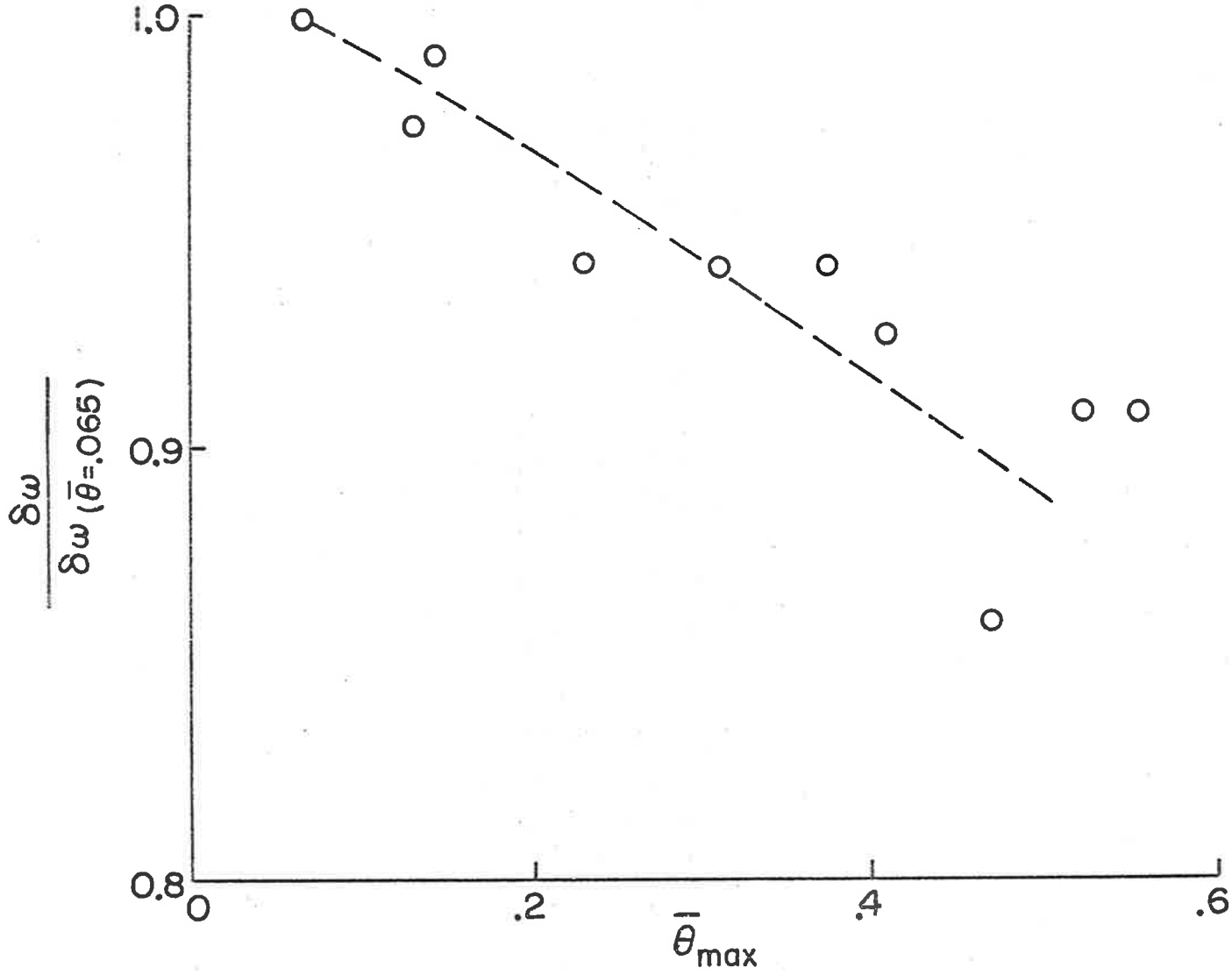

Fig. 3.21 Effect of Heat Release on Shear Layer Thickness.

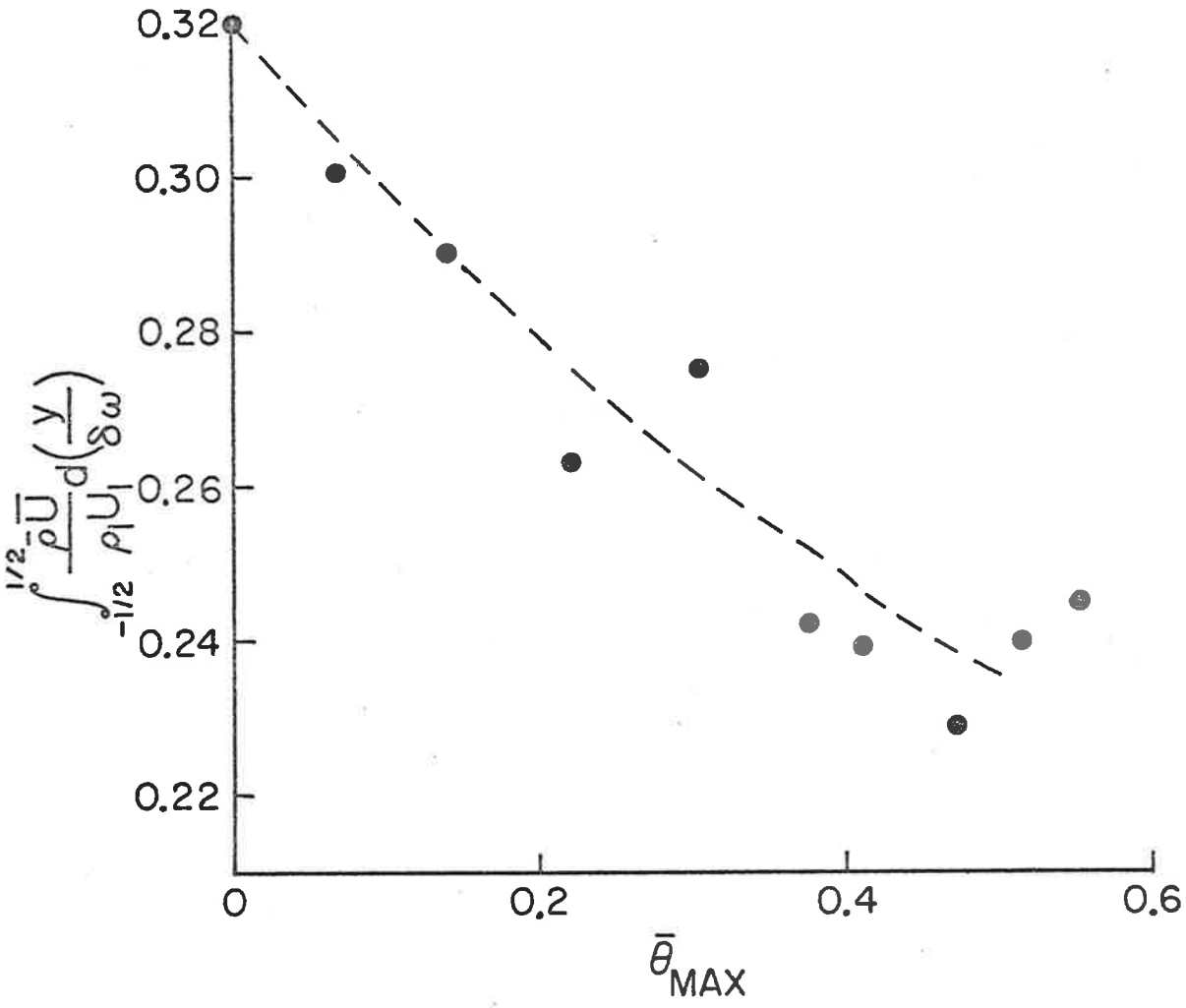

Fig. 3.22 Effect of Heat Release on Mass Flux in the Shear Layer.

The integration limits for the mass flux were chosen at $y = \pm \frac{\delta_\omega}{2}$, these points being relatively insensitive to local purturbations in the mean velocity or temperature profile. Inspection of Figures 3.21 and 3.22 indicates that at $\overline{\theta}_{max} = 0.5$, corresponding to a maximum mean density decrease of 33%, the mass flow is reduced by approximately 10% due to thinning of the layer, and a further 15% due to the density decrease, a total decrease of 25%, As explained above, about two thirds of the thinning appears to be caused by the heat release delaying the early developmental stages of the turbulent shear layer.

3.4.2 Mean Temperature Rise

Although it is clear that the total entrainment is reduced by heat release, it is not obvious if the PDFs have changed or not. The temperature rise at a point is determined entirely by the mixture fraction PDF at that point. It is easy to show, from the analysis presented in Appendix A, that if the PDF is unchanged, and ξ is fixed, the mean temperature must be a linear function of the reactant concentration. Due to experimental constraints, it was not possible to make a large number of runs with precisely the same ξ. However it is not necessary to be confined to a fixed location and fixed ξ to observe evidence of the change in the PDF with increasing heat release. This can be seen by plotting $\overline{\theta}_{max}$ from the experimental profiles against that from the PDF inferred profiles (Figure 3.23) for the same reactant concentrations. The points shown

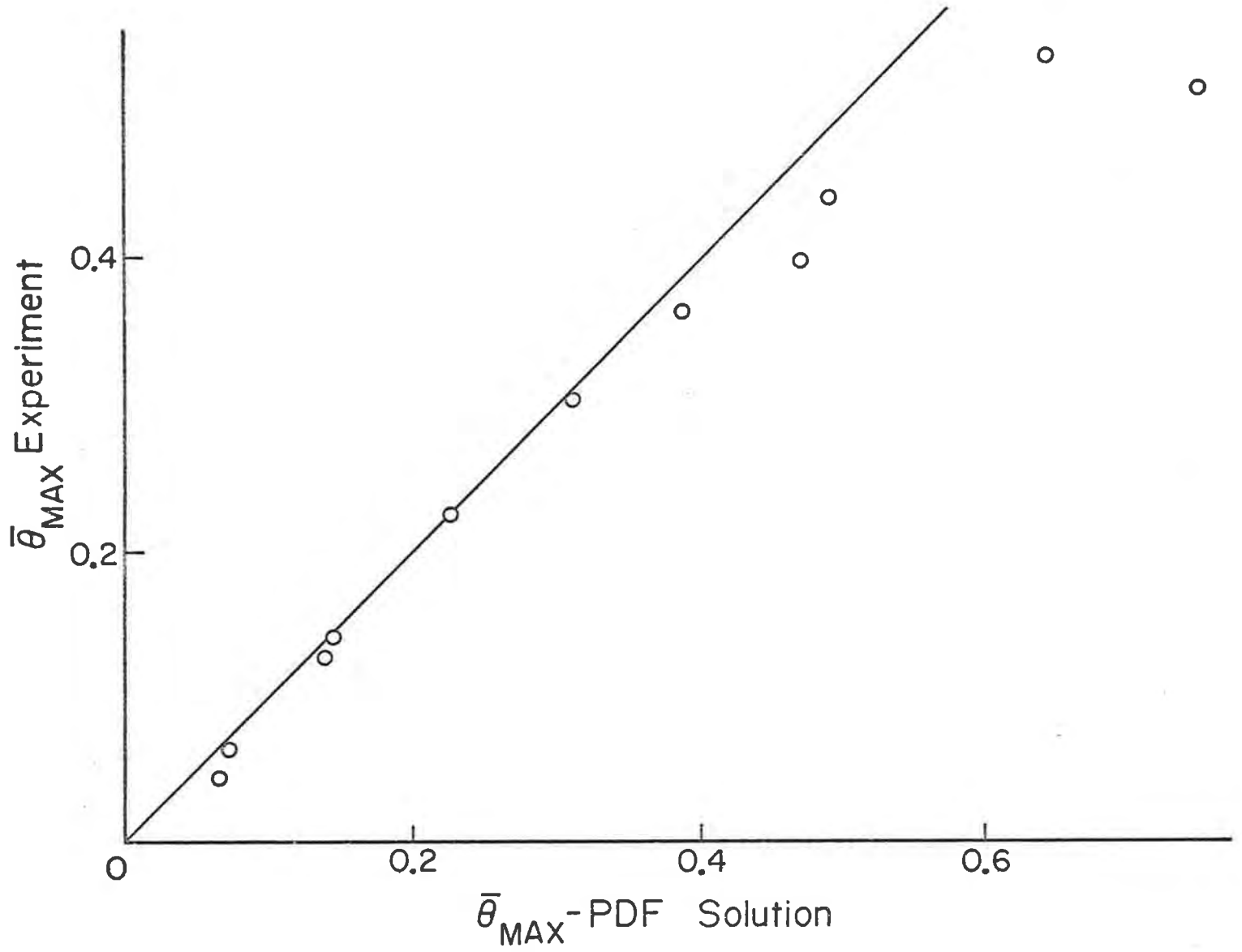

Fig. 3.23 Comparison of Measured $\bar{\theta}_{max}$ with $\bar{\theta}_{max}$ inferred from Konrad's Non-reacting PDFs. (Nitrogen Shear Layer)

correspond to a wide range of ξ, and the excellent agreement up to $\overline{\theta}_{max} \doteq 0.35$ tends to confirm the validity of the PDFs near the position of $\overline{\theta}_{max}$. Beyond the point where $\overline{\theta}_{max} = 0.35$, the heat release is evidently no longer passive - the actual PDF begins to alter significantly and the non-reacting PDF is no longer successful in predicting the temperature rise. In principle, the procedure used in Section 3.2 to determine a simplified PDF from a series of temperature measurements is also applicable to solve for the PDF in the flow with high heat release. However, this would require taking a series of runs all with the same high heat release and a wide range of ξ, a task outside the capabilities of the present apparatus, and indeed probably not feasible with the ozone-nitric oxide reaction due to the instability of concentrated ozone. Broadly speaking, two parameters which characterise any PDF are mixedness and mean mixture fraction. If we assume that the entrainment ratio is not significantly changed by the heat release (hence maintaining the same mean mixture fraction) then the fact that the temperature does not achieve the value predicted by the non-reacting PDF implies that the molecular scale mixedness must have decreased when $\overline{\theta}_{max} > 0.35$. We note that this is consistent with the flow visualisation presented in Section 3.1, where it was observed that the fine three dimensional scales were progressively suppressed by the heat release. Should this be the major cause of the deviation shown

in Figure 3.23, the crucial role of the small scales in mixing is apparent. It is interesting to compare the result of Konrad, showing that the mixedness at Reynolds numbers above the critical value (i.e. after transition) is about 25% higher than it was prior to transition. The increase in mixedness coincided with the appearance of the small scales.

3.5 Effect of Free Stream Density Difference on Product Formation

It has been established (Brown, 1974) that the relative entrainment rates of the free stream fluids in a turbulent mixing layer is dependent upon their relative densities. Irrespective of whether it is on the high velocity or low velocity side, more of the lower density stream is entrained than of the higher density stream. This property is clearly evident in the PDF of Konrad (Figure A2) in which the most probable concentration at almost all points across the layer is skewed to the helium side (c.f. the constant density PDF of Figure A1). One way of looking at the effect is to note that the entrainment rate of helium is about 3 times that of nitrogen, in contrast to the uniform density layer where the ratio of entrainment rate is about 1. The question as to why the variable density has such a significant effect on the PDF is considered later in this section. Whether this effect will lead to an increased or decreased product concentration (analogous to temperature rise) depends on the concentration ratio, ξ, of NO and O_3 in their respective free streams, that is, on the concentration c_s at which NO and O_3 are in chemical equivalence. Generally speaking, the highest mean product concentration is

expected when the ratio of NO and O_3 free stream concentrations corresponds to the entrainment ratio of the free streams. This is because at the most probable concentration (which corresponds roughly with the entrainment ratio), the chemical equivalence will be near unity.

To demonstrate the crucial effect of a free stream density ratio change, two runs were made with the same reactant concentrations, free stream velocities and streamwise pressure gradient (zero). The only difference was to change the high speed stream from nitrogen to helium. Nitrogen was used for the low speed stream in both cases, and the reactant concentration ratio ξ was 1. Despite an increase in the flame sheet temperature by a factor of 1.2† in the helium-nitrogen case, due to the reduced value of C_p, the maximum mean temperature rise in the turbulent layer fell to 0.6 of that in the nitrogen-nitrogen case. Figure 3.24 gives the experimental profiles. This result is in good agreement with the inferred temperatures calculated from Konrad's PDFs (see Section 3.2.1). The mean mixture at the dividing streamline now

---

† If the Lewis number D/α is one and the diffusivities of all species are equal.

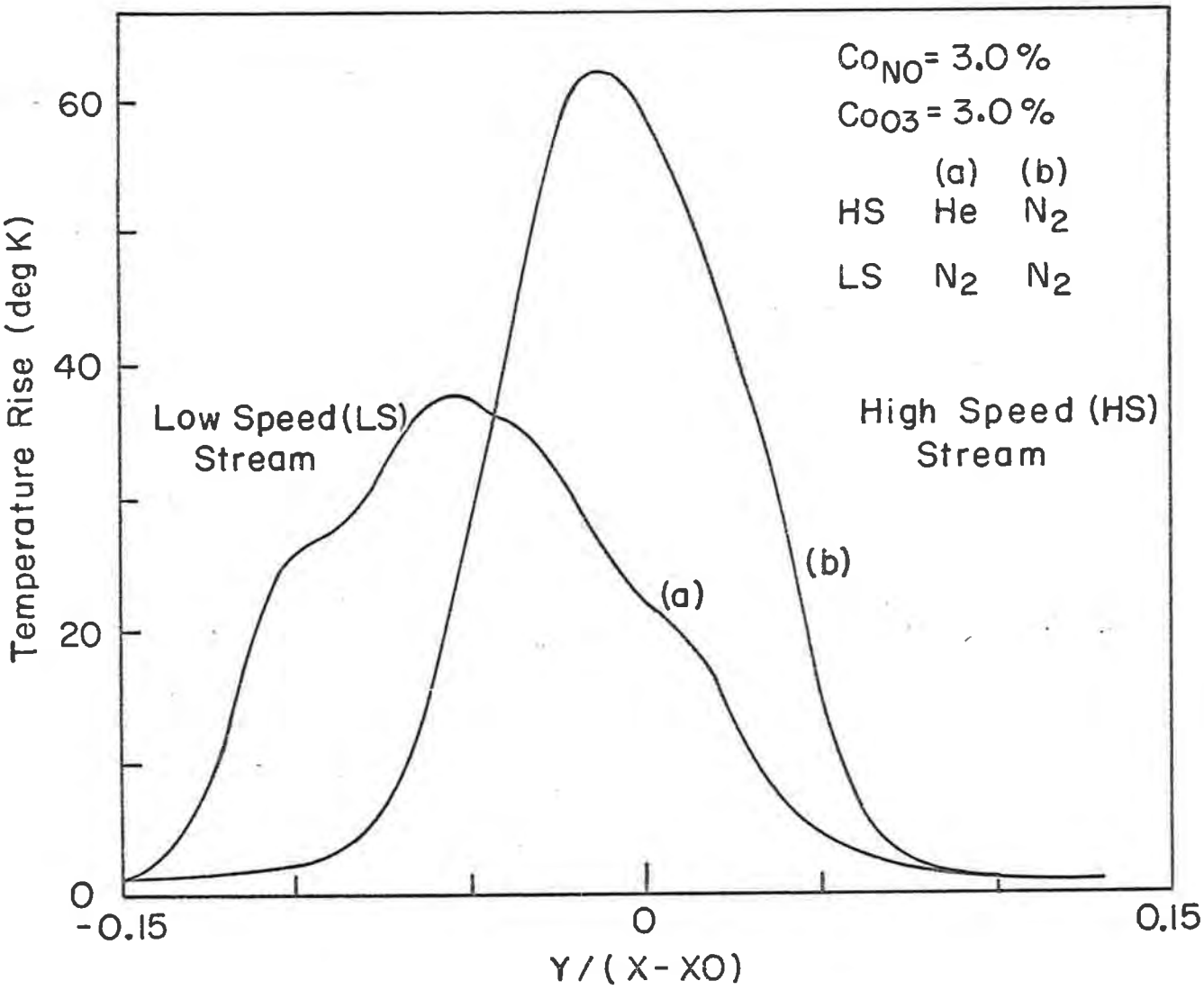

Fig. 3.24 Effect of Free Stream Density Difference on Temperature Profile.

strongly favours helium ($\bar{c}$ = 0.8, according to Figure 3, Konrad 1976) because of the increased entrainment of the lower density gas. The position of the mixture leading to the maximum temperature (about 1:1 since ξ is 1) is now moved strongly toward the nitrogen free stream, causing a shift to the left of the He/N_2 profile on Figure 3.24.

The result is in direct contrast to that which would be obtained in a laminar diffusion (or the analogous eddy diffusivity) model of the shear layer, which would predict a higher temperature in the He/N_2 case. The rigorous solution for the laminar diffusion model with unequal densities is discussed in Brown and Wallace (1981).

In Section 3.1.1 the significance of interacting density gradient and acceleration fields in causing a redistribution of the primary vorticity by baroclinic torque action was noted. A similar analysis of this non-uniform density layer provides an explanation for the asymmetric appearance and entrainment rate. The dotted line in Figure 3.25 represents an isopycnic surface between the helium and nitrogen free streams, which is normal to the density gradient, (Patnaik, Sherman and Corcos, 1976). The baroclinic torque term (refer to Section 3.1.1) on this line is seen to be strengthening the general vorticity in the region marked A and weakening it at B. The induced velocity (arrow C) in the helium free stream is consequently greater than that in the nitrogen, with the result that a larger volume

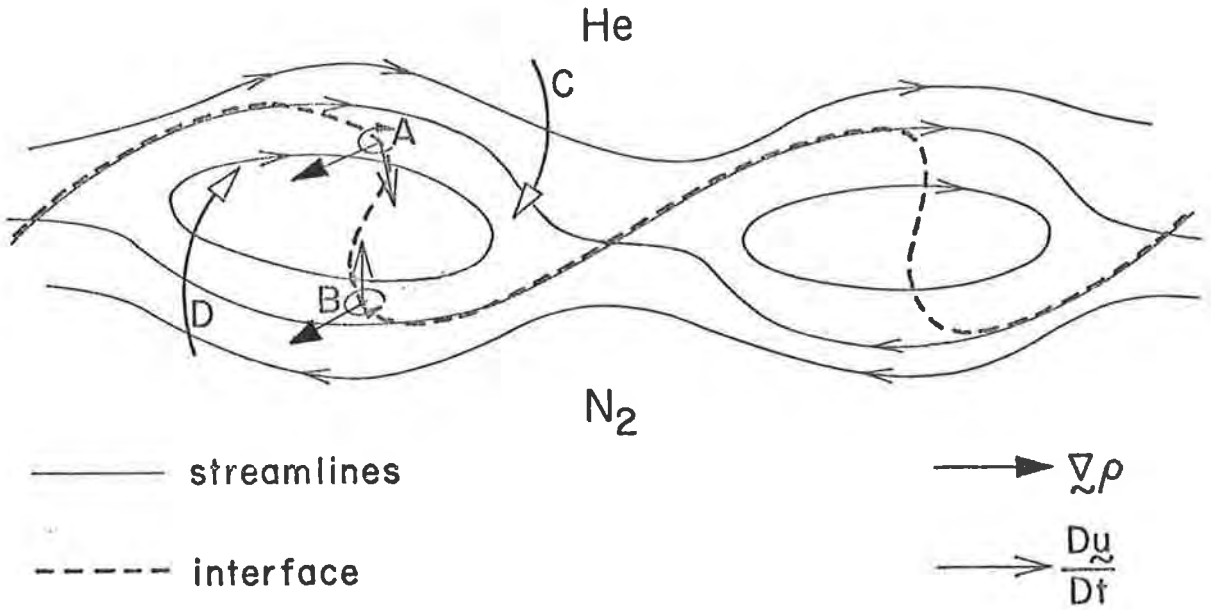

Fig. 3.25 Illustration of Baroclinic Torque Action in the Non-Uniform Density Shear Layer.

of helium enters the structure, thereby distorting it to the shape observed in Figure 3.2.

3.6. Mean Temperature Rise in Argon Shear Layers

Obviously, carrying the reactants in a gas with a lower specific heat should produce a higher temperature rise if all other flow parameters are the same. For this reason it was proposed to use argon instead of nitrogen as the carrier gas in order to achieve a higher temperature rise for a given reactant concentration, thereby enabling the heat release effect shown in Figure 3.23 to be checked to higher temperature. Upon doing the experiment, however, it was most surprising to find that this expected increase in temperature (an extra 40%) did not occur. Indeed, performing two consecutive, identical runs, except for merely swapping nitrogen for argon (a simple procedure on this facility), produced a slightly lower maximum mean temperature in the argon layer than in nitrogen! Numerous checks of the facility and probes were made, and a large number of runs taken. The results are shown in Figure 3.26, which is directly comparable with Figure 3.23. The velocities were 5 and 25 ms^{-1} and pressure 1 atm. $\overline{\theta}_{max}$ was measured at x = 100 mm.

At the time of writing, it is still unclear why the temperature rise in the argon shear layer falls so short of that predicted by the non-reacting PDFs of Konrad. The most likely explanation† appears to be one connected

† First suggested to me by Dr. Keith King, University of Adelaide.

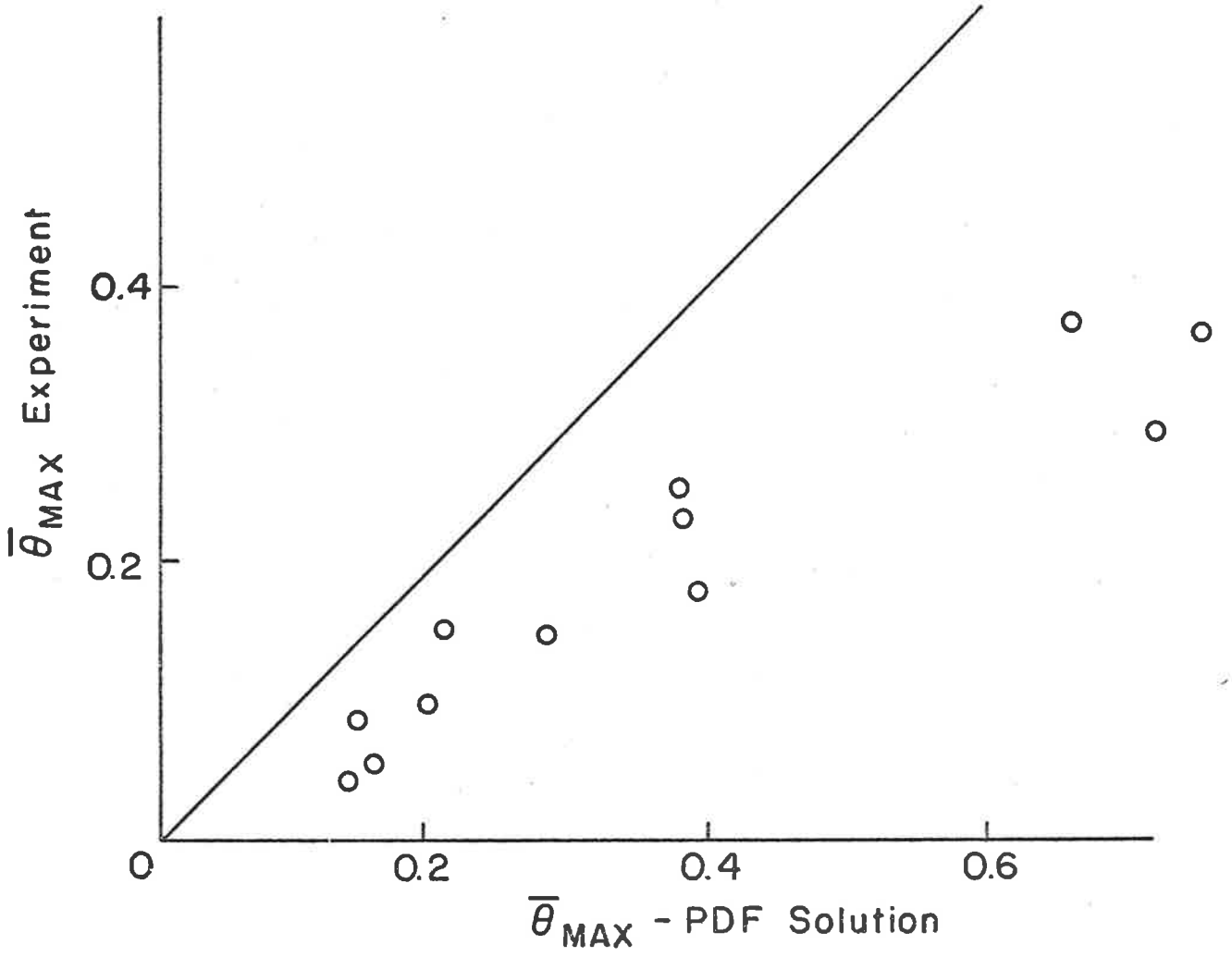

Fig. 3.26 Comparison of Measured $\overline{\theta}_{max}$ with $\overline{\theta}_{max}$ Inferred from Konrad's Non-reacting PDFs. (Argon Shear Layer)

with the chemical kinetics. It is reasonably well established that the ozone-nitric oxide reaction is basically a simple, one step, bimolecular reaction (Johnson & Crosby, 1954), but the appearance of the energy released (as a temperature) can be speed limited by the rate at which the activated NO_2^* transfers its energy to the carrier gas. i.e. the relevant reactions so far as temperature rise is concerned are

$$1.\quad NO + O_3 \rightarrow NO_2^* + O_2$$

$$2.\quad NO_2^* + M \rightarrow NO_2 + M + \text{heat.}$$

The reaction time quoted in calculating the Damkohler number (Appendix D) refers only to the first reaction, because it was determined by measuring the disappearance of ozone. The rate of reaction (2) has been assumed to be fast compared to reaction (1) making (1) the rate limiting step on the molecular scale. The rate of reaction (2) depends upon the collision kinetics of the molecules NO_2^* and M, and in particular on whether M is bimolecular (e.g. nitrogen) or atomic (e.g. argon), i.e. on the coupling efficiency. This coupling cannot be predicted by the cross sectional analysis model of molecular interaction. It is conceivable, (although no direct confirmation has been found in the literature to date) that the coupling of the vibrationally excited modes of NO_2^* to the molecule M will be more efficient if M is nitrogen than argon.

If this is the case, then the observed discrepancy is the result of a Damkohler number effect.

4. CONCLUDING REMARKS

The application of the unique flow facility described has begun to shed some light on the complex interaction between chemical heat release and turbulent mixing, perhaps the least well understood aspect of combustion at this point in time.

It has been demonstated that although the heat release has produced a volume expansion in the layer, the entrainment rate of free stream fluid has been reduced by about the same amount, causing the overall growth rate to remain substantially unchanged. Further understanding may determine if this is coincidental or has some mechanistic explanation. According to the pictures, the mixedness of the fluid in the layer is apparently reduced by the heat release as the small scales are progressively reduced. This is confirmed by mean temperature measurements which show that the relationship between mean temperature rise and reactant concentration (for a fixed reactant concentration ratio) is not linear beyond a temperature rise of $100^{o}K$. Experiments ranging to much higher temperature rises are needed to fully observe this trend and elucidate its implications on the shape of the mixture fraction PDFs.

APPENDIX A

Numerical Prediction of Temperature Rise Using Mixture Fraction PDFs

A1 Konrad's PDF Data

The extent of molecular scale mixing in the shear layer was measured with a Brown-Rebollo (1972) concentration probe having a spacial resolution of 200 μm and a frequency response to 45 kHz. Konrad obtained mixture fraction PDFs at seven positions across the layer for both the uniform and non-uniform density case. These are shown in Figures A1 and A2.

It is possible to use this data to predict the average and fluctuating species concentrations in the flow, and in particular find the product produced in a reacting flow. To do this we need to know, for a perfectly mixed particle, the resultant product concentration as a function of the mixture fraction and the two free stream reactant concentrations. This is derived in Section A2 below. The procedure to calculate the mean product concentration and temperature rise is given in A3.

Such a prediction involves the following assumptions:

(1) No effect of heat release on the fluid dynamics.

(2) An infinite Damkohler number, i.e., mixing limited reaction.

Assumption (1) is reasonably supported up to reactant

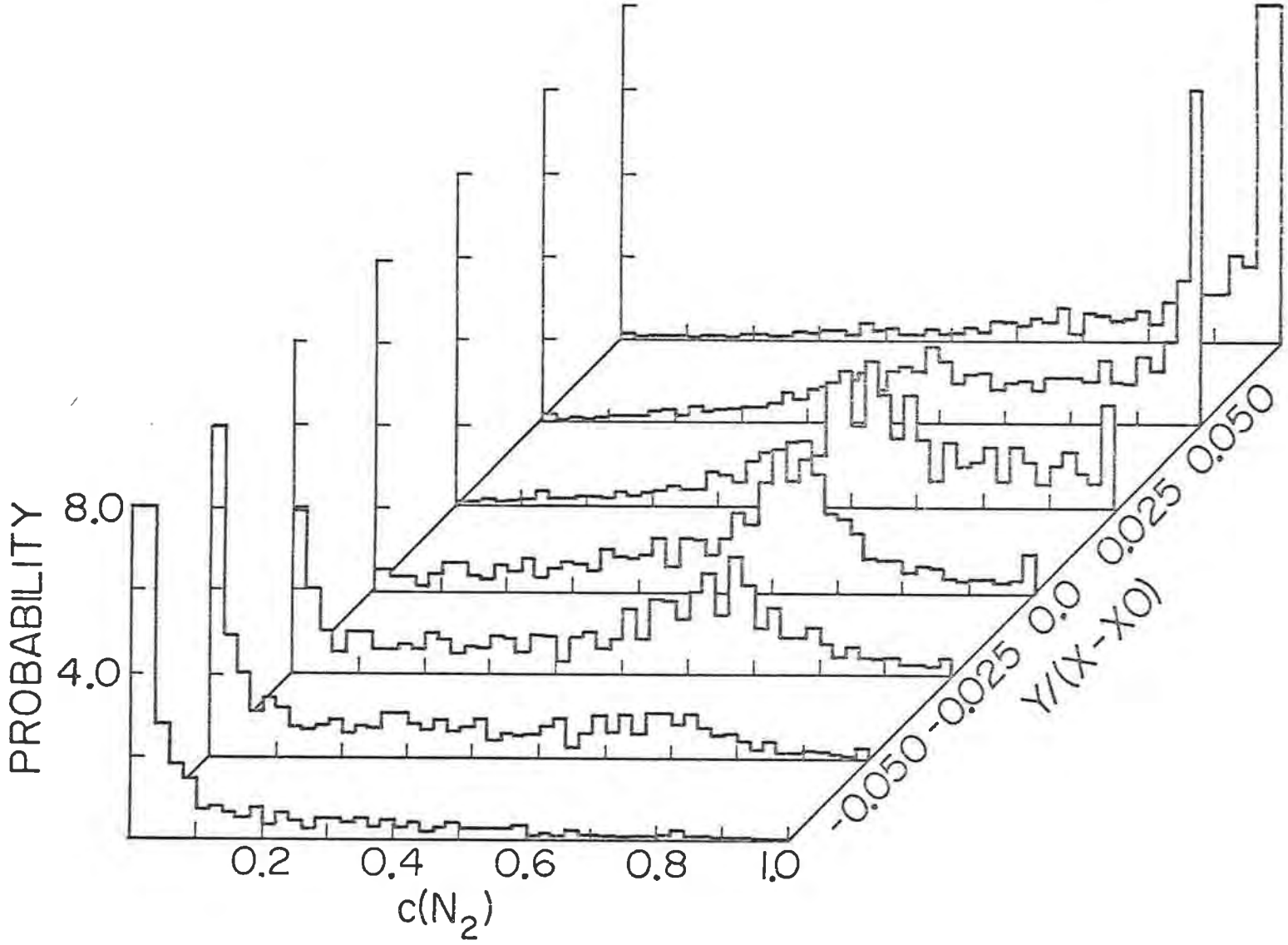

Fig. A1 Probability Density Function: r = 0.38, s = 1.0 (From Konrad).

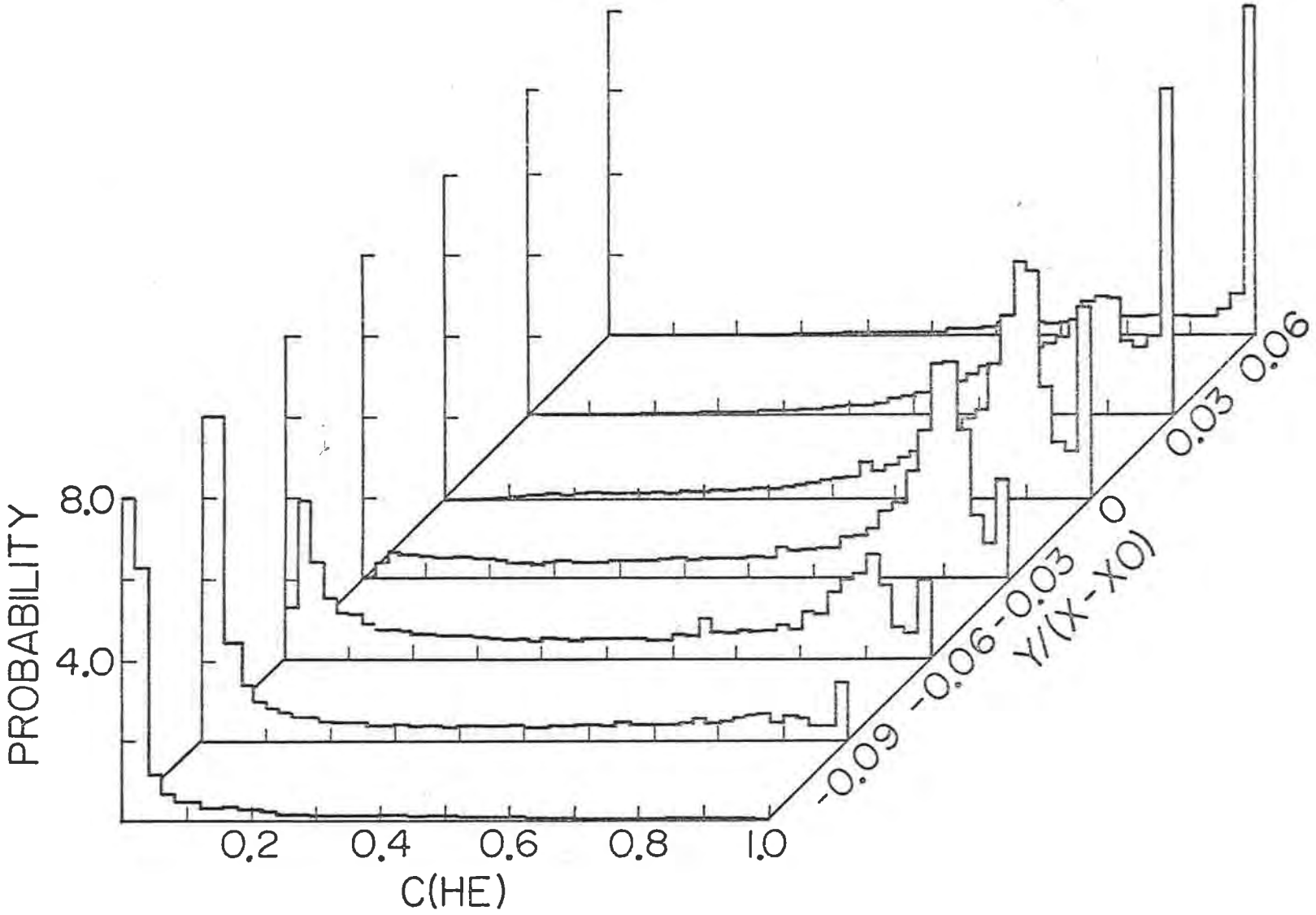

Fig. A2 Probability Density Function; r = 0.38, s = 7.0
(From Konrad).

concentrations of about 0.5% (only 5% change in density). Clearly this is not satisfied in the reacting flows but by comparing predictions based on this assumption with the actual results it is possible to determine the extent to which isothermal mixing is affected by the exothermic reaction. Refer Figure 3.23. The Damkohler number is estimated in Appendix D, where it is shown that the reaction rate is limited by the mixing process in this experiment except where the reactant concentrations are less than 1%. Most of the runs in this work were mixing limited.

A2 Perfect Mixing Analysis

The dominant reaction occuring in the flow is

$$O_3 + NO \rightarrow NO_2 + O_2$$

Consider two volumes of gas each with a total number of n_1 and n_2 molecules respectively. The n_1 molecules include n_{NO} molecules of NO in otherwise inert molecules, and likewise the n_2 molecules include N_{03} molecules of ozone. We define the free stream concentrations of NO and O_3 as

$$C_{0NO} = \frac{n_{NO}}{n_1} \tag{A1}$$

$$C_{003} = \frac{n_{03}}{n_2} \tag{A2}$$

and a mixture fraction

$$c = \frac{n_1}{n_1 + n_2} \tag{A3}$$

We also define the free stream reactant concentration ratio

$$\xi = \frac{C_{003}}{C_{0NO}} \tag{A4}$$

Now the two volumes of gas are mixed completely, i.e., the reaction proceeds until one of the reactants is completely exhausted. The concentration of the product NO is given by

$$C_{NO2} = \frac{n_{03}}{n_1 + n_2} \quad \text{if } n_{NO} > n_{03}$$

or

$$C_{NO2} = \frac{n_{NO}}{n_1 + n_2} \quad \text{if } n_{03} > n_{NO} \tag{A5}$$

which become

$$C_{NO2} = c\, C_{NO} \quad \text{if } n_{03} > n_{NO}$$

or

$$C_{NO2} = (1 - c)C_{03} \quad \text{if } n_{NO} > n_{03} \tag{A6}$$

At the point where $n_{03} = n_{NO}$, the reactants are present in their stoichiometric ratio, and the stoichiometric mixture fraction is given by

$$c_s C_{NO} = (1 - c_s)C_{03}$$

i.e.

$$c_s = \frac{C_{03}}{C_{03} + C_{NO}} \tag{A7}$$

and

$$c_s = \frac{\xi}{\xi + 1} \tag{A8}$$

This mixture fraction leads to the maximum achievable product concentration

$$C_{NO2}{}^{max} = c_s C_{NO} \tag{A9}$$

C_{NO2} as a function of c is plotted in Figure A3. In

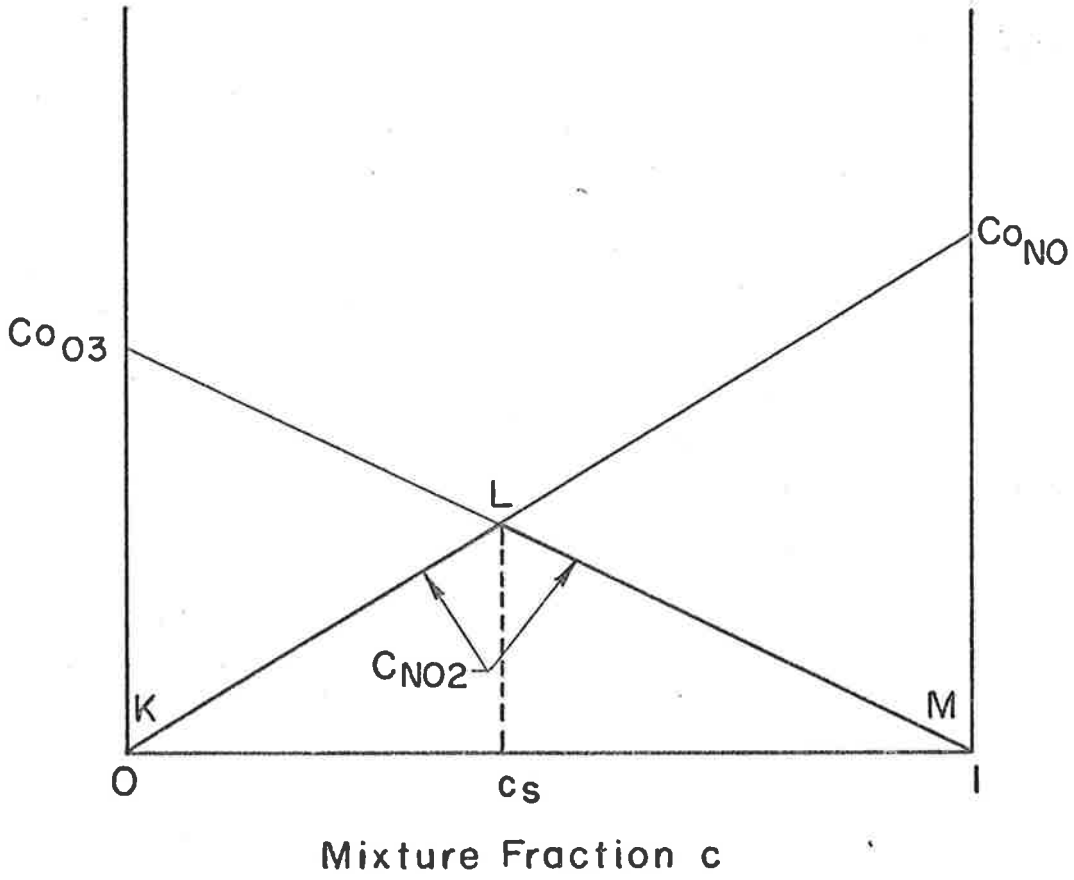

Fig. A3 The Function $C_{NO2}(c)$.

perfect mixing then, the operating point moves along the path KLM, achieving a maximum C_{NO2} at a mixture ratio c_s defined by equation A8.

Hence

$$C_{NO2}(c) = C_{NO}(c\,H(c_s - c) + \xi(1 - c)H(c - c_s)) \qquad (A10)$$

where H(x) is the Heaviside step function.

In the case where both free streams have the same specific heat, temperature rise becomes the direct analogue of product concentration since

$$T(c) = \frac{n_{NO2}\Delta H_f}{(n_1 + n_2)C_p} = C_{NO2}\frac{\Delta H_f}{C_p} = \text{const. } C_{NO2}(c) \qquad (A11)$$

where ΔH_f is the heat release per mole of reaction and C_p is the average specific heat per mole of the mixture at constant pressure. The abscissa of Figure A3 could equally well be temperature rise.

In the case where the two incident streams have different specific heats, the specific heat of the mixture is a function of mixture ratio. Hence

$$T(c) = \frac{\Delta H_f C_{NO2}(c)}{C_p(c)} \qquad (A12)$$

where

$$C_p(c) = C_{p2} + c(C_{p1} - C_{p2}) \qquad (A13)$$

A3 Calculation of Product Concentrations and Temperature Rise Profiles

The mean product concentration is calculated from its own PDF using the identity

$$\overline{C_{NO2}} \equiv \int_{C_{NO2}} C_{NO2}\, p_{NO2}(C_{NO2})\, dC_{NO2} \qquad (A14)$$

C_{NO2} is a function of c (equation (A10) which is now made the variable of integration

$$\overline{C_{NO2}} = \int_{c} C_{NO2}(c) \left[p_{NO2}(C_{NO2}) \frac{dC_{NO2}}{dc} \right] dc \qquad (A15)$$

The quantity in square brackets is the mixture fraction PDF $p_c(c)$, by identity (e.g. Fry 1965).

Hence

$$\overline{C_{NO2}} = \int_0^1 C_{NO2}(c)\, p_c(c)\, dc \qquad (A16)$$

Similarly,

$$\overline{\Delta T} = \int_0^1 T(c)\, p_c(c)\, dc \qquad (A17)$$

where T(c) is defined in equations A11 and A12. To construct a temperature profile, equation A17 was solved with each of the seven PDFs $p_c(c)$ measured by Konrad. This was done numerically with a simple FORTRAN program.

APPENDIX B

B1 Calculation of the Dividing Streamline

The position of the dividing streamline was found from the mean temperature and velocity profiles using the following expression

$$\int_{y^*}^{\infty} (\overline{\rho}\ \overline{u}\ U_1 - \overline{\rho}\ \overline{u^2})dy = \int_{-\infty}^{y^*} (\overline{\rho}\ \overline{u^2} - \overline{\rho}\ \overline{u}\ U_2)dy$$

This estimation is necessarily an approximation since a number of higher order terms, as well as correlations, have been omitted. The expression is simply obtained from the conservation of continuity and momentum in a strip extending to infinity each side of the dividing streamline.

APPENDIX C

Digital Filter Characteristics

The digital filter was used to smooth both the temperature and velocity signal and is identical to that used by Thomas (1977) previously of this department, who provided much of the information appearing in this section. It was described by Linn (1977).

Physically, the filter steps through the data record, averaging a fixed span of samples and placing the result at the span centre. Z plane analysis is used to obtain the frequency response and phase shift characteristic. The Z transform in this case is

$$Y(z)/X(z) = \left(\frac{1 - z^{k}}{1 - z}\right)^{n} \qquad (C1)$$

where

k = order of the filter

n = number of applications

Y,X = output and input respectively

$Z = e^{j\omega P}$

P = sample period

ω = circular frequency

which represents k zeroes equispaced around the unit circle, with one (at ω = 0) being cancelled by a coincident pole. The time domain operation, obtained by inspection from equation C1 is for r = 1.

$$Y_n - Y_{n+1} = X_n - X_{n+k}$$

i.e.

$$Y_{n+1} = Y_n - X_n + X_{n+k} \qquad (C2)$$

The record has experienced a shift of $(k - 1)/2$ sample periods by this process, or after n applications of the filter, a total shift of $n(k - 1)/2$ sample periods. By choosing an even number for n, a shift of an integral number of sample periods is assured. The shift is obviously independent of frequency, and is readily nulled by an equal shift of opposite sign after the filtering process. Choosing a higher value of n also has the advantage of giving the filter a shorter cutoff. The filter is recursive because it is using a previous output (Y_n) to derive the new output ($Y_n + 1$). This feature causes the RH side of equation C2 to have only 3 terms and permits rapid computation.

Although the actual filter cutoff is only of secondary consideration for present purposes, a typical frequency response is plotted in Figure C1. The computations of the curve was extended to a frequency of 5/2P to graphically show the Nyquist folding phenomenon within the filter at 1/P, 2/P.† Such folding is a danger since it causes high frequency energy to appear as low frequency energy after the digital processing. The only way of avoiding it is to ensure (by using analogue filters

---

† A good discussion of this phenomenon is to be found in Bendat & Piersol (1971).

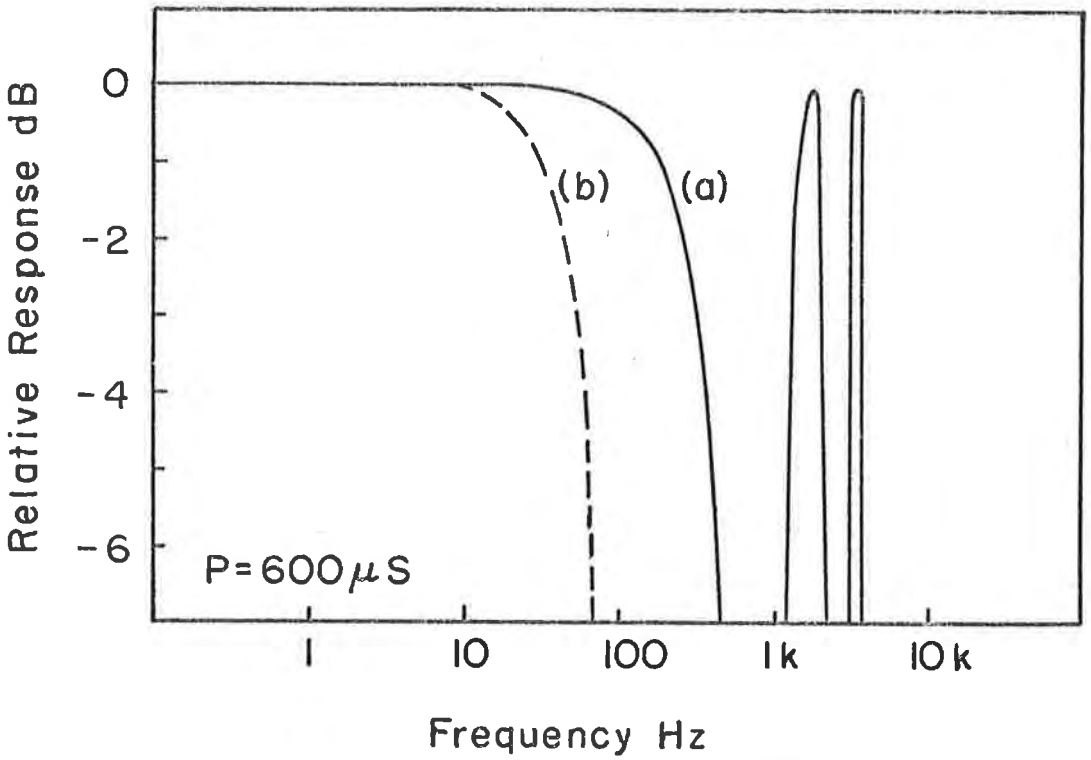

Fig. C1 Relative Frequency Response of Low Pass Filters
(a) n = 2, k = 2
(b) n = 2, k = 10

if necessary) that the analogue signal contains, neglible energy content above frequency of 1/2P. The sampling periods used were selected on this basis and checked by inspection of an expanded plat of the digital-to-analogue converted signal to ensure that an acceptably "clean" analogue signal could be obtained by connecting all the plotted points with a straight line.

APPENDIX D

Calculation of the Damkohler Number

The purpose of this section is to calculate a relative time scale for the chemical reaction and compare it to the range of mixing time scales in the flow. Mixing in the shear layer occurs over a wide range of length and time scales, the largest being the scale of the width of the shear layer (because no larger structure could possibly be incorporated) and the smallest being the scale at which molecular diffusivity becomes dominant enough to smear the inhomogenities into molecular homogeniety.

D1 Mixing Time Scales

The largest time scale, called the convection time scale τ_c is derived from the mean velocity $(U_1 + U_2)/2$ and the layer width at the cross section of interest.

$$\tau_c = \frac{2\delta_\omega}{U_1 + U_2}$$

In this experiment, at x = 100 mm,

$$\delta_\omega \doteq 20 \text{ mm}$$

$$U_1 = 25 \text{ m/s}$$

$$U_2 = 5 \text{ m/s}$$

hence the typical convection time is

$$\tau_c = \frac{2 \times .02}{25 + 5} = 660 \times 10^{-6} \text{ sec}$$

The smallest turbulent length scale is the Kolmogorov microscale

$$\lambda = (\nu^2/\varepsilon)^{1/4}$$

ν = kinetic viscosity

ε = K.E. dissipation rate per unit mass.

The dissipation rate can be taken as

$$\varepsilon = (U_1 - U_2)^3/\delta_\omega$$

If the molecular diffusivity is D, then the time scale appropriate to the smearing of these smallest eddies is

$$\tau_D = \frac{\lambda^2}{D}$$

which becomes

$$\tau_D = Re^{-1/2} \frac{\nu}{D} \frac{\delta_\omega}{\Delta U}$$

The Schmidt no. $\frac{\nu}{D}$ for the species in this flow is about unity. Hence

$$\tau_D = \frac{\delta_\omega}{\Delta U} Re^{-1/2}$$

For most of the flow in this case

$$Re = \frac{\Delta U \, \delta_\omega}{\nu} = \frac{20 \times .02}{1.6 \times 10^{-5}} = 2.5 \times 10^4$$

$$\tau_D = \sim 6.3 \times 10^{-6} \text{ secs.}$$

D2 Reaction Speed Time Scale

The reaction rate of the second order reaction is

$$\frac{d\,C_{03}}{dt} = k\, C_{NO}\, C_{03}$$

and

$$k = 0.8 \times 10^{12} e^{\frac{-2.5}{Rt}} \text{ cc mole}^{-1}\text{sec}^{-1}$$

The chemical time scale is obtained from

$$\frac{d(C_{03}/C_{03\,0})}{dt} = k C_{NO} \quad \text{i.e. } \tau_{chem} = \frac{1}{k C_{NO}}$$

which is at 5% concentration

$$\tau_{chem} = 40 \times 10^{-6} \text{ sec.}$$

The concentration at which $\tau_{chem} \doteq \tau_c$ is 0.3%.

D3 Summary

$$\tau_c \sim 660 \text{ μs}$$

$$\tau_D \sim 6 \text{ μs}$$

$$\tau_{chem} \sim 40 \text{ μs}$$

The ratio of mixing time to chemical reaction time is known as the Damkohler number, $\alpha = \frac{\tau_{mix}}{\tau_{chem}}$. The mixing rate is limited by the slowest of the steps, i.e. τ_c. The value of α is therefore about 16 at 5% reactant concentration, falling to 1 at 0.3% reactant concentration. Thus the rate of product formation is controlled by the mixing process (the large scale time) unless the reactant concentrations are somewhat less than 1%.

D4 Ozone-Nitric Oxide Chemistry

The following ractions are known to occur in the range 300 to 1000 K. Reaction 1 is dominant between 300 and 500°K.

Reaction rate $k_f = AT^{-N} \exp(E_a/RT)$

No.	Reaction	A cm^3 $molecule^{-1}$ sec^{-1}	E_a	N
1	$NO + O_3 \rightarrow NO_2 + O_2$	9.0×10^{-13}	- 2500	0
2	$NO_2 + NO_2 + O_2 \rightleftarrows NO + NO$	1.0×10^{-12}	- 26800	0
3	$O_3 + M \rightleftarrows O_2 + O + M$	6.4×10^{-10}	- 22800	0
4	$O + NO_2 \rightarrow NO + O_2$	9.1×10^{-12}	0	0
5	$O_3 + NO_2 \rightarrow NO + O_2 + O_2$	9.8×10^{-12}	- 7000	0
6	$O + O_3 \rightarrow O_2 + O_2$	1.5×10^{-11}	- 4480	0
7	$NO + O + M \rightleftarrows NO_2 + M$	1.0×10^{-31}	0	2.5

Note also for reaction 1 $\Delta H_f = -47.5$ kcal $mole^{-1}$

$$\kappa = [NO_2][O_2]/[NO][O_3] \sim 5 \times 10^{34}$$

5. REFERENCES

BATCHELOR, G.K., 1952, "Stretching of Fluid Lines and Surfaces in Homogeneous Turbulence" Proc. Roy. Soc. (London) A213, p. 349.

BATT, R.G.., 1977, "Turbulent Mixing of Passive and Chemically Reacting Species in a Low Speed Shear Layer" JFM 82 1, p. 53.

BENDAT, J.S. and PEIRSOL, A.C., 1971. "Random Data Analysis and Measurement Procedures" Wiley Press.

BILGER, R.W., 1976, "Turbulent Jet Diffusion Flames" Prog. E. Comb. Sci., 1, p. 87.

BROWN G.L. and REBOLLO, M., 1972, "A Small but Fast Response Probe to Measure Composition of a Binary Gas Mixture" AIAA 10, p. 649.

BROWN, G.L. and ROSHKO, A., 1974, "On Density Effects and Large Structure in Turbulent Mixing Layers" JFM 64 p. 775.

BROWN, G.L., 1974 "The Entrainment and Large Structure in Turbulent Mixing Layers", 5th Aust. Conf. on Hydraulics and Fluid Mech., Christchurch, New Zealand.

CHANDRASUDA, C., et al. 1978, JFM 4, p. 693.

COOK., et al. 1966 "Separation of Ozone from Oxygen by a Sorption Process", Ozone Chemistry and Technology, Advances in Chemistry Series, Int. Ozone Conf., p. 13.

CORRSIN, S., 1958, "Statistical Behaviour of a Reacting Mixture in Isotropic Turbulence" Phys. of Fluids, 1, p. 42.

DIMOTAKIS, P.E. and BROWN, G.L., 1975 "Large Structure Dynamics and Entrainment in the Mixing Layer at High Reynolds Number." Tech. Rep. CIT-7-PU, Project SQUID.

FRY, T.C., 1965, "Probability and its Engineering Uses", Van Nostrand.

GREEN, A.E.S., 1966 "The Middle Ultraviolet" Wiley Pres, P. 304.

GRIGGS, M., 1968, "Absorption Coefficients in Ozone in the Ultraviolet and Visible Regions" J. Chem Phy. 49, part 2, p. 857.

HALL, T. and BLACET F., 1952, "Separation of the Absorption Spectra of NO_2 and N_2O_4 in the Range 2400-5000 Å", J. Chem. Phy. 20, p. 1745.

HARPER, S.A. and GORDON, W.E., 1966,"Detonation Properties of Ozone", Ozone Chemistry and Technology, Advances in Chemistry Series, Int. Ozone Conf. p. 28.

HERRON, J.T. and HINE, R.E., 1973, J. Chem. Phys. Ref. Data 2, p. 299.

JENKINS, A.C., 1966, Ozone Chemistry and Technology, Advances in Chemistry Series, Int. Ozone Conf., p. 13.

JOHNSON, H.S. and CROSBY, H.J., 1954, "Kinetics of the Fast Gas Phase Reaction between Ozone and Nitric Oxide" J. Chem. Phys. 22, p. 689.

KENT, and BILGER, R., 1973, "Turbulent Diffusion Flames" Proc. 45h Int. Symp. on Combustion, p. 615.

KOLMOGOROV, A.N., 1940, C.R. Academy of Sciences, USSR 30, p. 301.

KONRAD, J.H., 1977, "An Experimental Investigation of Mixing in Two-Dimensional Turbulent Shear Flows with Applications to Diffusion Limited Chemical Reactions" Tech. Rep. CIT-8-PU Project SQUID.

LIEPMANN, H.W. and LAUFER, J., 1949, "Investigations of Free Turbulent Mixing", NACA TN 1257.

LIN, C.H. and O'BRIEN, E.E., 1974, "Turbulent Shear Flow Mixing and Rapid Chemical Reactions: an Analogy", JFM 64, p. 195.

LYNN, P.A., 1972, "Recursive Digital Filters with Linear Phase Characteristics", Computer Jnl. 15, p. 337.

O'BRIEN, E.E., 1971, "Turbulent Mixing of Two Rapidly Reacting Chemical Species", Phys. of Fluids 14, p. 1326.

PARIS, J.P., 1966, "Chemiluminescence", Enc. of Chem. G.L. Clark (ed.) Rheinhold, New York.

PATNAIK, P.C., SHERMAN, F.S. and CORCOS, G.M. 1976, "A Numerical Simulation of Kelvin-Helmholtz Waves of Finite Amplitude" JFM 73, part 2, p. 215.

SABERSKY, R.H., SIMERA, D.A. and SHAIR, F.H., 1973, Env. Sci. and Tech. 7, p. 347.

SHEA, J.R., 1976, "A Chemical Reaction in a Turbulent Jet", Ph.D. Thesis, CALTECH.

SPALDING, D.B., 1974, Project SQUID Workshop on Turbulent Mixing in Reacting and Non-Reacting Flows.

SPENCER and JONES, 1971, AIAA Preprint of paper 71-613.

TOOR, H.L., 1962, "Mass Transfer in Dilute Turbulent and Non-Turbulent Systems with Rapid Irreversible Reactions and Equal Diffusivities", A.I.Ch.E.J. 8, p. 70.

TUTU, N.K. and CHEVRAY, R., 1973, Bulletin Am. Phys. Soc. II 18, p. 11.

VERHOEK, F.H. and DANIELS, F., 1931, J. Am. Chem. Soc. 53, p. 1250.

WAHL, K., GAZELY, C., and KAPP, N., 1949, 3rd Int. Symp. on Combustion.

WYGNANSKI, I. and FIEDLER, H.E., 1970, JFM 41, part 2, p. 327.